UNIVERSITY OF CALIFORNIA SAN DIEGO

Wind, wave, and current interactions

A dissertation submitted in partial satisfaction of the

requirements for the degree

Doctor of Philosophy

in

Oceanography

by

Ana Beatriz de Figueiredo Melo Villas Bôas

Committee in charge:

Bruce D. Cornuelle, Co-Chair

Sarah T. Gille, Co-Chair

Matthew R. Mazloff, Co-Chair

Myrl C. Hendershott

Jan P. Kleissl

William R. Young

2020

The dissertation of Ana Beatriz de Figueiredo Melo Villas Bôas is approved, and it is acceptable in quality and form for publication on microfilm and electronically:

_____

_____

_____

_____

Co-Chair

_____

Co-Chair

_____

Co-Chair

University of California San Diego

2020

DEDICATION

The missing piece meets the Big O.

To Guilherme.

EPIGRAPH

You'll go backwards, but then

You'll go forwards, again

You'll go backwards, but then

You'll go.

—C. Martin, J. Buckland, G. Berryman, and W. Champion

TABLE OF CONTENTS

LIST OF FIGURES

LIST OF TABLES

ACKNOWLEDGEMENTS

First, I would like to thank all members of my committee for their advice and contributions.

One of the things that made me choose Scripps for my Ph.D. was the fact that we didn't have to pick an advisor in advance. While this was a source of stress for many of my peers, I was pretty confident that it wasn't going to be too hard to find a good match. It was Scripps, after all. How hard could it be? What I did not expect was to win the lottery three times. I don't usually brag about things, but let me tell you: I've had the best advisors any student could possibly wish for. Sarah, Bruce, and Matt, you have shaped me into the scientist that I am today. You have encouraged and supported me in all paths that I wanted to follow. You respected my limits. You listened. You let me wonder. Together, we learned how to say "yes, and". We worked hard, and we laughed a lot. I look up to the three of you, and I hope that one day I can be to someone the mentor that you were to me.

Bill, thanks for teaching to pay attention. Thanks for teaching me that right is good, but beautiful is better. I look forward to more blackboard adventures with you.

Myrl, I don't even know how to begin. Perhaps I should just say that being around you is a constant reminder that as a little 8-year-old, I wanted to do science just to know. Thanks for keeping me curious.

In the early years of my Ph.D., I was lucky enough to have Ken Melville in my committee. Ken was kind, patient, and a wonderful teacher. He always had very thoughtful advice, and we had plans to work together after I graduated. Ken is the most complete scientist that I have ever met, and I hope my work can contribute to his legacy.

From the moment I decided I wanted to work with wave modeling, I knew that I had to find a way to get to Fabrice Ardhuin. Since the very beginning of my Ph.D., Fabrice has been an incredible mentor and collaborator. He has opened many doors for me in the surface waves community (including the door of his office at IFREMER). While juggling between multiple projects and being a PI for a satellite, Fabrice has always found time to give me

advice and point me in the right direction. I am very grateful for having had the opportunity to collaborate with him.

Besides my advisors and collaborators, I had truly amazing teachers and mentors at Scripps. A special thanks to Walter Munk, Falk Feddersen, Ian Eisenman, Art Miller, and Rob Pinkel. They have done everything that they could to make sure I would succeed.

Navigating grad school was pretty overwhelming at times. I can't thank the SIO staff enough for making my life a lot easier. In particular, I would like to thank Gilbert Betrado, Tomomi Ushii, and Will Riveira. You are outstanding. I'm sure that caring for us, students, as much as you do, was not in your job description.

At Scripps, I have also found two incredible peer mentors who I can now call friends. Ruth and Nick, as a scarred and often lost grad student, it made a whole lot of difference to count on you. Thank you for listening and for being there for me.

I also had the privilege to work with two outstanding undergraduates. Luke and Roger, it was incredible to watch you grow, and I'm really proud of the two of you.

Perhaps I shouldn't have said that I don't brag about things, because I also had the best cohort of all time. Thanks to Paul, the champion; Derek, the delusional; Olavo, the out-there; Effie, the esteemed; Alan, the adored; Isa, the influential; Stephen, the superb; Reuben, the remarkable; and Dillon... the dingleberry, I'm kidding. Dillon, the dreamer. You guys have made this journey a wonderful adventure. It always surprises me how many incredible things have happened in my life by pure chance. Mika, thanks for being such a good friend. I hope our future adventures never involve crashing tens of thousands of dollars into a seamount ever again.

People often ask me if I miss Brazil. I don't. But no one can even imagine how much I miss people. This feeling is something so culturally important that we have a word for it in Portuguese: "saudade". The hardest thing since I left my hometown many years ago is not being there for the ones I love when they need me the most. I grew up surrounded by love, trust, freedom, and ocean. I deeply thank my parents and grandparents for raising me as a

curious and fearless child and for their unconditional support. My parents also gave me the most precious gift that I've ever received, my sisters. I don't know what I would do without you in my life. Gaby and Bianca, thanks for making my heart bigger, so it could hold the love that I have for you. Thanks to my favorite scientist, sensei, therapist, and uncle, Dr. Claudio Melo, and to my aunt Lucivanda. Thanks to my best friends, Hanoch, Alan, Barbara, and Zé, for being by my side since I can remember. Thanks to all my family and friends for not letting the distance make us grow apart.

Finally, there is only one person who has seen it all. Who was right there in my rains and shadows. Gui, we've come a long way. Everything you gave and nothing you would take. None of this would have been possible without you. I Love you to Arrakis and back. Good things are coming our way.

Chapter 2, in full, reprints material as it appears in Journal of Geophysical Research: Oceans, 2017, DOI:10.1002/2017jc013280. Ana B. Villas Bôas, Sarah T. Gille, Matthew R. Mazloff, Bruce d. Cornuelle. The dissertation author was the primary investigator and author of this paper.

Chapter 3, in full, reprints material as it appears in Journal of Fluid Mechanics, 2020, DOI:10.1017/jfm. Ana B. Villas Bôas and William R. Young. The dissertation author was the primary investigator and author of this paper.

Chapter 4, in full, reprints material as it appears in Journal Physical Oceanography, 2020, DOI:10.1175/JPO-D-20-0151.1. Ana B. Villas Bôas, Bruce D. Cornuelle, Matthew R. Mazloff, Sarah T. Gille, and Fabrice Ardhuin. The dissertation author was the primary investigator and author of this paper.

VITA

2012	B. S. in physics, Federal University of Rio Grande do Norte, Brazil
2014	M. S. in physical oceanography, University of São Paulo, Brazil
2020	Ph. D. in physical oceanography, University of California San Diego

PUBLICATIONS

Ana B. Villas Bôas, Sarah T. Gille, Matthew R. Mazloff, Bruce D. Cornuelle, and Fabrice Ardhuin. Wave-current interactions at meso and submesoscales: insights from idealized numerical simulations. Journal of Physical Oceanography, DOI:10.1175/JPO-D-20-0151.1.

Ana B. Villas Bôas and W. R. Young. Directional diffusion of surface gravity wave action by ocean macroturbulence. Journal of Fluid Mechanics, 890:r3, 2020. DOI: 10.1017/jfm.2020.116

SophiaMerrifield, Eric Terrill, Travis Schramek, Sean Celona, **Ana B. Villas Bôas**, and Patrick Colin. Typhoon-forced waves around a western Pacific island nation. Oceanography, 33, 2019. DOI: 10.5670/oceanog.2019.411

Ana B. Villas Bôas, Fabrice Ardhuin, Ernesto Rodriguez, Christine Gommenginger, et al. Integrated observations of global surface winds, currents, and waves: requirements and challenges for the next decade. Frontiers in Marine Science, 2019. DOI: 10.3389/fmars.2019.00425

Ana B. Villas Bôas, Sarah T. Gille, Matthew R. Mazloff, and Bruce D. Cornuelle. Characterization of the deep water surface wave variability in the California Current region. Journal of Geophysical Research: oceans, 122(11):8753–8769, 2017. issn 2169-9291. DOI: 10.1002/2017jc013280

Ana B. Villas Bôas, Olga T. Sato, Alexis Chaigneau, and Guilherme P. Castelão. The signature of mesoscale eddies on the air-sea turbulent heat fluxes in the South Atlantic ocean. Geophysical Research Letters, 42(6):1856–1862, 2015. DOI: 10.1002/2015gl063105

Guilherme P. Castelão, Luiz C. Irber, and **Ana B. Villas Bôas**. An objective reference system for studying rings in the ocean. Computers & Geosciences, 61:43–49, 2013. DOI:10.1016/j.cageo. 2013.07.004

ABSTRACT OF THE DISSERTATION

Wind, wave, and current interactions

by

Ana Beatriz de Figueiredo Melo Villas Bôas

Doctor of Philosophy in Oceanography

University of California San Diego, 2020

Bruce D. Cornuelle, Co-Chair

Sarah T. Gille, Co-Chair

Matthew R. Mazloff, Co-Chair

Surface gravity waves play a major role in the exchange of momentum, heat, energy, and gases between the ocean and the atmosphere. Strong winds blowing over long fetches give rise to long-period waves, known as swell, that can propagate great distances from their source; hence, the surface wave field in a given region results from the combined response to both local and remote wind forcing. Surface winds off the California coast are marked by

strong seasonality and regional scale variability associated with the coastal orography. As a consequence, a particular aspect of the surface wave variability in this region is the influence of these regional-scale high wind events that occur during spring and summer. These alongshore "expansion fan" winds have average speeds of $\sim$10 m/s and are the dominant forcing for waves off central/northern California, leading to relatively short period waves (8-10 s) that come predominantly from the north–northwest.

Waves are also modulated by ocean currents via wave–current interactions, which lead to variations in their direction, frequency, and amplitude. The surface current field in the California Current system (CCS) region is mostly dominated by balanced (rotational) motions in late winter/spring, while divergence is stronger in late summer/fall. Here, we propose a theoretical framework based on ray theory to assess the effects of current divergence and vorticity in the diffusion of wave action density. We show that the potential (divergent) component of the flow has no contribution to the diffusion of wave action.

In a separate study, we analyze a large ensemble of numerical experiments using the wave model WAVEWATCH III forced with idealized currents to investigate the role of divergent and rotational flows in modifying wave properties, including direction, period, directional spreading, and significant wave height (H_s). Finally, the results obtained using idealized currents are used to interpret the response of surface waves to realistic currents by running an additional set of simulations using the llc4320 MITgcm output in the CCS region.

Chapter 1

Introduction

The energetic balance between ocean, atmosphere, ice, and land regulates the Earth's climate. This balance is governed by processes that couple different components of the system in a number of complex interactions that happen at the boundaries. In particular, the marine atmospheric boundary layer provides a medium for the atmosphere and the ocean to constantly exchange energy, momentum, heat, freshwater, gases, and other tracers, as illustrated in the schematic in Figure 1.1. These fluxes are largely modulated by interactions between surface winds, waves, and currents. Despite wave motions being strongly coupled to the upper-ocean circulation and the overlying atmosphere, efforts to improve climate and wave models have evolved somewhat independently; however, surface wave physics may be key to improving climate models and better representing the coupling between the ocean and the atmosphere (Cavaleri et al., 2012; Villas Bôas et al., 2019). In this context, the questions that I address in this dissertation are aimed at bridging the gap between ocean and wave models and in advancing our understanding of how winds and currents affect the wave field.

While waves propagating over a uniform current are simply subject to a Doppler shift of their frequency, current gradients can modify the wavenumber, direction, and amplitude of the waves, having the potential to largely modulate the surface wave field. Even though the theoretical basis for such interactions is well established (Longuet-Higgins and Stewart, 1961),

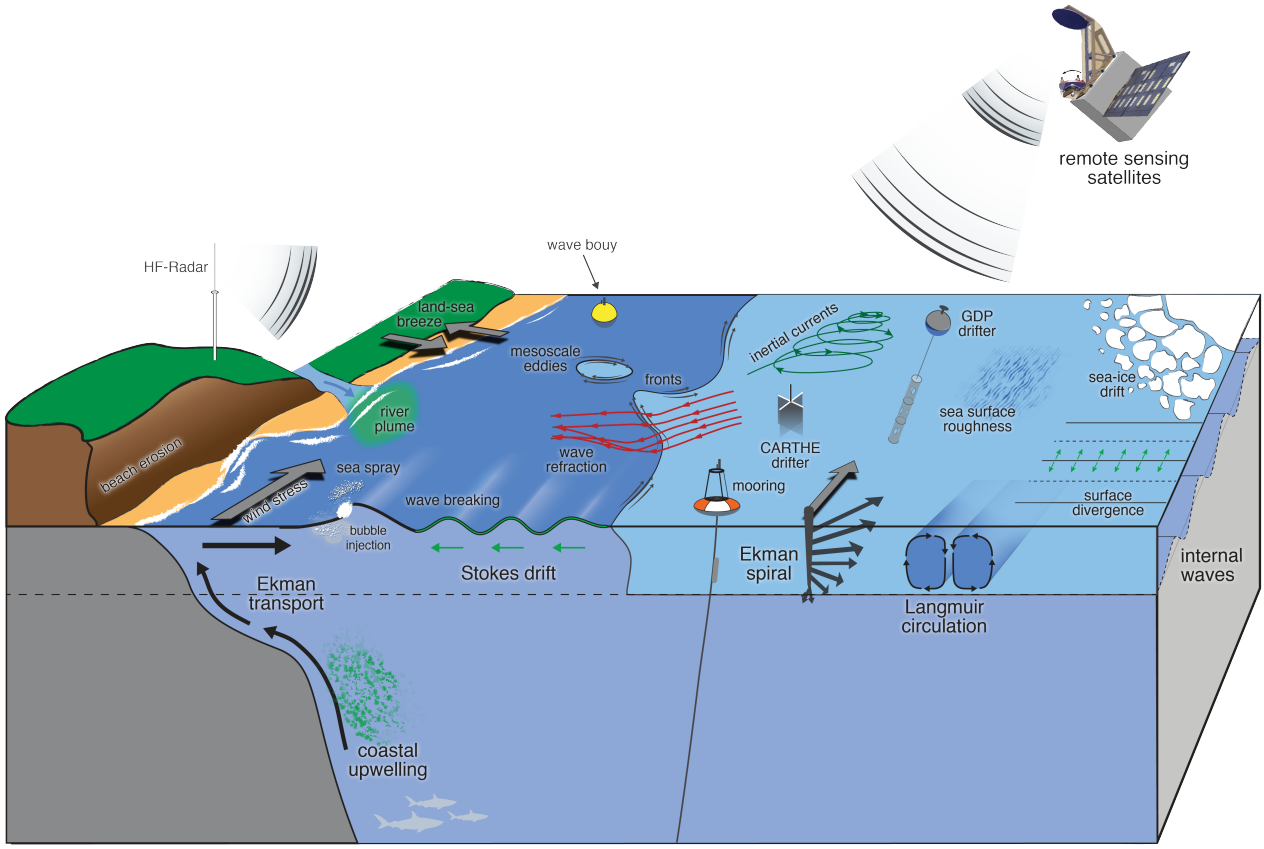

Figure 1.1: Schematic representation of upper-ocean processes that are coupled through the interaction between surface winds, currents, and waves. Processes that are driven by these interactions range from regional to global scales and happen in coastal areas (e.g., coastal upwelling and land-sea breeze), open ocean (e.g., inertial currents and mesoscale eddies) and marginal ice-zones (e.g., sea ice drift). Multiple components of the observing system including in situ (e.g. surface drifters, wave buoys, and moorings) and remote sensing (e.g, HF-radar and satellites) platforms are also illustrated (from **?**).

comprehensive observations and modeling of wave-current interactions are mostly limited to either tidal or large-scale currents (e.g., Wang et al., 1994; Irvine and Tilley, 1988; Masson, 1996), and a lot remains unknown about how waves and currents interact when both fields are highly variable, such as near ocean fronts and eddies (Ardhuin et al., 2012; Romero et al., 2017, 2020).

The California Current System (CCS) region is one of the most well-sampled regions of the ocean. It is continuously monitored by multiple observational platforms, such as HF radars,

gliders, wave-buoys, satellite remote sensing, and ocean moorings. The general structure of the CCS consists of a broad and weak equatoward flow that starts offshore of 150 km (the California Current), and two narrow poleward flows inshore of 150 km, one surface-intensified (the Inshore Countercurrent), and the other subsurface-intensified (the California Undercurrent). The poleward flows develop and intensify during late spring and summer as a result of coastal upwelling (Collins et al., 2000). Enhanced instabilities of the coastal upwelling current lead to intense meso and submesoscale activity, creating meanders, eddies, and jet-like features with typical surface velocities ranging from 40–80 cm s^{-1} (Di Lorenzo, 2003). Recent studies using both observations and numerical ocean models suggest that divergent motions associated with tides and inertia-gravity waves may contribute to a large portion of the surface kinetic energy (KE) (Qiu et al., 2017; Rocha et al., 2016a; Bühler et al., 2014a). Several regions in the ocean are marked by strong seasonal cycles in KE (Rocha et al., 2016b; Qiu et al., 2018). In the CCS region, for example, KE is mostly dominated by balanced (rotational) motions in late winter/spring, while divergence is stronger in late summer/fall (Chereskin et al., 2019).

Strong modulations of the surface wave field by meso and submesoscale features have been observed across upwelling jets off the California coast and meanders in the Loop Current region (Romero et al., 2017, 2020). These modulations resulted in high inhomogeneity of the wave field, enhancing nonlinear effects such as wave-breaking, and producing spatial gradients of up to 30% in the significant wave height (H_s, the average of the highest one-third of the waves). Recent case studies based on numerical simulations in the Gulf Stream and the Drake Passage (Ardhuin et al., 2017) also suggest that surface currents dominate the variability of H_s at scales smaller than 200 km, and that both the intensity and spatial structure of these currents significantly modulate the wave field.

The wave field off the California coast is also characterized by strong seasonal variability with higher waves in the winter and lower waves in the summer. Munk and Traylor (1947) described waves reaching La Jolla as belonging to five different types depending on the forcing

associated with typical meteorological situations. During winter, storm systems originating in the northeastern Pacific generate long-period waves that approach La Jolla from WNW directions, which the authors classified as type A. Some of these winter systems propagate closer to shore generating intermediate-period waves that come from W to NW directions (type B). During summer, very long-period waves from the Southern Hemisphere approach La Jolla from S to SW directions (type D). Additionally, the authors noted that La Jolla is also exposed to short-period waves generated by local low-pressure regions in spring (type E), as well as by the edge of the North Pacific High in summer (type C). Here, we build on the results from these authors by extending their analysis to the entire California coast and by quantifying their predictions. We characterize the seasonal and intra-annual variability of distinct wave types and describe how their contribution to the total wave field vary spatially along the coast.

1.1 Dissertation outline

This dissertation is comprised of three independent manuscripts that study different aspects of the interaction of surfaces waves with winds and currents. Chapter 2 focuses on the effects of local winds on surface waves. In particular, we characterize the seasonal variability of the deep-water surface wave field in the California Current region, as retrieved from over two decades of satellite altimetry data combined with wave buoys and wave model hindcast (WAVEWATCH III). Additionally, we assess the extent to which the local wind modulates the variability of the significant wave height, peak period, and peak direction. We find that during spring and summer, regional-scale wind events of up to 10 m/s are the dominant forcing for waves off the California coast, leading to relatively short period waves (8-10 s) that come predominantly from the north-northwest.

In Chapter 3 we shift our focus to the effects of currents on waves. We use a multiple-scale expansion approach to average the wave action balance equation over an ensemble of

sea-surface velocity fields characteristic of the ocean mesoscale and submesoscale and derive an expression for a diffusivity tensor of surface wave action density. We express the action diffusivity in terms of the kinetic energy spectrum of the flow. Applying a Helmholtz decomposition to the surface currents we show that, to leading order, the potential component of the surface velocity field has no effect on the diffusivity of wave action: only the vortical component of the surface velocity results in diffusion of surface wave action. Our analytic results for the action diffusivity by Monte Carlo ray-tracing simulations are validated through an ensemble of stochastic velocity fields.

Finally, the theory developed in Chapter 3 for monochromatic waves is further explored using numerical wave modeling for a wave spectrum characteristic of ocean swell. In Chapter 4, we use an ensemble of synthetic currents to force the wave model WAVEWATCH III and assess the relative impact of current divergence and vorticity in modifying several properties of the waves, including direction, period, directional spreading, and significant wave height (H_s). We find that the spatial variability of H_s is highly sensitive to the nature of the underlying current and that refraction-caused vorticity in the rotational component of the flow is the main mechanism leading to gradients of H_s. The results obtained using synthetic currents were used to interpret the response of surface waves to realistic currents by running an additional set of simulations using the llc4320 MITgcm output in the California Current region. Our findings suggest that wave parameters could be used to detect and characterize strong gradients in the velocity field, which is particularly relevant for the Surface Water and Ocean Topography (SWOT) satellite as well as several proposed satellite missions.

Chapter 2

Characterization of the Deep–Water Surface Wave Variability in the California Current Region.

2.1 Introduction

Surface gravity waves are a primary source of turbulence in the upper ocean, playing a major role in the exchange of momentum, heat, energy, and gasses between the ocean and the atmosphere (Sullivan et al., 2004; Cavaleri et al., 2012). These waves are the route for over 90% of the energy transferred from the wind to the ocean (Sverdrup and Munk, 1947; Ferrari and Wunsch, 2008), and wave breaking is believed to be the main mechanism forcing the ocean's wind-driven circulation (Donelan, 1998; Sullivan et al., 2004). The evolution of the surface wave spectrum during the onset of a storm is set by the input of energy from the wind, the energy loss due to wave breaking, and the transfer of energy between different frequency bands via nonlinear wave-wave interactions (Phillips, 1980). Strong winds blowing over long fetches originate long-period waves, known as swell, that can propagate great distances away from their source (Snodgrass et al., 1966); hence, the surface wave field in a given region

results from the combined response to both local and remote forcing.

The surface wave variability in the California Current region is largely affected by broad-scale atmospheric patterns, such as the El Niño Southern Oscillation (ENSO), the Pacific Decadal Oscillation (PDO), and the Pacific North American pattern (PNA) (Bromirski et al., 2005, 2013; Adams et al., 2008). For instance, higher wave heights (Adams et al., 2008) and wave power (Bromirski et al., 2013) in the northeastern Pacific are associated with the warm phase of the PDO. These effects are enhanced during El Niño years, which leads to higher risk of coastal flooding and beach erosion. Although many efforts have been made to characterize long-term trends and the interannual to decadal variability of the wave climate in the northeastern Pacific (e.g., Seymour et al., 1985; Seymour, 1996; Bromirski et al., 2005), the role of regional-scale forcing in modulating the wave field in this region remains unclear.

Alongshore winds off the California coast are established during late spring/early summer by the pressure gradient between a thermal low over the western United States and the North Pacific high (Zemba and Friehe, 1987; Koračin et al., 2004). At this time of the year, these upwelling-favorable winds lead to a low-level inversion that caps the marine atmospheric boundary layer (MABL) at heights lower than the coastal topography, such that the atmospheric flow is channeled. As these alongshore winds approach a cape, regions of compression (deceleration) are expected to develop upwind of the cape, followed by regions of expansion (acceleration) downwind of it (Winant et al., 1988; Koračin and Dorman, 2001; Taylor et al., 2008). A series of capes along the California coast together with the regional-scale coastline configuration allows a succession of such "expansion fan" winds to occur, leading to high wind speeds in May/June (Koračin and Dorman, 2001; Koračin et al., 2004). While swells originated in the Southern Ocean are known to be an important source of wave variability in the California region during summer, their energy gets dissipated along the way (Ardhuin et al., 2010, 2009) leading to small significant wave height (H_s, the average height of the highest one-third of the waves). Thus, high winds linked to expansion fans may play a major role as a local forcing for the wave field.

Even though the horizontal scales of surface waves are much smaller than the 10–km footprint of present satellite altimeters, they can produce a sea state bias (SSB) in the altimeter measurements and may impact the retrieval of the sea surface height (SSH) (Fu and Glazman, 1991; Peral et al., 2015). The SSB is generally decomposed into instrumental error and electromagnetic (EM) bias, both associated with the fact that the distribution of wave heights in the ocean is not exactly Gaussian (Fu and Glazman, 1991; Melville et al., 1991). While the instrumental error is attributed to the design of the altimeter itself, the EM bias is intrinsic to the way that the radar pulse interacts with the sea surface. As a result, the accuracy of SSH measurements from altimetry is directly limited by the effect of surface waves. Theoretical models of the EM bias predict a linear relationship between the EM bias and H_s; however, other characteristics of the sea state, such as the degree of wave development (wave age), the wind speed, and the direction of the waves with respect to the satellite boresight, contribute to the EM bias. Thus, as satellite altimeters evolve towards resolving finer scales, precise knowledge of the wave field is key to understanding how surface waves may contribute to the error budget of SSH measurements, and this information is relevant for the planning of future missions such as the Surface Water and Ocean Topography (SWOT) satellite.

Most earlier studies on surface wave variability in the California Current region have relied either on point measurements from wave buoys (e.g., Seymour, 1996; Bromirski et al., 2005), which lack spatial coverage, or output from wave models (e.g., Wang and Swail, 2001; Adams et al., 2008; Bromirski et al., 2013), which is subject to the model physics representativeness. Remote sensing satellites provide a complementary tool to infer the spatial structure of the wave field, and they provide a robust way to gain information on the H_s climatology. In the present work, we characterize the regional-scale intra-annual variability and the main driving mechanisms of the surface wave field in the California Current region by combining measurements retrieved from over two decades of satellite altimeter data with wave buoys, and a wave model hindcast. In particular, we assess the seasonal variability of significant wave height, period, and direction at several locations off the California coast, including one of the

potential sites for the calibration and validation of SWOT. We focus on offshore deep-water waves; investigation of processes happening close to the coast is left for future studies.

2.2 Data and Methods

2.2.1 Multimission Along-track Altimeter Data

Altimeters are active instruments that estimate the distance to a given target by measuring the two-way time of a microwave radar pulse. Assuming that the distribution of sea surface heights within the temporal and spatial scales of such a pulse is mostly due to surface gravity waves and that the distribution of wave heights in the ocean is approximately Gaussian (Pierson, 1955; Longuet-Higgins, 1963), H_s can be estimated from the average waveform of the return pulse (Brown, 1977).

Since 1992, several satellite altimeters have made it possible to observe H_s at global scales (Young et al., 2011), yet the lack of homogeneity between measurements from different missions poses a challenge in obtaining reliable long-term H_s time series (Queffeulou, 2004; Zieger et al., 2009). Discrepancies between missions arise from differences in the type of sensors as well as electronics drift, which can potentially introduce biases compromising the quality of the data. To address this issue, Queffeulou (2004) used cross-comparison of altimeter and buoy data to produce a homogeneously validated and calibrated dataset consisting of over twenty years (1992–2016) of along-track H_s measurements from nine different altimetry missions. This product is distributed by The French Research Institute for Exploitation of the Sea (IFREMER) and is publicly available for download. The analyses of satellite-based H_s in the present work were performed after daily averaging the along-track measurements into regular $1^\circ \times 1^\circ$ bins. To minimize the effects of land contamination and inaccurate tidal corrections (Bouffard et al., 2008), only measurements in regions deeper than 100 m and at least 20 km away from the coast were considered.

Table 2.1: Station ID, station name, position, depth, and time span of the selected CDIP wave buoys along the California coast as well as the calibration and validation site for SWOT (as shown in Figure 2.1).

Station ID	Station Name	latitude	longitude	depth [m]	time span
calval	calval	35.4 N	125.4 W	4561	1992–2016
168	Humboldt Bay	40.896 N	124.357 W	120	2010–2017
094	Cape Mendocino	40.294 N	124.731 W	333	2004–2017
029	Pt. Reyes	37.948 N	123.467 W	550	1997–2017
157	Pt. Sur	36.341 N	122.101 W	366	2009–2017
071	Harvest	34.454 N	120.783 W	548	1998–2017
167	S. Nicolas Isl.	33.499 N	119.489 W	1571	2008–2013
191	Pt. Loma South	32.529 N	117.421 W	1143	2008–2017

2.2.2 Buoy Measurements

Even though satellites are a useful source of wave height observations, they fail to provide frequency and directional information, which is essential to fully understand the variability of the surface wave field. To complement our analysis, we selected wave buoys from the Coastal Data Information Program (CDIP; http://cdip.ucsd.edu/) at water depths greater than 100 m along the California coast (Table 2.1). We have opted to use CDIP buoys exclusively, because they operate with Datawell Directional Waverider buoys, which are known to have better directional measurements in comparison to the 3-meter discus buoys from the National Data Buoy Center (O'Reilly et al., 1996). From the buoys that meet the depth requirement, we analyze only those with at least five years of data, and we select them to be separated by at least 0.5° in latitude and longitude. When multiple buoys are located within a 0.5° radius, we retain the one farthest offshore and with the longest record.

CDIP buoys provide historic quality-controlled timeseries of integral wave parameters such as significant wave height (H_s), peak frequency (f_p), and peak direction (D_p), as well as the first four angular moments (a_1, b_1, a_2, and b_2), which can be used to estimate the surface wave directional spectrum (Longuet-Higgins et al., 1963; Long, 1980). The peak frequency is defined as the frequency at which the wave energy spectrum reaches its maximum, and the peak direction is the wave direction at the peak frequency.

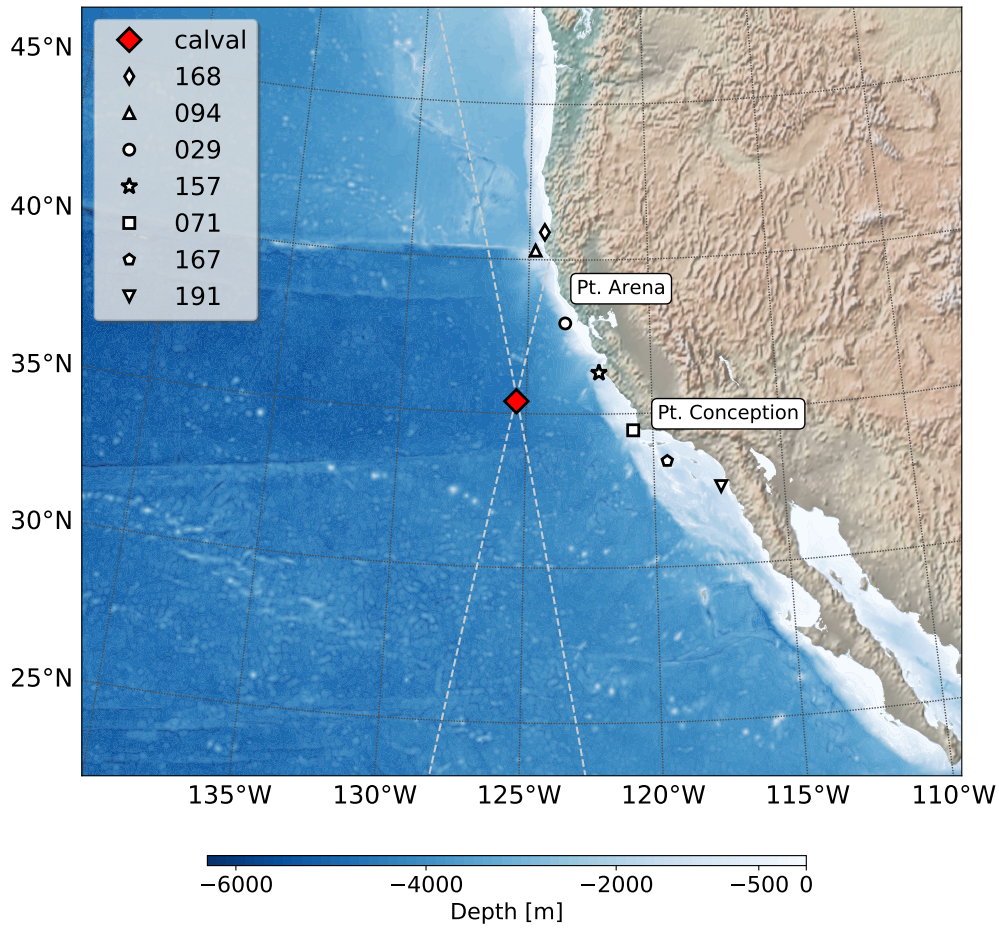

Figure 2.1: Location of the CDIP buoys (white), potential calibration and validation site for SWOT (red diamond), and calibration and validation orbit nadir ground track of SWOT (dashed gray). All the wave buoys are at depths greater than 100 m. The color map shows the local bathymetry in meters.

The directional spectrum of the surface wave field $E(f,\theta)$ represents the density of the sea surface variance at each frequency (f) and direction (θ). The integral of $E(f,\theta)$, i.e. the total variance of the surface elevation, is related to the significant wave height by:

$$H_s = 4\left(\int_{-\infty}^{\infty}\int_{0}^{2\pi} E(f,\theta)\,df\,d\theta\right)^{1/2}. \tag{2.1}$$

Thus, if one is interested in describing the significant wave height associated with a particular frequency and direction band, one may split the directional spectrum into N partitions such

that:

$$H_{s_i} = 4\left(\int_{f_{1i}}^{f_{2i}}\int_{\theta_{1i}}^{\theta_{2i}} E(f,\theta)df\,d\theta\right)^{1/2}, \tag{2.2}$$

with

$$H_s = \left(\sum_{i=1}^{N} H_{si}^{\,2}\right)^{1/2}. \tag{2.3}$$

In Section 2.3.4, we use the maximum entropy method (MEM) (Lygre and Krogstad, 1986) to compute the directional spectra from the angular moments measured by the selected buoys, and investigate the H_s variability of multiple partitions as in equation (2.2).

2.2.3 Wave Model Hindcast

Assessments of wave models show reasonable agreement with observations (Bidlot et al., 2002; Cox and Swail, 2001), which makes such models useful tools to bridge the gap between the sparseness of point measurements from wave buoy and the satellite limitation of measuring only H_s. In this study, we complement our analysis with a global wave parameter database (Rascle and Ardhuin, 2013) developed using one of the state-of-the-art spectral wave models, WaveWatch III (WW3) (WAVEWATCH III Development Group, 2009), forced by NCEP Climate Forecast System Reanalysis Reforecast (CFSR) winds. The simulations for this database span from 1994 to 2012 and were carried out at 0.5° spatial resolution, using a spectral grid with 32 frequencies and 24 directions and saving outputs every 3 hours. Grid points at water depth shallower than 100 m or within 20 km of the coastline were not considered in our analysis. We refer the reader to Rascle and Ardhuin (2013) for further details on the model set-up and validation.

2.3 Results and Discussion

2.3.1 Significant Wave Height Variability

For the sake of consistency, the analysis of satellite–based H_s presented hereinafter was performed over the same time span as the wave model hindcast (1994–2012); however, there are no significant changes in the results when using the entire altimetry database (1992–2016, not shown). Monthly maps of H_s in the California Current region from altimeter measurements reveal a clear seasonal cycle with higher waves occurring during the boreal winter (Figure 2.2). Average H_s varies between a maximum of 4.5 m in January, in the offshore region north of 40°N, and a minimum of 1.1 m in August in the entire domain. Additionally, except for August, the average H_s at the SWOT calval site is greater or equal to 2 m, the threshold specified for the projected SWOT performance (Peral et al., 2015). From late fall to early spring there is a nearly zonal demarcation in H_s with higher waves in the northern portion of the domain decreasing southward, a hallmark of winter cyclone/anticyclone systems that propagate from the northwestern Pacific into the Aleutian Low region, as suggested by earlier studies (e.g., Adams et al., 2008; Bromirski et al., 2005, 2013). Monthly averages of H_s from the WW3 hindcast result in the same overall variability, with wave heights from WW3 having a small bias ($\sim \pm 10$ cm) relative to both altimetry and buoy data (Supporting information Figure S1 and S2). An interesting feature of Figure 2.2 is a rather localized region of $H_s \geq 2$ m near the coast from May to July. This feature starts to develop in April as a narrow band of $H_s = 2.5$ m, becoming broader and weaker ($H_s = 2$ m) in May, and very localized around central/northern California through June and July, extending ~ 500 km offshore (closed oval contour of $H_s = 2$ m).

Figure 2.3 shows monthly averages of H_s (curves) and D_p (vectors) at the SWOT calval site (Figure 2.3a), and at the selected CDIP buoy sites (Figure 2.3b–h). Because we have no wave buoy at the SWOT calval site, we show H_s from altimeter observations at the nearest neighbor (light red), together with average H_s (dark red) and D_p from the WW3 hindcast

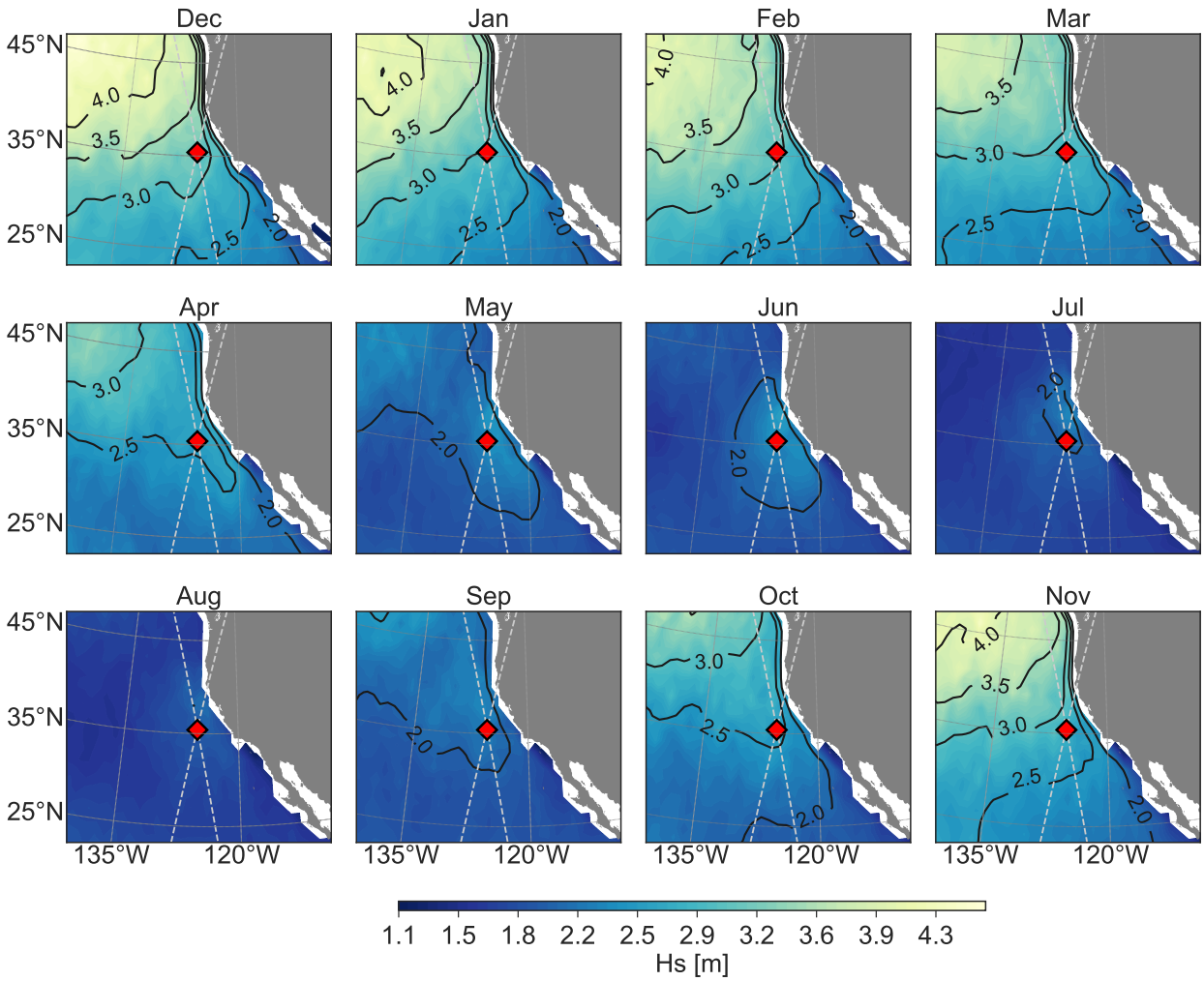

Figure 2.2: Monthly average maps of significant wave height off the California coast from altimeter measurements between August 1994 and August 2012 (colors and contours). The dash lines show the nadir ground track of SWOT's calibration and validation orbit and the red diamond, one of the potential calibration and validation sites for SWOT.

(Figure 2.3a). Hereinafter the wave direction will follow the meteorological convention, such that 0° means that waves are coming from the north, 90° waves are coming from the east, and so on. For each location, the standard error of the mean H_s (shade) changes from month to month depending on the number of months considered in the average, as well as variations of the standard deviation. For example, buoy 167 (Figure 2.3f) has a much larger standard error due to its relatively short record.

As in Figure 2.2, the overall seasonal variability of H_s is marked by an annual cycle that

peaks during boreal winter, with H_s of up to 3.1 m at the northernmost buoy sites. At buoys 167 and 191, however, the maximum average is observed in April. The absolute minimum H_s for all sites occurs in August, and the annual mean (dashed horizontal line) is greater than 2 m, except at buoys 167 and 191. Even though a winter–to–summer decrease in H_s is expected, the fact that the seasonal variability deviates considerably from a sinusoidal cycle is somewhat surprising.

Instead of decreasing monotonically throughout the spring and summer, there is either a local maximum or a plateau in H_s that can be observed along central/northern California in May–July (e.g. Figure 2.3d). This feature is apparent in monthly averages from all three data sets (altimetry, buoy, and wave model) for latitudes north of 33° N and south of 42° N (Supporting information Figure S3). Average D_p is predominantly from the WNW to NW

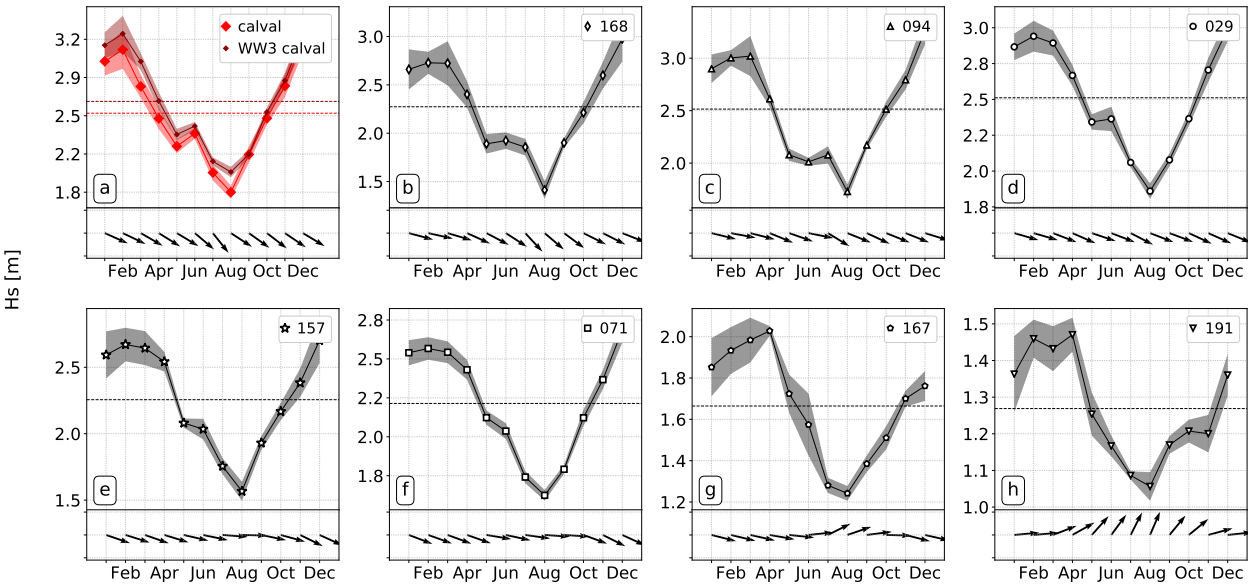

Figure 2.3: Monthly averages of significant wave height (H_s) from altimeter data at the SWOT calval site (red) and from the selected CDIP buoys (black), along with the respective averaged peak direction (D_p, black arrows). For the SWOT calval site, we computed the average D_p from the WW3 hindcast. In that case H_s from WW3 is also shown as a reference (panel a, dark red). The standard error of the mean is shown as a shade, and the annual mean for each curve is plotted as a dashed horizontal line. The station ID is indicated on the top right of each plot and the plots are organized from the northernmost buoy (168, panel b) to the southernmost (191, panel h). Note the different vertical axis from panel to panel.

year-round at the SWOT calval site and at buoys 168, 094, and 029 (Figure 2.3a–c). In late spring and summer, at buoys 157 and 071 (Figure 2.3d–e), peak direction shifts to waves coming from the W, while south of Point Conception (buoys 167 and 191) spring and summer waves come predominantly from the SW to WSW.

2.3.2 Peak Direction and Peak Period

One might hypothesize that the plateauing of H_s in May–July is due to an increase in south swell generated by winter storms in the Southern Ocean that propagate all the way to the California coast (Snodgrass et al., 1966). To investigate this hypothesis, we take as an example CDIP buoy 029, which has a relatively long record and is within the $H_s = 2$ m contour in Figure 2.2 (June).

Figure 2.4 shows joint histograms of H_s, peak period ($T_p = 1/f_p$), and D_p from CDIP buoy 029 for measurements in December–February (top) and May–July (bottom). During boreal winter (top), the distributions are predominantly unimodal with most waves coming from the W to NW ($270^\circ \leq D_p \geq 315^\circ$), with significant wave heights between 2 m and 4 m, and peak period between 12 s and 15 s. In late spring and early summer the picture is rather different: Even though remotely generated south swell ($180^\circ \leq D_p \geq 215^\circ$) is relatively frequent in May–July (bottom left of Figure 2.4d), the majority of the waves with $H_s \geq 2$ m come from the NW ($315^\circ \leq D_p \geq 330^\circ$). From Figure 2.4f, we also note that these waves from the NW have a rather short period ($T_p \leq 10$ s), which suggests that they are locally generated wind waves. In contrast, the distribution of longer-period waves ($T_p > 12$ s), is concentrated around directions between 180° and 215°, characteristic of south swell. The results shown in Figure 2.4 for buoy 029 reinforces the idea that waves off central and northern California come predominantly from the W to NW during boreal winter and from the WNW to NW during May–July.

To assess the spatial variability of wave direction and period throughout the year, we computed monthly average maps of D_p and T_p from the WW3 hindcast (Figure 2.5 and 2.6).

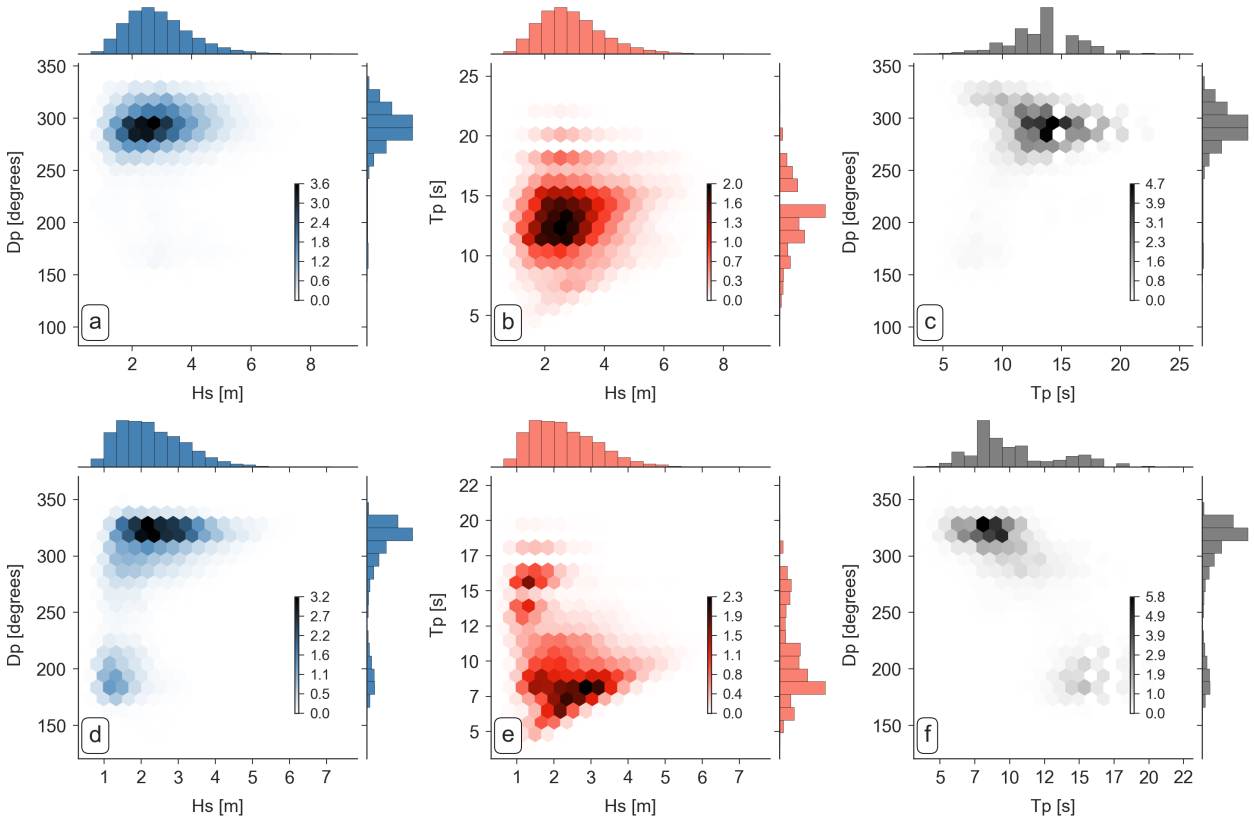

Figure 2.4: Joint histograms from CDIP buoy 029 for measurements during December–February (top) and May–July (bottom) of peak direction (D_p) and significant wave height (H_s) (blue, panels a and d), peak period (T_p) and significant wave height (red, panel b and e), and peak direction and peak period (black, panels c and f). The colorbar shows the number of points scaled by 10^3.

Figure 2.5 shows that from October to April, waves come, on average, from directions between the W (270°) and N (360°) in the entire domain (consistent with Figure 2.4a,c). In May, waves from the S to SW start to dominate at longitudes west of 125°W and latitudes south of 35°S, becoming more from the SE to S in late summer. Even though we would expect a dominance of waves with a south component from late spring to summer, we observe that east of 125°W the average D_p remains from the WNW to NW from May to September, which could also be seen in Figure2.4d. This somewhat isolated region of waves from the NW (blue/purple region embedded into yellow/orange) is particularly evident in June–August, when storms in the Southern Hemisphere are more frequent. Note also that the region of waves from the NW overlaps with the region having $H_s \geq 2$ m in May–July in Figure 2.2. As expected from

Figure 2.3f–g, the average D_p maps show that in a small region onshore and south of Point Conception the mean wave direction is from the SW in spring/summer.

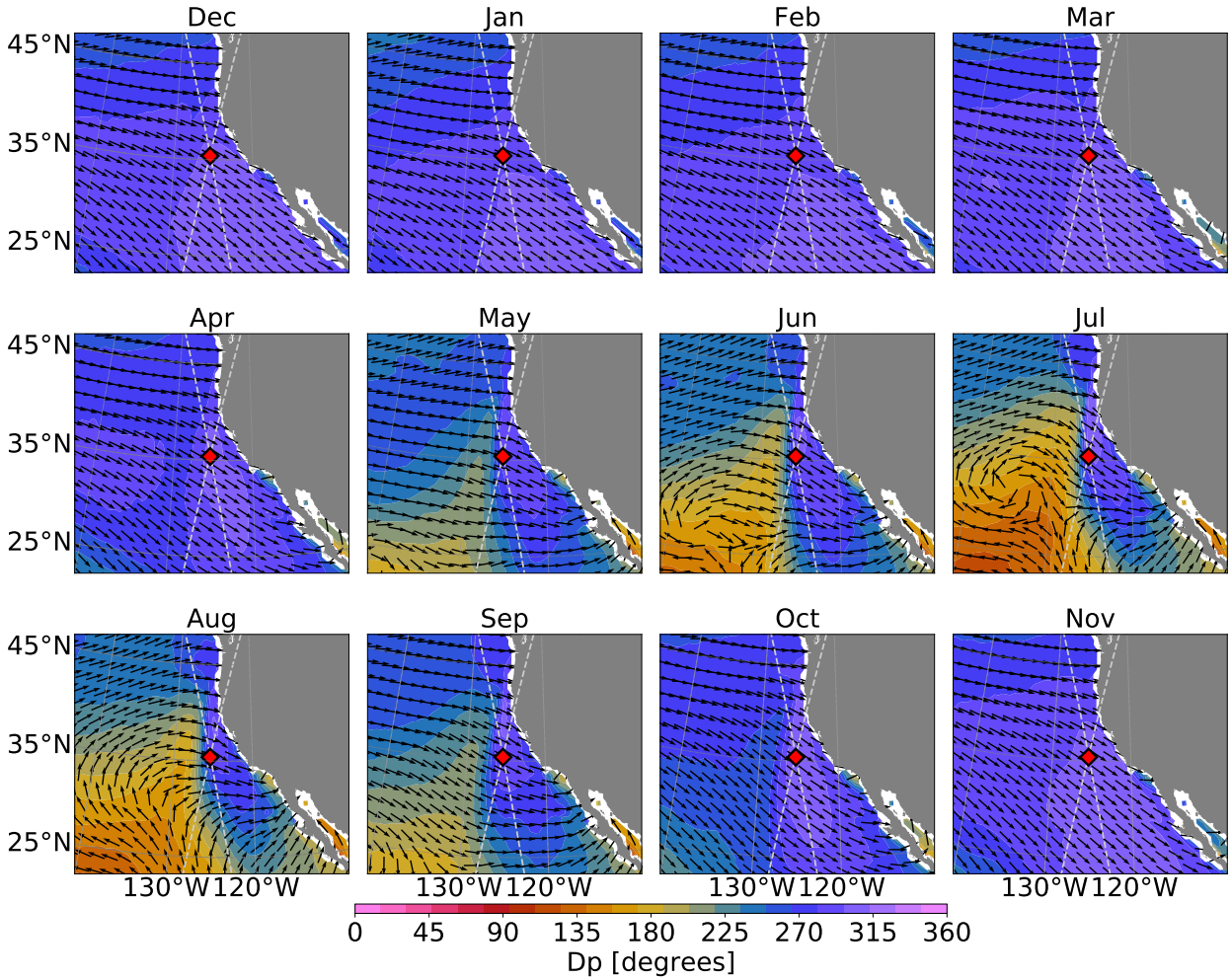

Figure 2.5: Monthly average maps of peak direction (D_p) off the California coast from the WaveWatch III hindcast (colors and vectors). The direction follows the meteorological convention, such that zero degrees means waves coming from the North and 90 degrees, waves coming from the East.

Monthly maps of peak period (T_P) are shown in Figure 2.6. From late fall to early spring the average T_p is dominated by intermediate to long-period waves ($T_p \geq 12$ s). Because during this time most waves are associated with storms propagating from the Gulf of Alaska, the average T_p is slightly lower in the northern portion of the domain and increases with distance from the source region. A spatial pattern similar to the one observed in the H_s and D_p averages for June is also apparent in the T_p map for that month. Despite the evidence

of long-period south swell south of Point Conception in late spring/summer, a well-defined region of $T_p \leq 10$ s characterizes the maps of average peak period between 33°N–42°N.

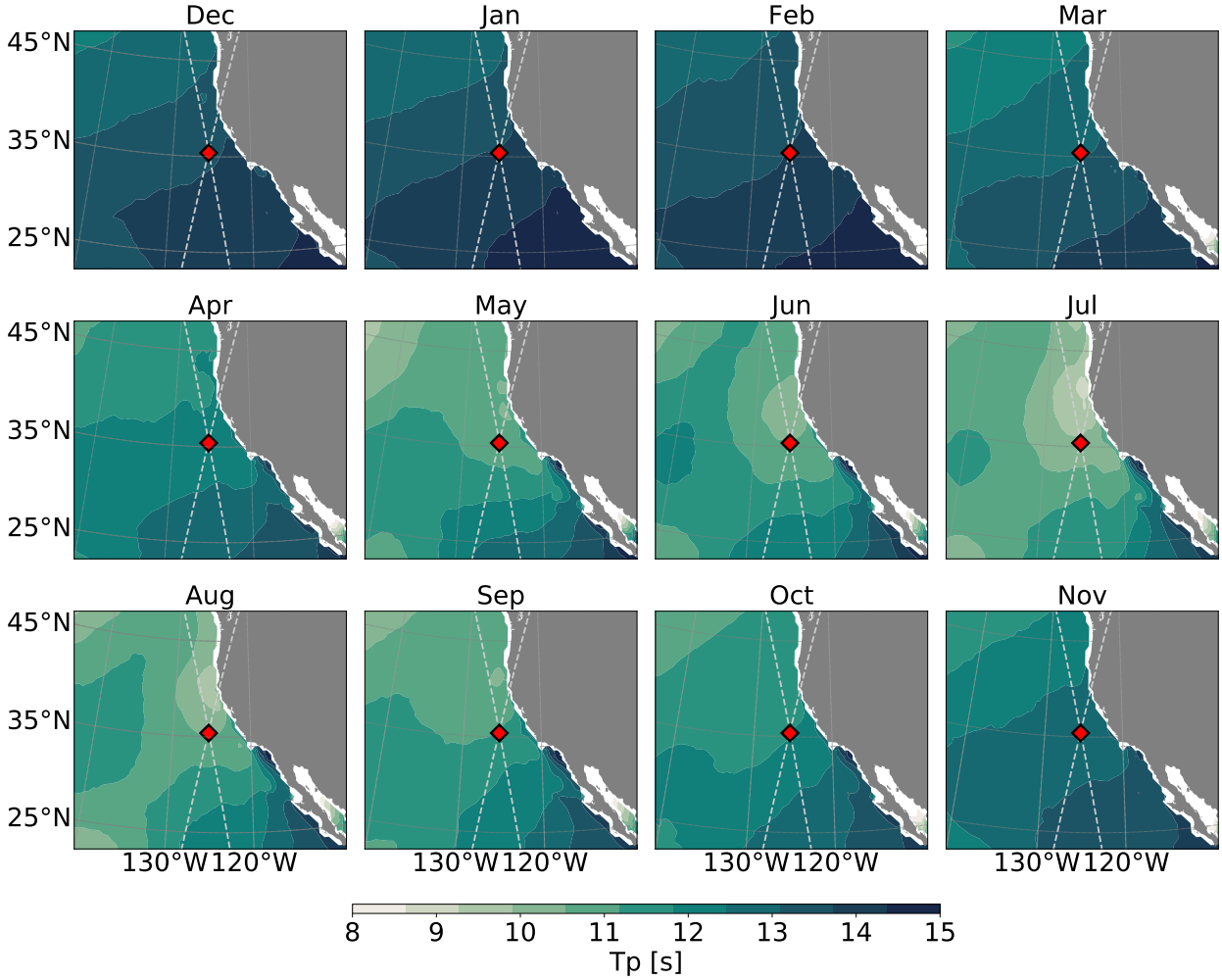

Figure 2.6: Monthly average maps of peak period ($T_p = 1/f_p$) off the California coast from the WaveWatch III hindcast.

2.3.3 Variability of the Wind Forcing

The surface wave field in a given region is set by the combination of local and remote forcing. To investigate the importance of the regional-scale wind field to the surface wave variability off the California coast we analyzed monthly averages of reanalysis 10 m winds ($\vec{U}_{10}$) from CFSR between 1994 and 2012, the same wind product used to force the WW3

hindcast. Monthly maps of wind speed ($U_{10} = \sqrt{u_{10}^2 + v_{10}^2}$) and direction are shown in Figure 2.7.

During boreal winter the wind field in the eastern Pacific is mostly influenced by two major pressure systems: the Aleutian low (centered at about 50°N, between the date line and 170°W) and the North Pacific high (centered around 30°N and 135°W) (Schroeder et al., 2013; Rodionov et al., 2005). These pressure systems drive stronger (7–8 m/s) southwesterly winds off the California coast north of 40°N and weaker (4–6 m/s) northwesterly winds south of 40°N (Figure 2.7, November–March). In spring/summer, the northward migration of the North Pacific high together with the development of a thermal low over the southwestern US shifts the mean wind towards a more northwesterly orientation along the entire California coast (Figure 2.7, April–July). As expected from previous studies (Halliwell and Allen, 1987; Taylor et al., 2008; Schroeder et al., 2013), Figure 2.7 (April–July) shows a clear signature of expansion fan winds, characterized by anomalously high (7–10 m/s) alongshore winds in central/northern California during spring/summer that extend $\sim$ 500 km offshore between 33°N and 42°N. Consistent with the simulations of Koračin et al. (2004), the wind structure in June that we observe is marked by two major cape-scale expansion fans: one off Point Arena ($\sim$ 38°N) and the other off Point Conception ($\sim$ 34° N), together with a California-scale expansion fan (7 m/s contour in Figure 2.7, June). Enhanced wind speeds right off Point Conception start in April, followed by a region of persistent low wind speeds further south, where the coastline orientation changes by roughly 90°, becoming nearly east–west oriented.

Monthly averages of wind speed at the SWOT calval site and the selected CDIP buoys may provide further insight on the role of local and remote wind forcing. Given the lack of anemometers on the CDIP wave buoys, we compute the averages using the CFSR winds at the nearest neighbor of the calval site and wave buoy locations. CFSR winds in the northeast Pacific have been shown to have good agreement in respect to both NOAA wave buoys and satellite altimeters (e.g., Chawla et al., 2013; Rascle and Ardhuin, 2013; Stopa and Cheung, 2014).

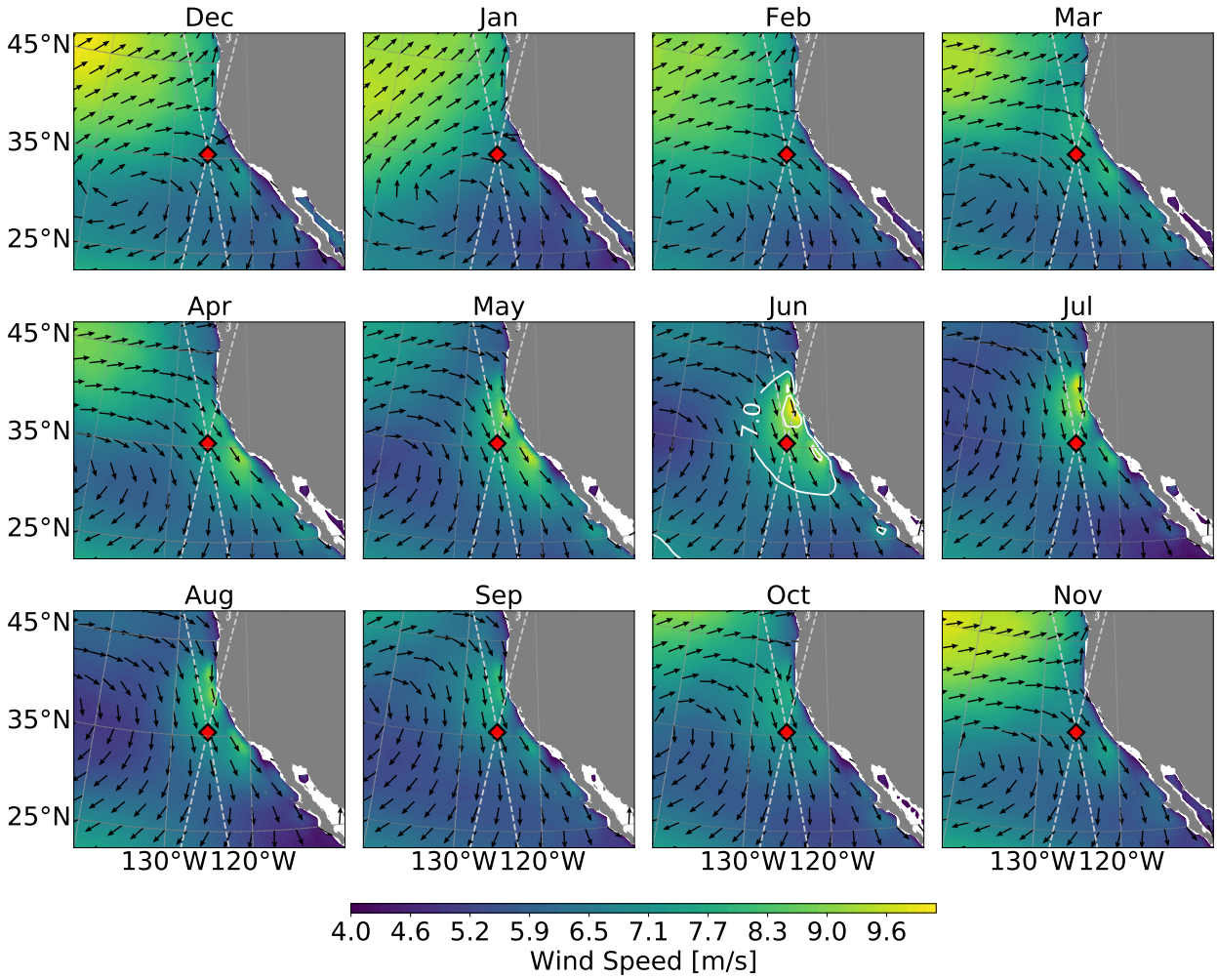

Figure 2.7: Monthly average maps of the wind field off the California coast from the CFSR reanalysis. The wind speed is shown in the colormap and the direction as normalized vectors. Note the development of a localized high-wind speed region from late spring to late summer near the California coast associated with expansion fan winds. A California-scale expansion fan is marked by the 7 m/s contour in June

As we can see in Figure 2.8, the seasonal variability of the wind speed has a strong geographic dependence. At sites north of Point Conception, we observe maximum average wind speeds of 7–9 m/s in May–July (Figure 2.8a–f), while at buoys 167 and 191 the wind speed peaks in April. This geographic pattern of stronger surface wind speed in April at regions south of Point Conception was also observed by Winant et al. (1988). As the North Pacific high strengthens and moves northward at the beginning of spring, winds in southern California tend to peak earlier than in central/northern California. The 50% increase in wind

speed from buoy 157 to buoy 071 is a good example of a deceleration area upwind of Point Conception, followed by expansion fan winds in the immediate lee of it.

Monthly averages of wind direction are shown in the bottom of each panel in Figure 2.8. At buoys 168 and 094 winds during boreal winter are predominantly southerly. In April, winds start veering clockwise, becoming nearly alongshore (northwesterly) by late spring/summer. Wind directions between Point Reyes and Harvest (Figure 2.8c–e) are predominantly northwesterly year-round, while south of Point Conception (Figure 2.8f–g) the winds shift to westerly in spring/summer. This shift in wind direction south of Point Conception is associated with the abrupt change in the coastline orientation, which causes the flow to separate (Harms and Winant, 1998). Figures 2.7 and 2.8 show that average wind speeds off the California coast are higher in spring/summer, with wind directions being predominantly alongshore (northwesterly) in central/northern California, and onshore (westerly) in southern California. For a state of equilibrium between winds and waves, Pierson and Moskowitz

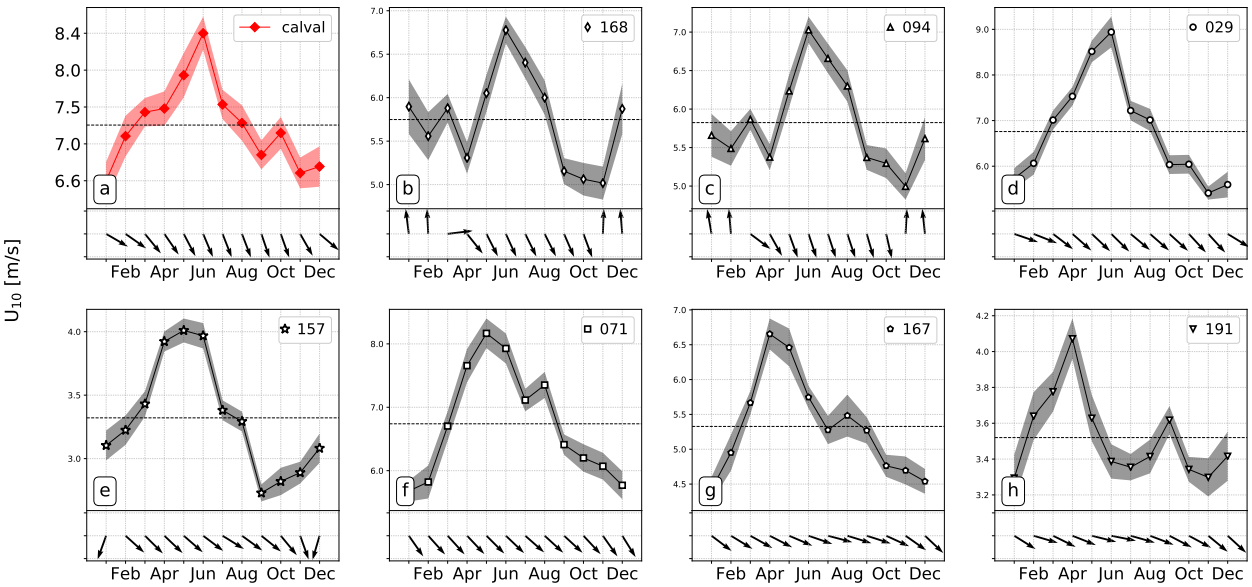

Figure 2.8: Monthly averages of wind speed from the CFSR reanalysis at the nearest neighbor of the SWOT calval site (red) and of the selected CDIP buoys (black). The standard error of the mean is shown as a shade, and the annual mean for each curve is plotted as a dashed horizontal line. The station ID is indicated on the top right of each plot and the plots are organized from the northernmost buoy location (168, panel b) to the southernmost (191, panel h). Note the different vertical axis among the plots. In the bottom of each panel, the monthly average wind direction is ploted as black arrows.

(1964) have shown that integral spectra parameters such as H_s and f_p tend to asymptotic values that are a function of the wind speed only, such that:

$$f_p = 0.13 \left(\frac{g}{U_{10}} \right), \tag{2.4}$$

where f_p is the peak frequency, g is the acceleration due to gravity, and U_{10} is the wind speed at 10 m. From the dispersion relationship for deep-water waves, the phase speed (c_p) at the peak frequency can be written as:

$$c_p = \frac{g}{2\pi f_p}. \tag{2.5}$$

Thus, at full development, i.e. when the surface wave spectrum becomes stationary, equations (2.4) and (2.5) are usually combined to a constant (Alves et al., 2003):

$$\frac{c_p}{U_{10}} = 1.2 \tag{2.6}$$

The ratio between the phase speed of the waves and wind speed (equation 2.6) is often referred as the "wave age" and provides a metric for the degree of development of the wave field. For $c_p/U_{10} \leq 1.2$, the wave field is dominated by wind-sea, in these conditions, momentum is transferred from the wind to the waves, such that the wave field is highly coupled to the local winds. Conversely, sea states with $c_p/U_{10} > 1.2$ are associated with remotely generated swell that travel at speeds faster than the local wind and do not absorb as much momentum.

Figure 2.9 shows monthly averages of the fraction of days dominated by locally generated waves ($c_p/U_{10} \leq 1.2$) computed using c_p and U_{10} from the WW3 hindcast. We can see that swell-dominated sea states are ubiquitous year-round. The overall average fraction of wind-waves is lower than 0.05, which is consistent with the global estimates of Hanley et al. (2010). However, Figure 2.9 suggests that this fraction can be much higher at regional scales. In the region where expansion fan winds are characteristic, periods of swell-dominated sea states are interspersed with wind-sea, which leads to a fraction of locally generated waves as high

as 50% in spring/summer, reinforcing the importance of local winds to the variability of the surface wave field off the California coast.

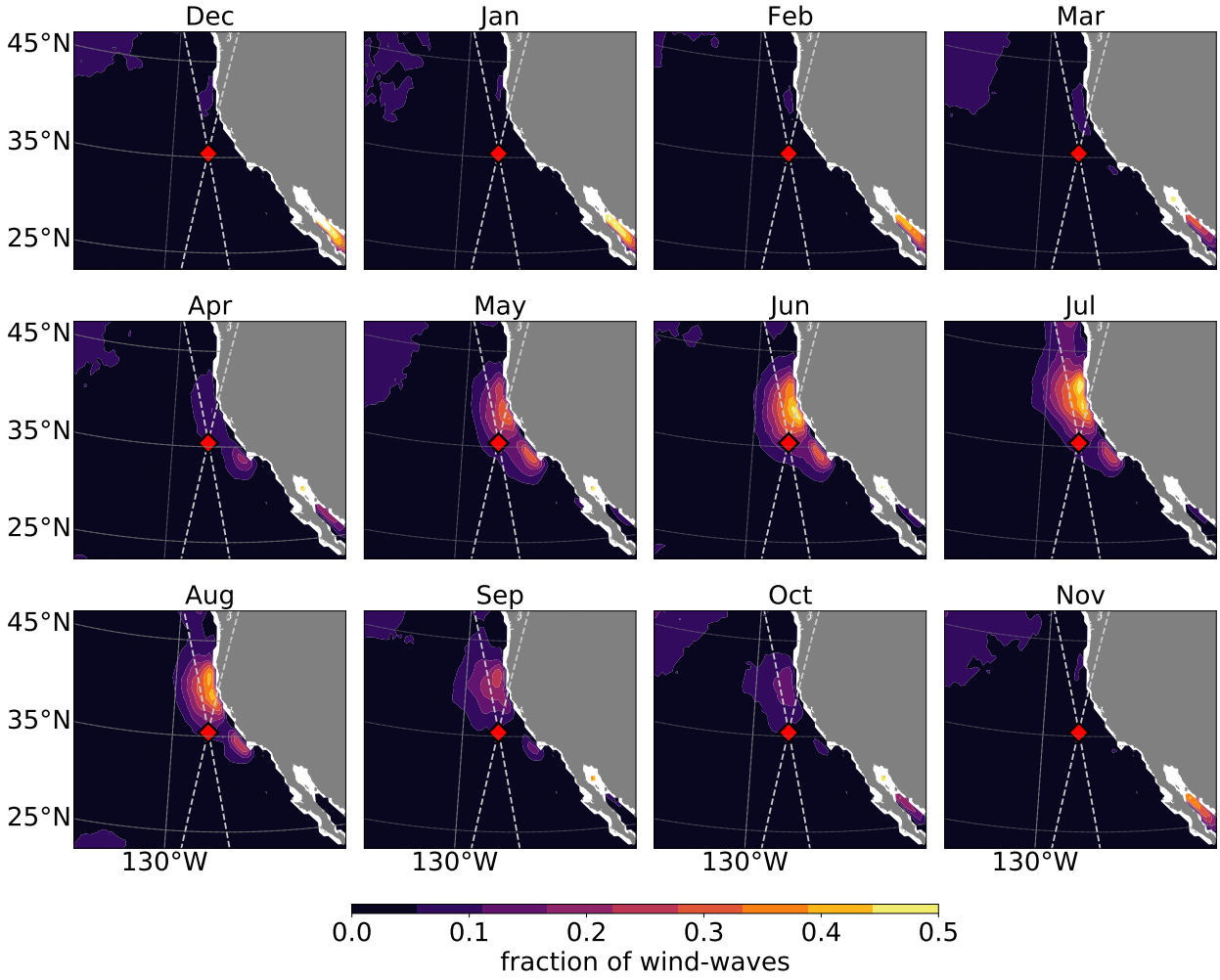

Figure 2.9: Monthly average of the fraction of days with $c_p/U_{10} \leq 1.2$, which is associated wind-sea dominated sea states. The monthly maps were computed using peak phase speed and wind speed from the WW3 hindcast.

2.3.4 Directional spectrum partitions

CDIP buoys provide frequency and directional information for the wave field. This allows the wave energy spectrum to be partitioned into specific bands of period and direction, and it permits a quantification of the H_s associated with each partition (see Section 2.2.2). Munk and Traylor (1947) proposed five major "wave types" associated with typical meteorological

Table 2.2: Thresholds used for separating the directional spectra into seven partitions, using equation (2.2), as illustrated in Figure 2.10a. The timeseries for the partitions marked by a star are shown in the Supporting Information.

Partition name	Period [s]	Direction [degrees]
Expansion Fans	$10 \geq T \geq 5$	$270° \leq \theta \leq 360$
Winter Storms	$T \geq 12$	$240 < \theta \leq 360$
Intermediate Period	$12 > T > 10$	$135 \leq \theta \leq 360$
S. Hemisphere	$T \geq 12$	$135 < \theta \leq 240$
*Chop	$T < 5$	$0 < \theta \leq 360$
*East	$T \geq 5$	$135 < \theta < 360$
*Short S. Hemisphere	$12 > T \geq 5$	$135 < \theta < 270$

conditions to characterize waves reaching La Jolla, California. Here we modify their scheme in order to encompass a greater domain and add extra partitions, which better isolates the wave types that we aim to characterize. Note the thresholds used to define the partitions are subjective, despite being based on earlier studies (e.g., Munk and Traylor, 1947; Adams et al., 2008) and on the results discussed in sections 2.3.1–2.3.3. Similar methods of spectral partitioning have been recently implemented by Portilla-Yandún et al. (2016).

Table 2.2 shows the period and direction thresholds that we used for separating the directional spectra into seven partitions. The *Expansion Fans* partition comprises what we argue to be waves associated with regional-scale winds in spring/summer off the California coast. These waves have a relatively short period and are typically aligned with the wind, which spans directions from W to N. Longer period waves associated with the propagation of storm systems across the North Pacific are encompassed by the *Winter Storms* partition, whereas long-period waves generated by storms in the Southern Hemisphere are referred to as *S. Hemisphere*. To account for waves that could have been either locally or remotely generated we consider the *Intermediate Period* partition. Short-period waves ($T < 5$ s) from all directions are grouped in the *Chop* partition; waves in the same direction range as *S. Hemisphere*, but with period too short to be considered swell are accounted for by the *Short S. Hemisphere* partition; finally, the *East* partition accounts for waves coming predominantly from the east.

Figure 2.10 shows monthly average H_s at the selected CDIP buoys associated with the four partitions that are the most relevant to our discussion, namely *Expansion Fans*, *Winter Storms*, *Intermediate Period*, and *S. Hemisphere*. Curves for all seven partitions are available in the Supporting Information Figure S4. At all buoys, the H_s associated with winter cyclones/anticyclones systems in the North Pacific (*Winter Storms*, green) has a well-defined annual cycle, being nearly sinusoidal, with maximum values during winter and minimum during summer. Except for buoys 167 and 191, the seasonal variability from November to March is dominated by waves from the *Winter Storms* partition. The overall variability of the *Intermediate Period* partition (gray) is also marked by an annual cycle that peaks during boreal winter. However, the plateauing observed in Figure 2.3 is to some extent also present in the *Intermediate Period* curves, which would be expected since this partition accounts for a mix between locally and remotely generated waves. From April to October, the H_s associated with the *Intermediate Period* partition is comparable or slightly higher than the *Winter Storms*, but much lower than the *Expansion Fans*.

Even during summer, the average contribution of swell from the Southern Hemisphere (*S. Hemisphere*, blue) to the total H_s variability is nearly irrelevant when compared with the other partitions, except at Point Loma (buoy 191, Figure 2.10h), which is geographically more exposed to waves from this direction. However, if we focus on long-period waves only ($T \geq 12$ s), *S. Hemisphere* waves dominate over *Winter Storms* from late spring to late summer. So, even though we do observe some south energy at long-periods along the California coast, this band is associated with small wave heights. Waves from the *Expansion Fans* partition contribute the most to the total H_s between April and October, except at buoy 191, where the H_s from *Expansion Fans* is comparable to *S. Hemisphere*. It is interesting to note the correspondence between the monthly averages of wind speed from Figure 2.8 and the respective *Expansion Fans* partition. Such correspondence is the most evident at buoys in the immediate lee of the two major cape-scale expansion fans (Figure 2.7, June) namely, buoys 029 and 071. In the same way, the wind speed peaks up earlier in southern California (Figure

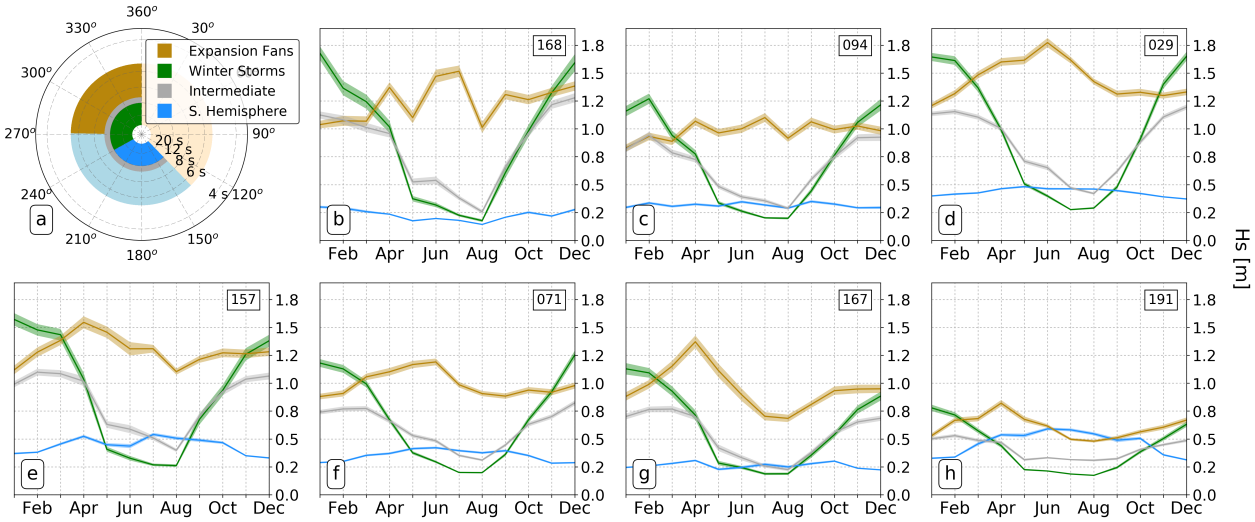

Figure 2.10: Monthly averages of significant wave height computed by integrating the directional spectra from CDIP buoys within different partitions, as illustrated on the top left panel. For the sake of clarity, we only show curves for the most relevant partitions, referred to as: *Expansion Fans* (10 s$\geq T \geq$5 s, $270° \leq \theta \leq 360°$, golden); *Winter Storms* ($T \geq 12$ s, $240° \leq \theta \leq 360°$, green); *Intermediate Period* (12 s$> T >$10 s, $135° \leq \theta \leq 360°$, gray), and *S. Hemisphere* ($T \geq 12$ s, $135° < \theta \leq 240°$, blue). The station ID is indicated on the top right of each panel. Curves for all seven partition are shown in the Supporting Information (Figure S4).

2.8 buoys 167 and 191), so does the H_s from the *Expansion Fans* partition. The partitioning of the directional spectra is artificial in the sense that it depends on arbitrary thresholds. Nonetheless, this approach shows that the highest wave heights in spring and summer off the California coast are associated with short-period (10 s$\geq T \geq$5 s) waves coming from the NW.

2.3.5 Implications for Satellite Altimetry

Comprehensive knowledge of the surface wave field is also relevant for the success of future altimetry missions such as SWOT. SWOT will map the ocean surface topography every 20 days via two parallel 50–km–wide swaths with 1–km pixel spacing, that will make it the first of its kind capable of resolving the submesoscale ocean SSH. The California Current region has been identified as one of the target regions for calibration and validation of SWOT (Figure 2.1), as pointed out in Wang et al. (2016); so, an accurate characterization of the wave field in this region could be readily used to complement the error budget analysis of Peral et al.

(2015), and to help interpret the SSH signal measured by SWOT. Figure 2.11 shows the

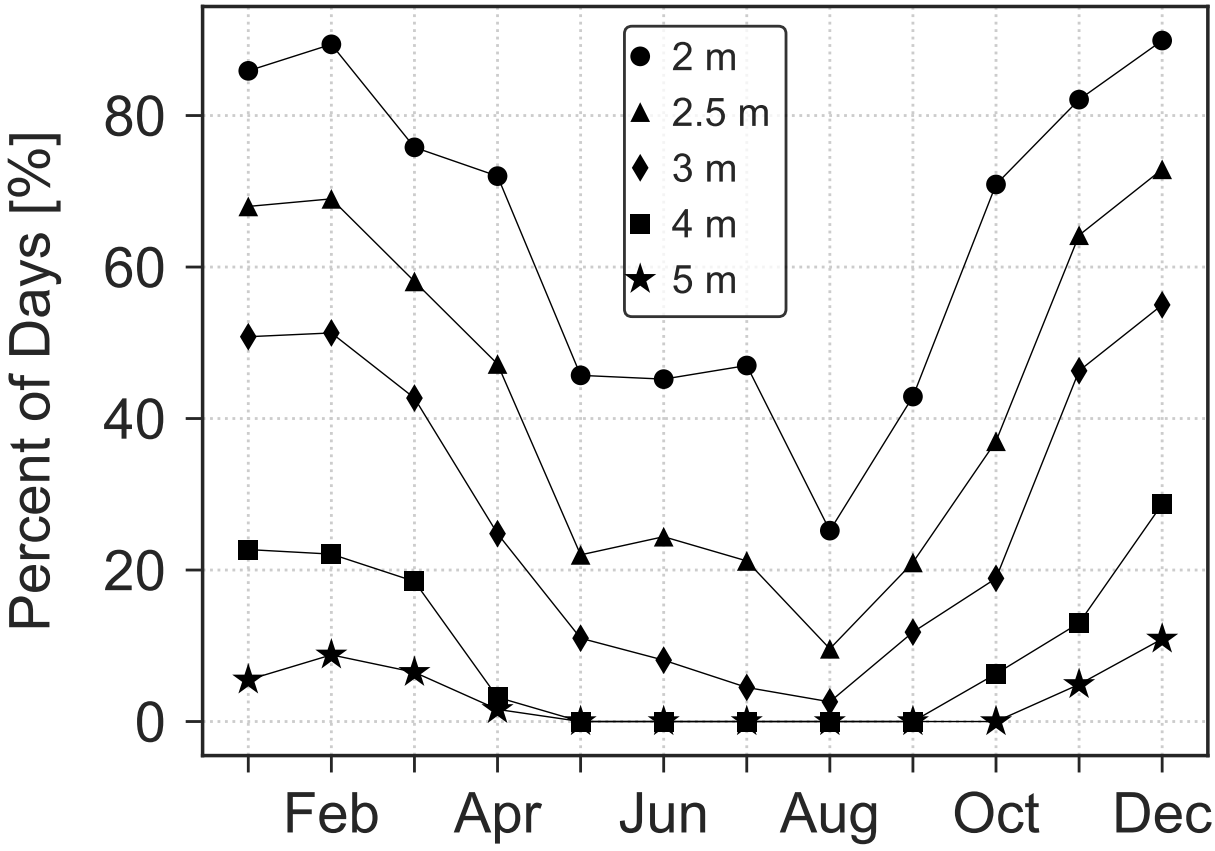

Figure 2.11: Average percentage of days per month on which the significant wave height at the SWOT calval site off the California coast (35.4°N, 125.4°W) is above a given threshold. The significant wave height used is from the altimeter database and spans from 1992 to 2016.

average percentage of days per month on which the H_s is above a given threshold at one of the potential calibration/validation (calval) sites for SWOT. The curves were computed based on 24 years of altimeter data, which means we have used the full time span of the altimetry dataset (1992–2016). Our results show that the H_s at the calval site is above the 2 m threshold specified for the projected SWOT performance on average over 60% of the time; however, this value can be as low as 25% in August. Peral et al. (2015) show that systematic sea surface height errors due to ocean surface waves are the dominant source of error on SWOT's SSH error budget for sea states with H_s higher than 4 m. Given that the surface

wave field in the California Current regions is highly variable, SWOT's performance may be degraded depending on the period that calibration and validation efforts take place. From Figure 2.11 we can see in December, for example, there is nearly 30% chance that a given H_s measurement will be above 4 m, whereas between April and September this chance drops to almost zero. The performance of SWOT will also depend on the relative angle between the

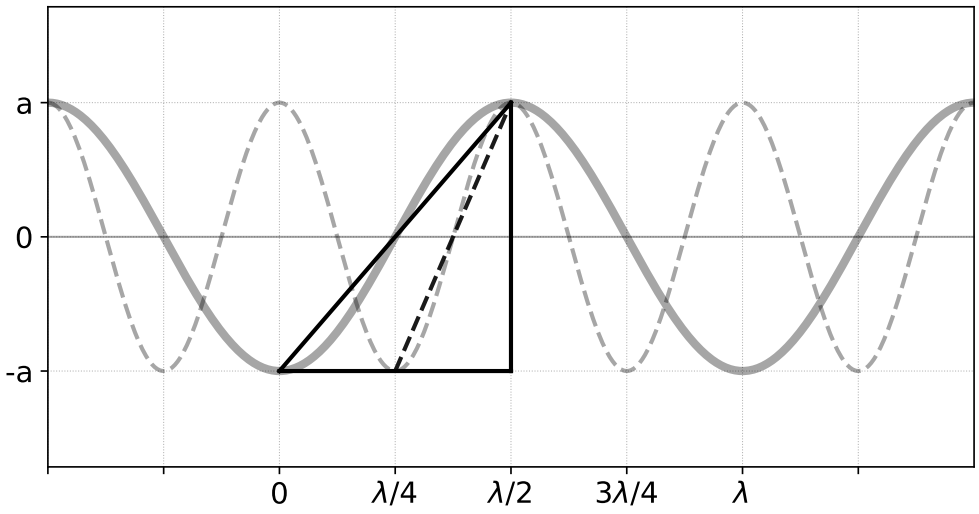

Figure 2.12: Schematic representation of the characteristic wave slope for two monochromatic waves with amplitude a, and wavelengh λ and $\lambda/2$, respectively. Here, the characteristic wave slope (α_{ch}) is defined as the angle relative to the horizontal of a straight line connecting the wave crest to the wave trough.

sea surface and SWOT's radar pulse. If the incidence angle of the radar pulse is shallower than the sea surface inclination, multiple points in the physical space may map onto the same point in the radar space, leading to an effect know as "layover" that distorts the measured sea surface with respect to the true sea surface (see Figure 3 of Peral et al. (2015)).

Figure 2.12 shows a schematic representation of a proposed proxy for the sea surface inclination due to surface waves. The scheme shows two monochromatic waves that have the same amplitude (a, distance from the crest/trough to the mean sea surface), but different wavelengths (λ and $\lambda/2$, respectively). We then define a *characteristic wave slope* (α_{ch}) as the angle relative to the horizontal of a straight line that connects the wave trough to the

wave crest, such that for the longer wave in Figure 2.12 we can write:

$$\tan(\alpha_{ch}) \equiv \frac{2a}{\lambda/2}. \tag{2.7}$$

As we can see from the scheme and equation (2.7), for a given amplitude, shorter waves are steeper than longer waves. We can then estimate a "bulk" α_{ch} from the integral wave parameters by assuming $H_s \sim 2a$ and taking the wavelength (λ) to be the wavelength at the peak frequency (λ_p):

$$\alpha_{ch} \sim \tan^{-1}\left(\frac{H_s}{\lambda_p/2}\right), \tag{2.8}$$

where

$$\lambda_p = \frac{g}{2\pi f_p^2}. \tag{2.9}$$

Figure 2.13 shows monthly average maps of the bulk α_{ch} computed from the WW3 hindcast. Note that both the spatial and temporal variability patterns of the average bulk α_{ch} closely match those for the average wind speed (Figure 2.7). We see that expansion fan winds in spring and summer lead to short-period and relatively high wave heights which, unsurprisingly, translate into higher bulk wave slopes. The look angle of SWOT in the near and far range will be approximately 4° and 1°, which is comparable to α_{ch}. Therefore, especially for the shallower look angle, locally generated wind-waves in spring and summer may increase layover effects, impacting the SSH retrieval.

Schwendeman and Thomson (2015) have shown that the variance of the surface slope, or the mean square slope (mss), which includes contributions from high-wavenumber surface roughness, correlates better with the wind forcing and whitecap coverage in comparison to the bulk wave slope. We have computed monthly averages of the mss from the WW3 hindcast and have found the correlation between the monthly bulk wave slope (Figure 2.13) and the monthly mss to vary between 0.79 and 0.93 (not shown).

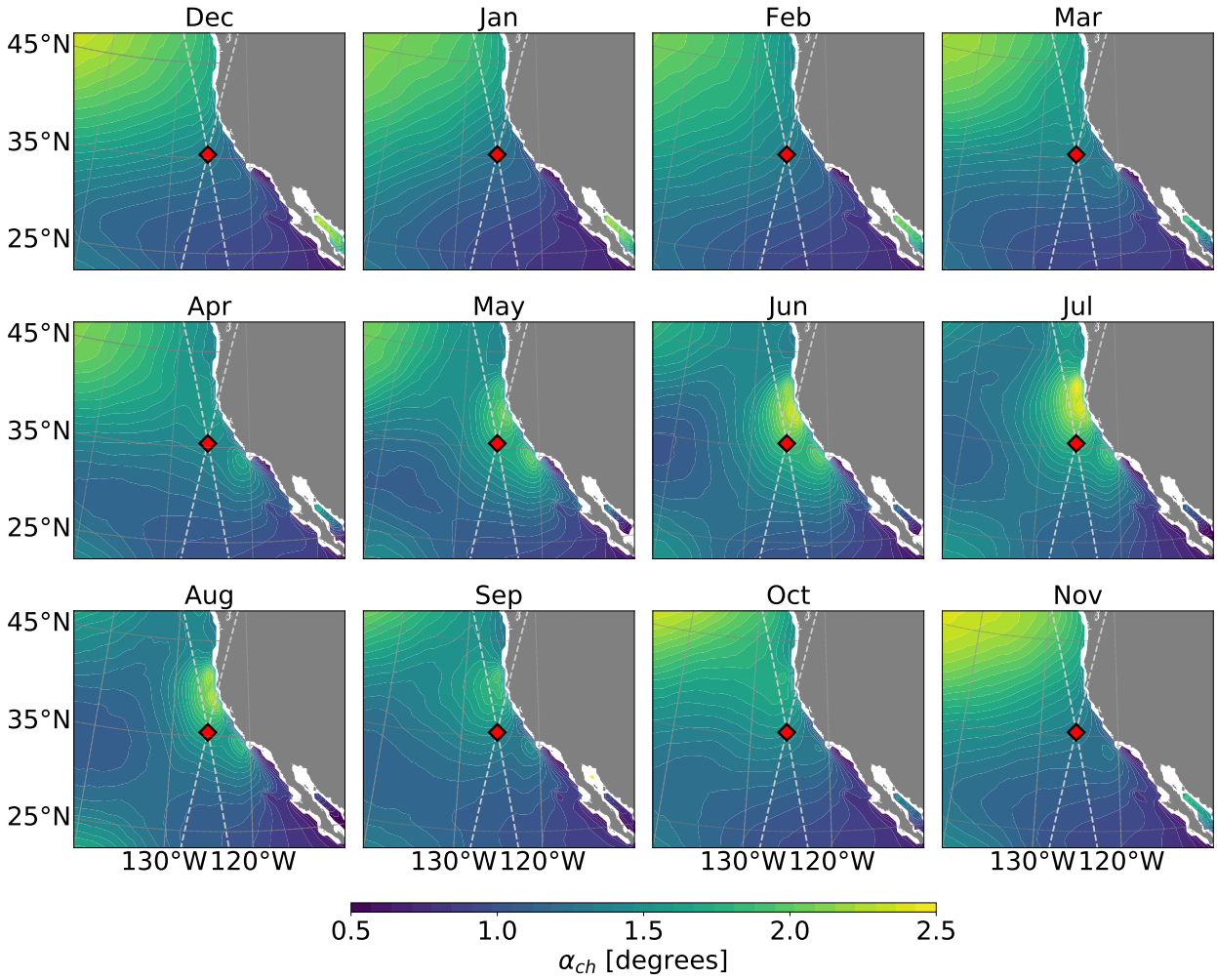

Figure 2.13: Monthly maps of average characteristic wave slope, computed using the significant wave height and peak period from the WW3 hindcast

2.4 Summary and Conclusions

A series of capes along the California coast together with the regional-scale coastline configuration allow a succession of "expansion fan" winds to occur. These winds appear as anomalously high (7–10 m/s) alongshore winds in central/northern California from April to July that extend 300–500 km offshore between 33° and 42°N. South of Point Conception, the wind speed peaks earlier in the spring, when wind directions become predominantly westerly (onshore). From analyzing significant wave height, peak period, and peak direction we have shown that expansion fans play a crucial role in determining the intra-annual variability of

the surface wave field in the California Current region. As a result, most high waves during spring/summer in central/northern California have relatively short-period ($T \leq 10$ s) and come from the northwest. By combining data from altimeter, wave buoy, and wave model hindcast, we were able to quantify both the spatial and temporal characteristics of the wave field and also build a thorough surface wave climatology.

The signature of the expansion fan winds projects onto monthly maps of H_s as a localized region of $H_s \geq 2$ m that is very well defined in June. The same spatial pattern appears on monthly maps of peak period and peak direction. Partitioning of the directional spectra from the CDIP wave buoys has confirmed the importance of local wind forcing to the significant wave height. Our findings show that the band of waves from directions between 270° and 360° and periods between 5 s and 10 s give the largest contribution to the total H_s between April and October at nearly all buoys.

The effects of surface waves on altimeter measurements are intrinsically dependent on the statistics of the sea state. Theoretical formulations of the sea state bias (SSB) rely on the fact that the distribution of wave heights is nearly Gaussian; however, the distribution of wave heights for locally-generated wind waves is fairly skewed (Fu and Glazman, 1991; Glazman and Pilorz, 1990, e.g.). We have found that during spring/summer, the wave field off the California coast is dominated by local wind-sea ($c_p/U_{10} \leq 1.2$) up to 50% of the time, which implies that the interpretation of the sea state bias might have to be revisited. It is also noteworthy that satellite altimetry is currently the only way to constantly monitor significant wave height at global scales. Given that the wave field is highly variable in both space and time, accurate regional-scale climatologies are key to continue improving satellite-based wave products. Finally, we have discussed the potential implications of the seasonal variability of the surface wave field to the calibration and validation efforts for the SWOT mission. Based on our results, significant wave height at the potential calval site has the highest probability ($\sim$70%) of being below the specified threshold for the projected SWOT performance in August, which would be the optimum time regarding H_s for calval to minimize

surface-wave-induced error. However, we have also shown that expansion fan winds cause the characteristic wave slope at the calval site to be the highest during late spring and summer, which might increase layover effects. Therefore, the contribution of surface waves to SWOT's error budget will be a trade off between smaller errors due to H_s in spring and summer, but higher errors associated with layover effects due to the wave steepness. As satellite altimeters evolve to resolve finer scales, knowing the wave field with precision may help the interpretation of sea surface height measurements at high wavenumbers and frequencies.

Supplemental Material

Introduction

Here we present four additional figures that support the results discussed in the main text. Figures S1-S3 compare the signicant wave height (Hs) retrieved from the CDIP wave buoys with satellite altimetry and the WaveWatch III (WW3) hindcast. The purpose of showing these figures is cross-comparison and to illustrate similarities and differences. For independent validation of these datasets the reader is referred to the original documentation of the respective products.

Monthly Average Significant Wave Height

Figure 2.S1 shows monthly average maps of significant wave height (H_s) from 18 years (1994–2012) of WaveWatch III (WW3) hindcast forced by CFSR winds. The colorbar used has the same limits as the one in Figure 2 of the main text. Except for a slightly positive bias in respect to the maps computed using satellite altimetry data, the WW3 hindcast reproduces the monthly H_s fairly well. It is noteworthy that the WW3 hindcast captures the two local maxima of H_s associated with expansion fan winds off the two major capes in June (small closed contours of $H_s = 2$m), which are not resolved in the altimetry maps.

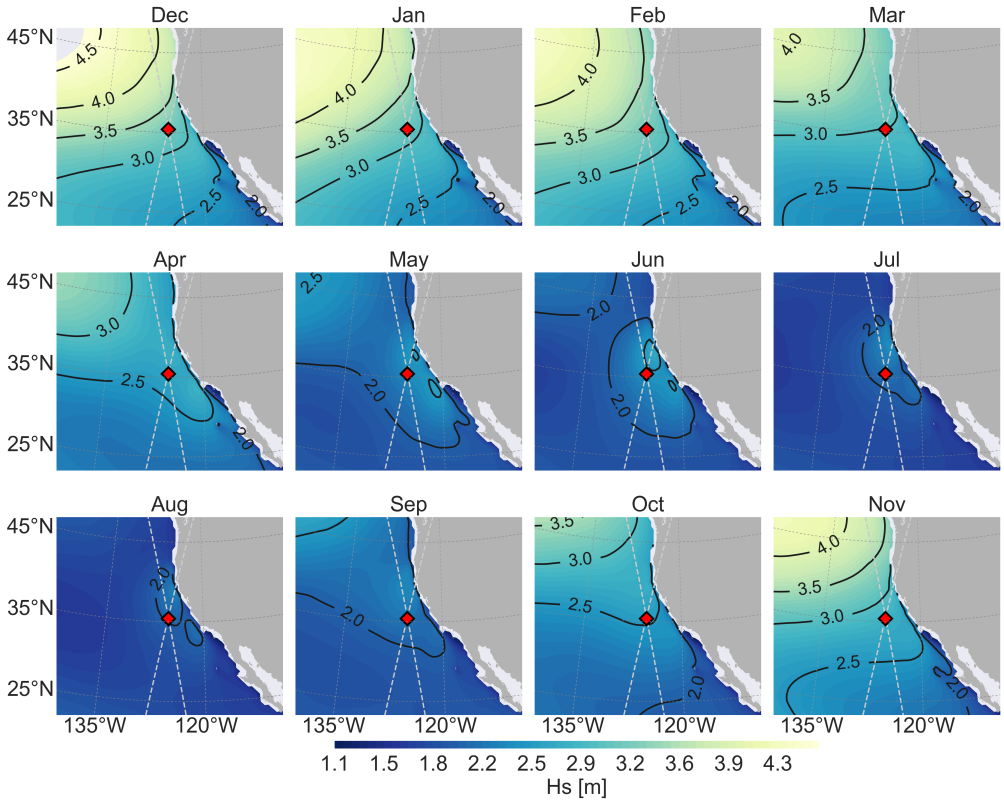

Figure 2.S1: Same as Figure 2 in the main text, but using significant wave height (H_s) from the WW3 hindcast. Note that monthly averages from the hindcast closely match the results obtained from altimetry, with the H_s from the hindcast having slightly higher values overall.

Comparison Between Satellite Altimetry, Wave Buoy, and the WaveWatch III Hindcast

Figure 2.S2 shows scatter plots comparing H_s measurements from CDIP wave buoys, satellite altimetry, and the WW3 hindcast. For consistency purposes, all data in the scatter plots are daily averages – since the altimeter measurements were averaged into daily $1^\circ \times 1^\circ$ bins. Correlation coefficients between the data sets are above 0.9 at nearly all buoy sites with relatively small biases (< 2 cm), indicating good agreement between the three datasets. Figure 2.S3 shows the monthly average H_s from CDIP wave buoys at the selected buoy sites and from altimetry and WW3 at the nearest neighbor. All three data sets reproduce the same overall seasonal variability despite small biases.

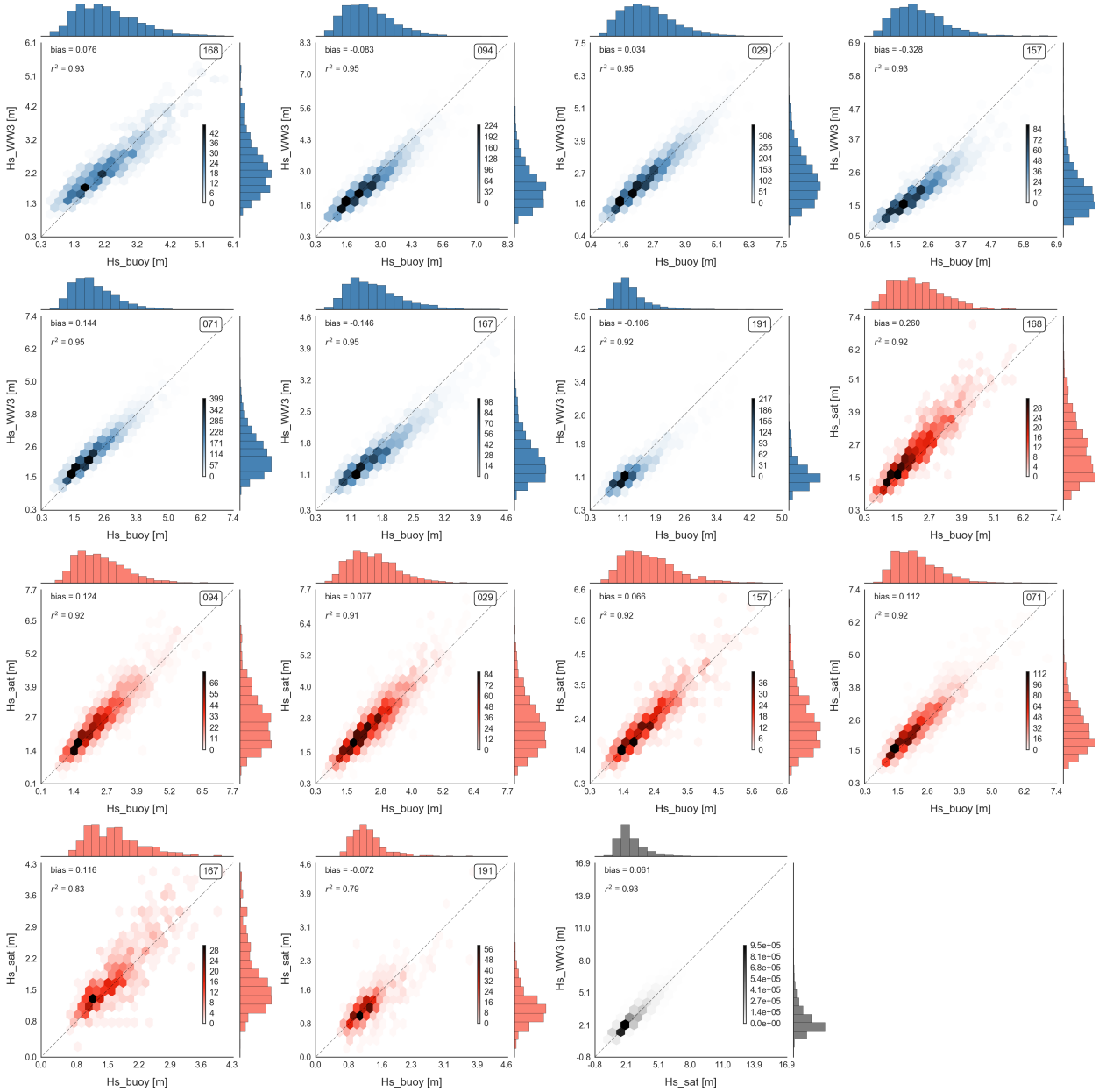

Figure 2.S2: Scatter plots comparing significant wave height (H_s) from the CDIP wave buoys, satellite altimetry, and the WW3 hindcast. The data from altimetry and WW3 were taken at the nearest neighbor of the buoy sites (see Figure 1 and Table 1, main text). The comparison between WW3 and altimetry was made in a grid-point-to-grid-point basis. Scatter plots of H_s from the WW3 hindcast against the CDIP buoys are shown in blue; satellite altimetry against CDIP buoys, are shown in red; and the WW3 hindcast against satellite altimetry is in black. The colorbar indicates the number of points.

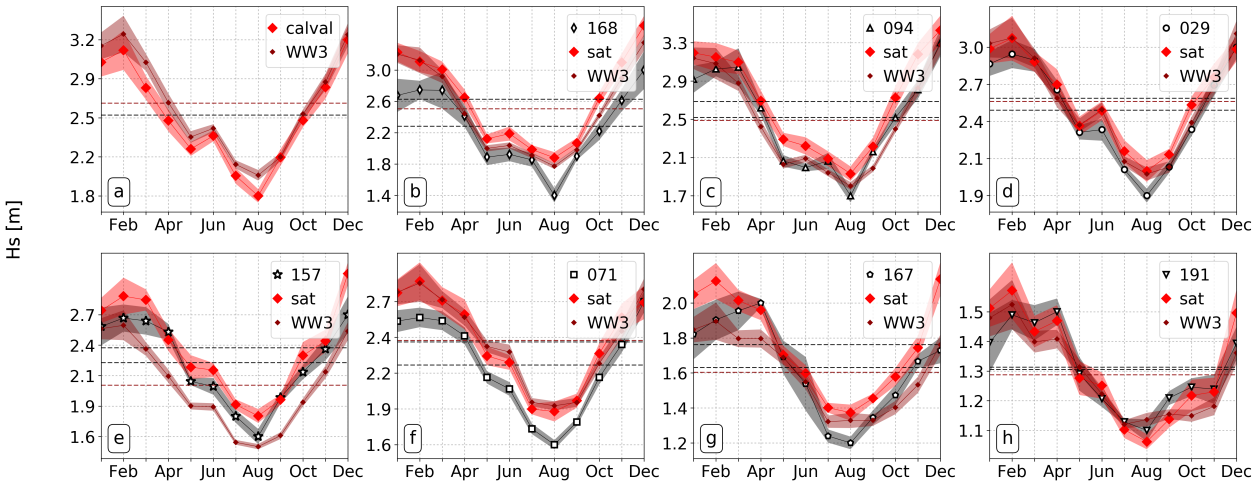

Figure 2.S3: Same as Figure 3 in the main text, but comparing the average H_s from the wave buoys (black), with the the average H_s from altimetry (red) and the WW3 hindcast (brown). The timeseries from altimetry and WW3 were taken at the nearest neighbor of the buoy sites.

2.5 Spectrum Partitioning

Figure 2.S4 shows the monthly average H_s of all 7 partitions used in our analysis. From the additional 3 partitions that are not shown in Figure 10 of the main text (*Chop, East,* and *Short S. Hemisphere*), the *Chop* partition (dashed gray) contributes on average with the highest H_s and is associated with extremely short period ($T < 5$ s) waves. We refer the reader to the main text for a detailed discussion on the partitioning methods. From Figure 2.S4, the average H_s of a particular month is obtained by taking the square root of the sum of the squared H_s of all 7 partitions.

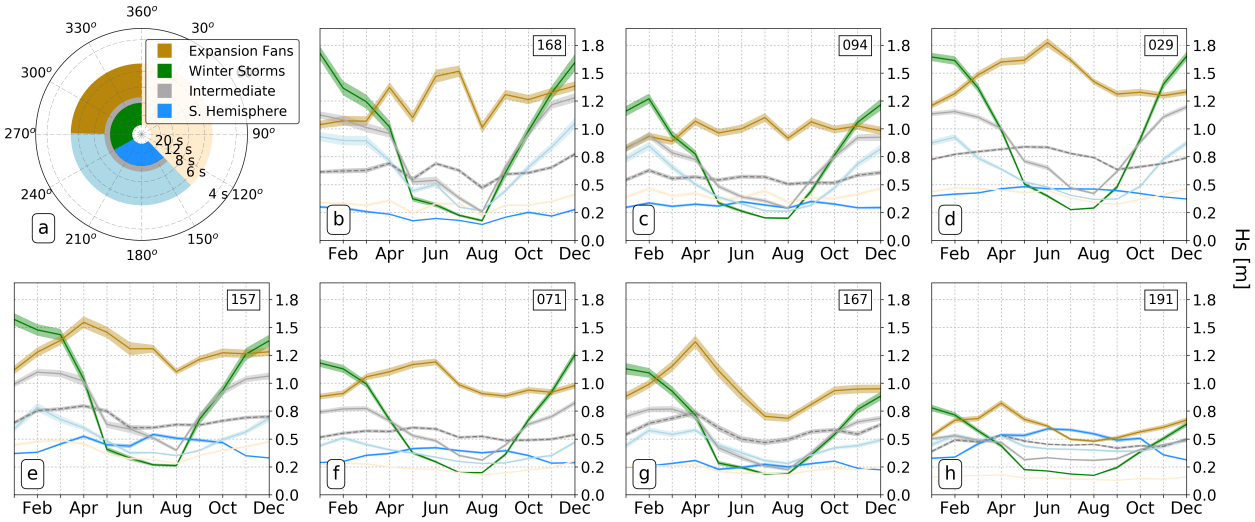

Figure 2.S4: Same as Figure 10 (main text), but showing the monthly averages of significant wave height for all partitions (see Table 2, main text). The additional partitions in comparison to Figure 10 are: *Chop* (dashed gray), *East* (light ivory), and *Short S. Hemisphere* (light blue).

Acknowledgments

This work was supported by the SWOT program with NASA grant NNX16AH67G and 80NSSC17K0326. BDC was partially funded by the ONR grant N000141512285. The authors thank the two anonimous reviewers for their comments and suggestions.The authors ackowledge the *Coastal Data Information Program* (CDIP) for providing the buoy data available from http://thredds.cdip.ucsd.edu and the *French Research Institute for Exploitation of the Sea* (IFREMER) for providing the WaveWatch III hindcast (ftp://ftp.ifremer.fr/ifremer/ww3/HINDCAST) and the altimeter surface wave database (ftp://ftp.ifremer.fr/ifremer/cersat/products/swath/altimeters/waves). ABVB is grateful to Reuben Demirdjian and Sean Crosby for fruitful discussions.

Chapter 2, in full, reprints material as it appears in Journal of Geophysical Research: Oceans, 2017, DOI:10.1002/2017JC013280. Ana B Villas Bôas, Sarah T Gille, Matthew R Mazloff, Bruce D Cornuelle. The dissertation author was the primary investigator and author of this paper.

Chapter 3

Directional diffusion of surface gravity wave action by ocean macroturbulence

3.1 Introduction

Surface gravity waves are an important route by which the ocean exchanges energy, momentum, heat, and gases with the overlying atmosphere (Cavaleri et al., 2012; Villas Bôas et al., 2019). Sea-surface currents modify the wavenumber, direction, and amplitude of surface waves, and affect the spatial variability of the wave field. The effect of currents on waves under the Wentzel-Kramers-Brillouin (WKB) approximation has been well studied (Kenyon, 1971a; Peregrine, 1976; White and Fornberg, 1998; Henderson et al., 2006; Heller et al., 2008; Gallet and Young, 2014). But the sparseness of ocean current observations makes it difficult to explicitly account for wave-current interactions in numerical surface wave models. Thus, instead of explicit resolving sea-surface currents, a statistical approach to the effect of currents on surface waves is required.

Recent studies of surface wave-current interactions suggest that the sea-state variability at meso- and submesoscales, here referred to as macroturbulence, is dominated by the variability of the current field (Ardhuin et al., 2017; Quilfen et al., 2018; Quilfen and Chapron, 2019).

At these scales, horizontally divergent motions associated with tides, inertia-gravity waves, and fronts contribute significantly to the surface kinetic energy (Bühler et al., 2014a; Rocha et al., 2016a; D'Asaro et al., 2018). If surface gravity waves respond differently to divergent than to rotational flows — and we show here that they do — then changes in the dominant regime of surface currents can result in significant changes in the surface-wave field. This offers the possibility that observations of surface gravity waves might be used to probe the structure of submesoscale ocean turbulence.

In the context of internal gravity waves, McComas and Bretherton (1977) showed how scale-separated wave interactions can be analyzed with the WKB approximation and understood as diffusion of wave action. The induced-diffusion approximation of McComas & Bretherton has recently been developed and extended by Kafiabad, Savva & Vanneste (2019, KSV, hereafter) to obtain an action-diffusion equation for the scattering of internal gravity waves by mesoscale ocean turbulence. Here we apply the KSV method to surface gravity waves. Crucial to this development is that the parameter

$$\epsilon \stackrel{\text{def}}{=} |\boldsymbol{U}|/c \tag{3.1}$$

is small; above $\boldsymbol{U}$ is the horizontal current at the sea surface and $c = \sqrt{g/4k}$ is the deep-water group speed at wavenumber k.

In section 3.2, and in appendix 3A, we use the formalism of KSV to derive an expression for a diffusivity tensor of surface wave action. In section 3.3 we consider the simplifications that result from assuming that the sea-surface velocity $\boldsymbol{U}$ has isotropic statistics. We show that the horizontally divergent component of $\boldsymbol{U}$ has no effect on action diffusivity: diffusivity results solely from the vortical (solenoidal) component of $\boldsymbol{U}$ and produces an angular diffusivity that is expressed as a weighted integral of the solenoidal part of the energy spectrum of $\boldsymbol{U}$ as in (3.28). Smit and Janssen (2019) have also examined the action diffusion of surface waves using a framework based on Lagrangian random walk theory. Section 3 discusses the differences

between Smit & Janssen's expression for the action diffusivity and ours. In section 3.4 the analytic results are tested with Monte Carlo ray-tracing through an ensemble of stochastic velocity fields.

3.2 The induced diffusion approximation

For linear deep-water surface waves, the Doppler-shifted dispersion relation is

$$\omega(t, \boldsymbol{x}, \boldsymbol{k}) = \sigma + \boldsymbol{k}\boldsymbol{U}(t, \boldsymbol{x}) \,, \tag{3.2}$$

where $\boldsymbol{k} = (k_1, k_2)$ is the wavenumber, $\sigma = \sqrt{gk}$ is the intrinsic wave frequency, with $k = |\boldsymbol{k}|$ and g the gravitational acceleration. Also in (4.1), $\boldsymbol{U}(t, \boldsymbol{x}) = (U_1, U_2)$ is the horizontal current at the sea-surface. Provided that $\boldsymbol{U}(t, \boldsymbol{x})$ is slowly varying with respect to the waves, i.e., the temporal scales of variations in the current field are longer and the spatial scales are larger than those of the waves, wave kinematics is described by the ray equations. Using index notation the ray equations are

$$\dot{x}_n = \partial_{k_n}\omega = c_n + U_n \,, \qquad \text{and} \qquad \dot{k}_n = -\partial_{x_n}\omega = -U_{m,n}k_m \,, \tag{3.3}$$

where $c_n = \partial_{k_n}\sigma(k)$ is the group velocity. Under the same assumptions, wave dynamics is governed by the conservation of wave-action density $A(\boldsymbol{x}, \boldsymbol{k}, t)$

$$\partial_t A + \dot{x}_n \partial_{x_n} A + \dot{k}_n \partial_{k_n} A = 0 \,, \tag{3.4}$$

with $\dot{x}_n$ and $\dot{k}_n$ given by (3.3) (Phillips, 1966; Mei, 1989).

We follow KSV and develop a multiple-scale solution, based on $\epsilon \ll 1$, that enables one to average (4.7) over the ensemble of velocity fields $\boldsymbol{U}$ (see appendix 3A). Assuming that the

statistical properties of $\boldsymbol{U}$ are stationary and homogeneous, one finds that

$$\partial_t \bar{A} + c_n \partial_{x_n} \bar{A} = \partial_{k_j} \mathsf{D}_{jn} \partial_{k_n} \bar{A} \,, \tag{3.5}$$

where $\bar{A}$ denotes the ensemble average of A. The diffusivity tensor D_{jn} in (3.5) is expressed in terms of the two-point velocity correlation tensor

$$\mathsf{V}_{im}(\boldsymbol{x} - \boldsymbol{x}') \stackrel{\text{def}}{=} \langle U_i(\boldsymbol{x}) U_m(\boldsymbol{x}') \rangle \ . \tag{3.6}$$

Because of the assumption of spatial homogeneity, V_{im} depends only on the separation $\boldsymbol{r} = \boldsymbol{x} - \boldsymbol{x}'$ of the two points. The most convenient formula for explicit calculation of D_{jn} is the Fourier space result

$$\mathsf{D}_{jn} = \frac{k_i k_m k}{4\pi c} \int q_j q_n \tilde{\mathsf{V}}_{im}(\boldsymbol{q}) \delta\big(\boldsymbol{q}\boldsymbol{k}\big) \mathrm{d}\boldsymbol{q} \,, \tag{3.7}$$

where $c = g/2\sigma$ is the magnitude of the group velocity and

$$\tilde{\mathsf{V}}_{im}(\boldsymbol{q}) = \int \mathrm{e}^{-\mathrm{i}\boldsymbol{r}\boldsymbol{q}} \mathsf{V}_{im}(\boldsymbol{r}) \, \mathrm{d}\boldsymbol{r} \tag{3.8}$$

is the Fourier transform of $\mathsf{V}_{im}(\boldsymbol{r})$. (In (3.7) and (3.8) the integrals cover the entire two-dimensional planes (q_1, q_2) and (r_1, r_2) respectively.) The diffusivity in (3.7) is the two-dimensional equivalent of (A7) in KSV. Our appendix 3A derivation, however, assumes only spatial homogeneity and stationarity of the velocity $\boldsymbol{U}$, and does not require incompressibility of $\boldsymbol{U}$.

One can verify from (3.7) that $\mathsf{D}_{jn} k_n = 0$ and therefore there is no diffusion of wave action in the radial direction in $\boldsymbol{k}$-space. Fast surface-wave packets propagate through a frozen field of macroturbulent eddies and thus preserve the absolute frequency $\sqrt{gk} + \boldsymbol{U}\boldsymbol{k}$. Because ϵ in (3.1) is small, the Doppler shift $\boldsymbol{U}\boldsymbol{k}$ is small relative to the intrinsic frequency $\sqrt{gk}$. Thus, at leading order, both σ and k, are constant. In other words, absolute frequency conservation,

together with $\epsilon \ll 1$, implies that there is no radial $\boldsymbol{k}$-diffusion in (3.5). Thus scattering by weak surface currents results mainly in directional diffusion of surface gravity waves.

3.3 Diffusion of wave action density by isotropic velocity fields

The derivation of (3.7) makes essential use of the assumption that the spatial statistics of $\boldsymbol{U}$ are spatially homogeneous. We now make the further assumption that the statistical properties of $\boldsymbol{U}$ are also isotropic and investigate the contributions of vertical vorticity and horizontal divergence to D_{jn}. We follow Bühler et al. (2014a) and represent $\boldsymbol{U}$ with a 2D Helmholtz decomposition into rotational (solenoidal) and irrotational (potential) components

$$\boldsymbol{U} = (U, V) = (\phi_x - \psi_y, \phi_y + \psi_x)\,. \tag{3.9}$$

The streamfunction ψ and velocity potential ϕ have the two-point correlation functions

$$C^{\psi}(r) = \langle \psi(\boldsymbol{x})\psi(\boldsymbol{x}')\rangle\ , \qquad \text{and} \qquad C^{\phi}(r) = \langle \phi(\boldsymbol{x})\phi(\boldsymbol{x}')\rangle\ . \tag{3.10}$$

If the velocity ensemble is not mirror invariant under reflexion with respect to an axis in the (x, y)-plane, then there might also be a "cross-correlation" between ψ and ϕ

$$C^{\psi\phi}(r) \stackrel{\text{def}}{=} \langle \psi(\boldsymbol{x})\phi(\boldsymbol{x}')\rangle = \langle \psi(\boldsymbol{x}')\phi(\boldsymbol{x})\rangle\ . \tag{3.11}$$

Because of isotropy, the scalar correlation functions introduced in (3.10) and (3.11) depend only on the distance $r = |\boldsymbol{r}|$ between points $\boldsymbol{x}$ and $\boldsymbol{x}'$. Therefore, $\partial_{r_i} = \partial_{x_i} = -\partial_{x'_i}$. Using the notation $\boldsymbol{r} = (r_1, r_2)$, the V_{11} component of the velocity autocorrelation tensor in (3.6)

can be expressed in terms of the scalar correlation functions as

$$\mathsf{V}_{11}(\boldsymbol{r}) = \langle U(\boldsymbol{x})U(\boldsymbol{x}')\rangle \,, \tag{3.12}$$

$$= \langle \psi_y \psi_{y'}\rangle - \langle \psi_{y'}\phi_x\rangle - \langle \psi_y \phi_{x'}\rangle + \langle \phi_x \phi_{x'}\rangle \,, \tag{3.13}$$

$$= -\partial_{r_2}^2 C^{\psi} + 2\partial_{r_1}\partial_{r_2} C^{\psi\phi} - \partial_{r_1}^2 C^{\phi} \,. \tag{3.14}$$

Similar calculations for the other components of V_{im} result in

$$\mathsf{V}_{im} = \mathsf{V}_{im}^{\psi} + \mathsf{V}_{im}^{\psi\phi} + \mathsf{V}_{im}^{\phi} \,, \tag{3.15}$$

with

$$\mathsf{V}_{im}^{\psi} = \begin{bmatrix} -\partial_{r_2}^2 & \partial_{r_1}\partial_{r_2} \\ \partial_{r_1}\partial_{r_2} & -\partial_{r_1}^2 \end{bmatrix} C^{\psi} \,, \qquad \mathsf{V}_{im}^{\phi} = -\begin{bmatrix} \partial_{r_1}^2 & \partial_{r_1}\partial_{r_2} \\ \partial_{r_1}\partial_{r_2} & \partial_{r_2}^2 \end{bmatrix} C^{\phi} \,, \tag{3.16}$$

$$\text{and} \qquad \mathsf{V}_{im}^{\psi\phi} = \begin{bmatrix} 2\partial_{r_1}\partial_{r_2} & \partial_{r_2}^2 - \partial_{r_1}^2 \\ \partial_{r_2}^2 - \partial_{r_1}^2 & 2\partial_{r_1}\partial_{r_2} \end{bmatrix} C^{\psi\phi} \,. \tag{3.17}$$

The Fourier transform of (3.16) and (3.17) follows with $\partial_{r_i} \mapsto \mathrm{i}q_i$ and is equal to

$$\tilde{\mathsf{V}}_{im}^{\psi}(\boldsymbol{q}) = \left(q^2\delta_{im} - q_i q_m\right)\tilde{C}^{\psi}(q) \,, \qquad \tilde{\mathsf{V}}_{im}^{\phi}(\boldsymbol{r}) = q_i q_m \tilde{C}^{\phi}(q) \,, \tag{3.18}$$

$$\text{and} \qquad \tilde{\mathsf{V}}_{im}^{\psi\phi}(\boldsymbol{q}) = \left(q_i q_m^{\perp} + q_i^{\perp} q_m\right)\tilde{C}^{\psi\phi}(q) \,, \tag{3.19}$$

where $\boldsymbol{q}^{\perp} = (-q_2, q_1)$ is the perpendicular vector to $\boldsymbol{q} = (q_1, q_2)$. Also in (3.18) and (3.19)

$$\tilde{C}^{\psi}(q) = 2\pi \int_0^{\infty} C^{\psi}(r) J_0(qr)\, r\mathrm{d}r \,, \tag{3.20}$$

with J_0 the Bessel function of order zero, is the Fourier transform of the axisymmetric function $C^{\psi}(r)$. The expressions for $\tilde{C}^{\phi}(q)$ and $\tilde{C}^{\psi\phi}(q)$ are analogous to (3.20).

Substituting (3.18) and (3.19) into (3.7) we have

$$k_i k_m \tilde{\mathsf{V}}_{im}(\boldsymbol{q}) = k^2 q^2 \tilde{C}^{\psi}(q) + \cdots \tag{3.21}$$

where $\cdots$ above indicates the three other terms that arise from contracting (3.18) and (3.19) with $k_i k_m$. Each of these three terms, however, contains a factor $\boldsymbol{kq}$. Courtesy of $\delta(\boldsymbol{kq})$ in the integrand of (3.7), the $\cdots$ in (3.21) makes no contribution to D_{jn} and the diffusivity tensor reduces to

$$\mathsf{D}_{jn}(\boldsymbol{k}) = \frac{k^3}{4\pi c} \int q^2 q_j q_n \tilde{C}^{\psi}(q) \delta\big(\boldsymbol{qk}\big) \mathrm{d}\boldsymbol{q}\,, \tag{3.22}$$

where the integral covers the entire (q_1, q_2)-plane. The diffusion tensor in (3.22) does not depend on the velocity potential ϕ. Using $\delta(\boldsymbol{qk})$ to evaluate one of the two integrals in (3.22) one obtains

$$\mathsf{D}_{jn}(\boldsymbol{k}) = \frac{1}{2\pi c} \begin{bmatrix} k_2^2 & -k_1 k_2 \\ -k_1 k_2 & k_1^2 \end{bmatrix} \int_0^{\infty} q^4 \tilde{C}^{\psi}(q)\ \mathrm{d}q\,. \tag{3.23}$$

It is remarkable that the compressible and irrotational component of the velocity field, produced by the velocity potential ϕ, makes no contribution to the action diffusion tensor in (3.23). Dysthe (2001a) shows that in the weak-current limit, $\epsilon \ll 1$, the ray curvature is equal to ζ/c where $\zeta = \psi_{xx} + \psi_{yy}$ is the vertical vorticity of the surface currents; see section 68 of Landau and Lifshitz (1987a) and Gallet and Young (2014) for alternative derivations. These ray-tracing results rationalize the result in (3.23) that diffusion of surface-wave action by sea-surface currents is produced only by the vortical and horizontally incompressible component of the sea-surface velocity.

This effect is illustrated in figure 3.1, where we show ray trajectories obtained by numerical integration of the ray equations (3.3) for waves with period of 10s propagating through three

different types of surface flows (purely solenoidal, purely potential, and combined solenoidal and potential). These synthetic surface currents were created from a scalar function with random phase and prescribed spectral slope ($q^{-2.5}$ in this case). In panel A this function is used as a streamfunction ψ to generate an incompressible vortical flow. In panel B the same function is used as a velocity potential ϕ to generate an irrotational horizontally divergent flow. In panels B and E, with pure potential flow, the ray trajectories are close to straight lines i.e., there is almost no scattering. The flow in panel C is constructed by summing the velocity fields in A and B. Even though the flow in C is twice as energetic as that in A, the ray trajectories in D and F are very similar. This is a striking confirmation of (3.22): the diffusivity is not affected by ϕ. Because $\mathsf{D}_{jn}k_n = 0$, the diffusive flux of wave action, $-\mathsf{D}_{jn}\partial_{k_n}\bar{A}$, is in the direction of $\boldsymbol{k}^{\perp} = k\hat{\boldsymbol{\theta}}$ where (k, θ) are polar coordinates in the $\boldsymbol{k}$-plane and $\hat{\boldsymbol{\theta}}$ is a unit vector in the θ-direction. Using these polar coordinates simplifies the ∂_{k_j} and ∂_{k_n} derivatives on the right of (3.5) so that the averaged action equation becomes

$$\bar{A}_t + c\cos\theta\bar{A}_x + c\sin\theta\bar{A}_y = \alpha\bar{A}_{\theta\theta}\,, \tag{3.24}$$

where

$$\alpha(k) = \frac{1}{2\pi c}\int_0^\infty q^4\tilde{C}^{\psi}(q)\;\mathrm{d}q \tag{3.25}$$

is the directional diffusivity.

To conclude this section we express α in (3.25) in terms of the energy spectrum of the solenoidal component of the velocity $\tilde{E}^{\psi}(q)$, related to $\tilde{C}^{\psi}(q)$ by

$$\tilde{E}^{\psi}(q) = \frac{q^3}{4\pi}\tilde{C}^{\psi}(q)\,. \tag{3.26}$$

The spectrum is normalized so that the root-mean-square velocity of the solenoidal component, $\mathcal{U}_{\psi}$, is

$$\mathcal{U}_{\psi}^2 = \langle\psi_x^2\rangle = \langle\psi_y^2\rangle = \tfrac{1}{2}\langle|\boldsymbol{\nabla}\psi|^2\rangle = \int_0^\infty \tilde{E}^{\psi}(q)\,\mathrm{d}q\,. \tag{3.27}$$

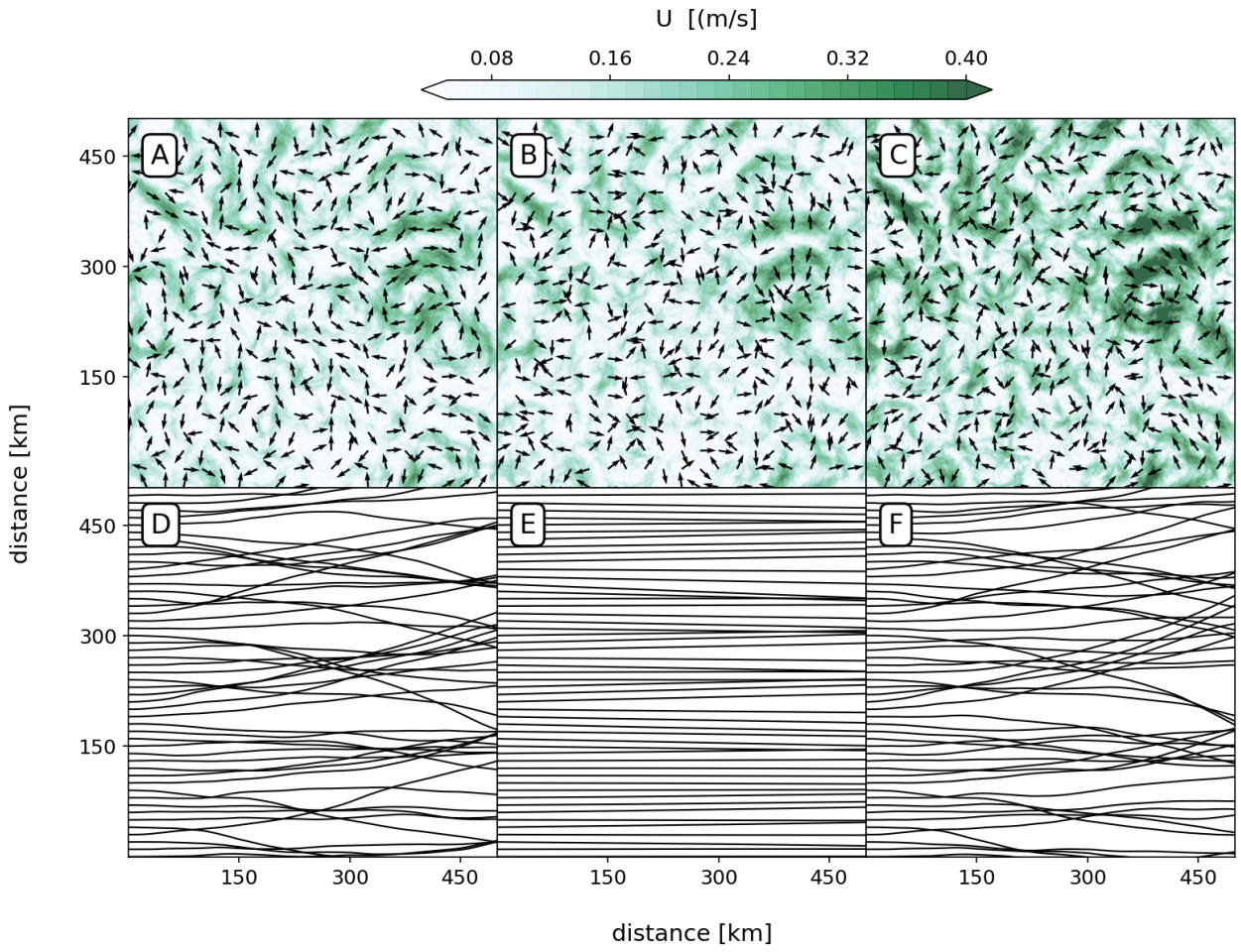

Figure 3.1: Illustration of the effects of different surface flow regimes on the diffusion of surface waves. Surface flow fields are shown on the top row and the respective ray trajectories in the bottom row. Panels A and D show solenoidal flow; panels B and E potential flow. Panels C and F show a combination of solenoidal and potential flows (the velocity in panel C is the sum of the velocities in panels A and B). The mean kinetic energy of A and B are equal, whereas panel C has twice that of A and B. All rays are initialized from the left side of the domain at $x = 0$ with direction $\theta = 0°$ and period equal to 10s.

Then $\alpha(k)$ can be written as

$$\alpha(k) = \frac{2}{c}\int_0^\infty q\tilde{E}^\psi(q)\,\mathrm{d}q\,. \tag{3.28}$$

Taking the trace of the velocity correlation tensors in (3.18) and (3.19) shows that the total energy spectrum is

$$\tilde{E} = \tilde{E}^\psi(q) + \tilde{E}^\phi(q), \tag{3.29}$$

where $\tilde{E}^\phi(q)$ is obtained by $\psi \mapsto \phi$ in (3.27). As anticipated in figure 3.1, the diffusivity $\alpha(k)$ in (3.28) depends only on the spectrum of the solenoidal component, $\tilde{E}^\psi(q)$.

Smit and Janssen (2019) arrive at an expression for $\alpha(k)$ differing from (3.28) in two respects: *(i)* the coefficient in front of the integral on the right is $(1/c)$; and *(ii)* the integrand is $\tilde{E}(q)$. This expression agrees with (3.28) only for the special class of isotropic velocity fields considered by Smit & Janssen in which the integral of $\tilde{E}^\phi(q)$ is equal to the integral of $\tilde{E}^\psi(q)$ i.e., isotropic flows in which kinetic energy is equipartitioned between the solenoidal, ψ, and the potential, ϕ, components. An example of an equipartitioned flow is shown in the third column of figure 3.1 and discussed further in section 3.4 (see the + simulations). Equipartition, however, is not characteristic of ocean macroturbulence e.g., large scales are in geostrophic balance and are therefore solenoidal. In this pure solenoidal case the diffusivity in Smit and Janssen (2019) would be too small by a factor of two.

3.4 A numerical example using ray tracing

Equation (3.24) has an exact solution that can be used to test (3.28). Begin by noting that

$$\frac{\mathrm{d}}{\mathrm{d}t}\iiint A\,\mathrm{d}x\mathrm{d}y\mathrm{d}\theta = 0\,, \tag{3.30}$$

where the integrals above are over the whole (x, y)-plane and over $-\pi < \theta \leq \pi$. This is, of course, conservation of action. Multiplying (3.24) by $\cos\theta$ and integrating over (x, y, θ) one

obtains

$$\frac{\mathrm{d}}{\mathrm{d}t}\iiint \cos\theta\, A\,\mathrm{d}x\mathrm{d}y\mathrm{d}\theta = -\alpha \iiint \cos\theta\, A\,\mathrm{d}x\mathrm{d}y\mathrm{d}\theta\,. \tag{3.31}$$

Combining the time integrals of (3.30) and (3.31) we find

$$\langle\cos\theta\rangle = \langle\cos\theta\rangle_0\,\mathrm{e}^{-\alpha t}\,, \tag{3.32}$$

where $\langle\rangle$ denotes the action-weighted average and $\langle\cos\theta\rangle_0$ is the initial value of $\langle\cos\theta\rangle$. At large times $\langle\cos\theta\rangle \to 0$ with an e-folding time α^{-1}: this is long-time isotropization of the wave field by eddy scattering. To investigate short-time and small-angle scattering, consider for simplicity an initial condition such as that in figure 3.1 with initial direction $\theta_0 = 0$. Then with $\alpha t \ll 1$ and $\theta \ll 1$, it follows from (3.32) that $\langle\theta^2\rangle \approx 2\alpha t$.

To test our result for the diffusivity α, we verify $\langle\theta^2\rangle \approx 2\alpha t$ by numerical integration of the ray-tracing equations (3.3) for surfaces waves with initial period of 10s propagating through an ensemble of stochastic velocity fields. The ensemble is created by assigning random phases to each Fourier component of the stream function ψ and velocity potential ϕ. The energy spectrum of the sea surface velocity is modelled with power laws $\tilde{E}^{\psi}(q)$ and $\tilde{E}^{\phi}(q) \propto q^{-n}$, with $q_1 < q < q_2$ and no energy outside the interval (q_1, q_2). The spectra are normalized with prescribed mean square velocities $\mathcal{U}^2_{\psi}$ and $\mathcal{U}^2_{\phi}$ as in (3.27). For $n \neq (1, 2)$ the integral in (3.28) is evaluated as:

$$\alpha = \frac{2}{c}\frac{(n-1)}{(n-2)}\,\frac{(q_1^{2-n} - q_2^{2-n})}{(q_1^{1-n} - q_2^{1-n})}\,\mathcal{U}^2_{\psi}\,. \tag{3.33}$$

For $n = 1$

$$\alpha = \frac{2}{c}\frac{(q_2 - q_1)}{\ln(q_2/q_1)}\mathcal{U}^2_{\psi}\,, \tag{3.34}$$

and for $n = 2$

$$\alpha = \frac{2}{c}\frac{q_1 q_2}{q_2 - q_1}\,\ln(q_2/q_1)\;\mathcal{U}^2_{\psi}\,. \tag{3.35}$$

We take $q_1 = 2\pi/150$km and $q_2 = 2\pi/1$km and spectral slopes $n = (5/3, 2.0, 2.5, 3.0)$. For

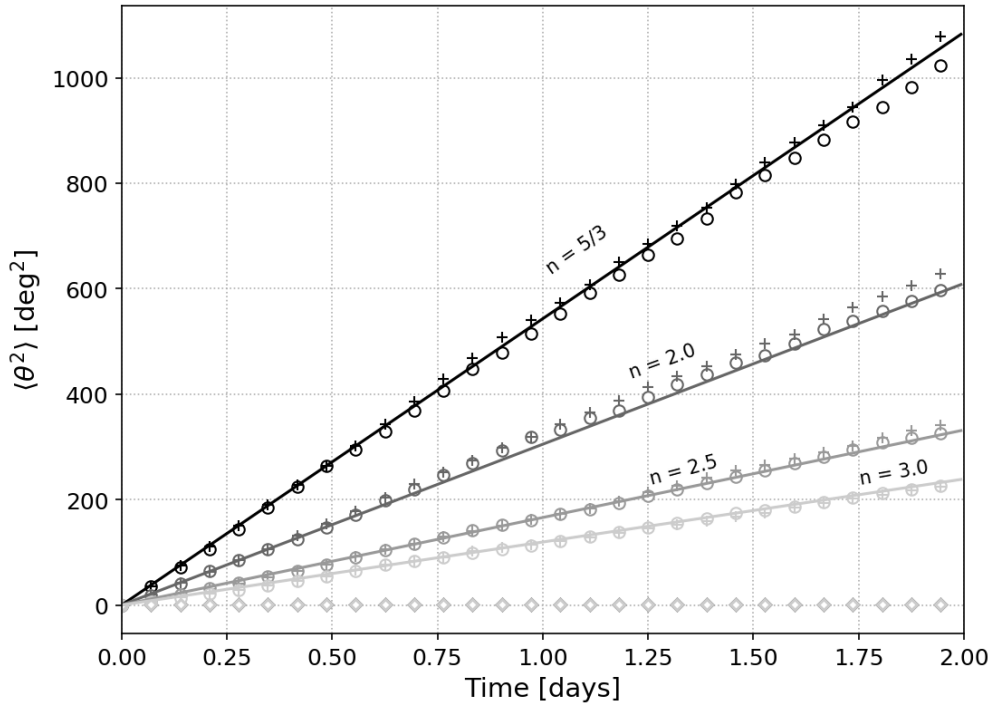

Figure 3.2: Comparison between the Monte Carlo ray-tracing simulations averaged across an ensemble of stochastic velocity fields (markers) and the analytical result $\langle\theta^2\rangle \approx 2\alpha t$ (solid lines). Here we show the results for an energy spectrum with spectral slopes following a q^{-n} power-law where $n = 5/3$, 2, 2.5, or 3. Circles $\circ$ are the result for solenoidal flows; diamonds $\diamond$, for potential flows; and crosses $+$ for the combination of solenoidal and potential. The solenoidal and potential flows have mean square velocity 0.01 m^2/s^2, whereas the combined flow $+$ has mean square velocity 0.02 m^2/s^2. The initial period and direction of the waves are 10s and 0°, respectively.

each n we consider three cases corresponding to the three columns in figure 3.1:

$\circ$ $\mathcal{U}_\psi = 0.1\text{m s}^{-1}$ and $\mathcal{U}_\phi = 0$;

$\diamond$ $\mathcal{U}_\psi = 0$ and $\mathcal{U}_\phi = 0.1\text{m s}^{-1}$;

$+$ $\mathcal{U}_\psi = 0.1\text{m s}^{-1}$ and $\mathcal{U}_\phi = 0.1\text{m s}^{-1}$.

Figure 3.2 summarizes the results by showing $\langle\theta^2\rangle$ as a function of time obtained by averaging 2000 rays. The results are in agreement with $\langle\theta^2\rangle \approx 2\alpha t$ using α obtained from (3.33) and (3.35). In particular there is good agreement between $\langle\theta^2\rangle$ for case $\circ$ and the analytic result (solid lines). As expected, the potential component of the velocity has no effect on the diffusion of wave action. Thus in case $\diamond$ — pure potential flow — there is no diffusion of action. In case $+$ the flow has twice as much kinetic energy (and shear) as in cases $\circ$ and $\diamond$; this is also an example of a flow with kinetic energy equipartitioned between the solenoidal and potential components (Smit and Janssen, 2019). Doubling the strength of the flow, by adding a ϕ component, does not significantly increase action diffusion above that of case $\circ$.

At the final time, two days, the $n = 5/3$ simulations shown in figure 3.2 have $\sqrt{\langle\theta^2\rangle}$ of order 30° and the other, steeper, spectral slopes result in smaller directional spreading. Thus none of the Monte Carlo simulations shown in figure 3.2 have lasted long enough to result in isotropization of the wave field. We verified, however, that longer simulations are in agreement with (3.32) when $\alpha t \sim 1$ (not shown).

We conclude this section by noting that numerical and observational evidence supports the hypothesis that $\tilde{E}(q) \sim q^{-2}$ on submesoscales (very roughly, scales less than 50km). Horizontally divergent motions contribute significantly the total surface kinetic energy in this range, but the solenoidal component is not negligible (Rocha et al., 2016b; Torres et al., 2018; Kafiabad et al., 2019; Morrow et al., 2019). There is considerable geographic variation. For example, the Gulf Stream region is an exception, with $\tilde{E}(q) \sim q^{-3}$ and little indication of horizontally divergent motions (Bühler et al., 2014a). These results indicate that spectral

slope -2 is relevant to oceanic application of (3.28). But with -2, the integral on the right of (3.28) is sensitive to high-wavenumber solenoidal energy i.e., to the value of the high-wavenumber cut-off q_2, as in (3.35). This problem is worse for spectral slopes shallower than -2, and less severe in the Gulf Stream region with the steeper slope -3.

In the absence of a high-wavenumber transition to a spectral fall-off steeper than -2, the cut-off q_2 might be determined by the failure of the WKB approximation once the horizontal scales of $\boldsymbol{U}$ are comparable to the hundred-meter wavelengths of surface gravity waves. These considerations complicate the practical application of (3.28) in some oceanic regimes and indicate the necessity of better understanding the interaction of surface gravity waves with wave-scale currents.

3.5 Conclusions

Our expression for the action diffusivity in (3.7) assumes that the WKB approximation is valid and that $\epsilon = |\boldsymbol{U}|/c \ll 1$. Typical sea-surface currents are of order 0.1m s^{-1} while the swell band has group velocities that exceed 5m s^{-1}. Thus $\epsilon \ll 1$ is not restrictive. Our analysis also neglects effects associated with vertical shear of the flow, which would modify the Doppler-shifted dispersion relationship (Kirby and Chen, 1989).

We derived an expression for the diffusivity of surface wave action in (3.7) and demonstrated that for isotropic surface currents the action diffusivity can be expressed in terms of the kinetic energy spectrum of the flow as in (3.28). This result shows that the potential component makes no contribution to action diffusion. Our results are illustrated both qualitatively (figure 3.1) and quantitatively (figure 3.2) by numerical solution of the ray equations. Although the numerical examples presented here were obtained for synthetic flows having random phase, the results are also valid in the presence of coherent structures, such as axisymmetric vortices, as long as the statistics remain isotropic (not shown). To leading order, there is no difference between the diffusivity obtained for rays propagating through a pure

solenoidal flow and the same solenoidal flow with the addition of an equally strong potential component. Provided that $\epsilon \ll 1$, the horizontally divergent and irrotational component of the sea-surface velocity has no effect on the action diffusion of surface gravity waves.

Recent studies motivated by the upcoming Surface Water and Ocean Topography (SWOT) satellite mission have found that surface kinetic energy spectra in the ocean are marked by a transition scale from balanced geostrophic motions (horizontally non-divergent) to unbalanced horizontally divergent motions such as inertia-gravity waves (e.g., Rocha et al., 2016a,b; Torres et al., 2018; Qiu et al., 2018; Morrow et al., 2019). At scales shorter than this "transition" scale, the kinetic energy spectrum of the potential component of the currents has been observed to dominate over the solenoidal component. In this regime, only a small fraction of the total kinetic energy of the flow would be contributing to the diffusion of surface wave action.

Perhaps the most important application of our results is in the realm of operational surface wave models. Wave models, such as WaveWatch III, solve the action balance equation (4.7) with additional terms to account for wind forcing, non-linear interactions, and wave dissipation (WAVEWATCH III Development Group, 2009). Explicitly solving for wave-current interactions in surface-wave models poses two main challenges: it is computationally costly and surface current observations at scales shorter than 100 km are rare (Ardhuin et al., 2012). The wave action diffusivity calculated here can be easily implemented as an additional term in operational wave models allowing the effects of the currents to be accounted for based on statistical properties of the sea-surface velocity. Although not discussed in the present manuscript, it is also worth noting that refraction of surface waves by meso and submesoscale flows will ultimately lead to deviations of the wave propagation from the great-circle route, impacting path lengths and, subsequently, arrival times (Smit and Janssen, 2019). An statistical approach to account for these effects in numerical wave models could potentially improve arrival time predictions.

Declaration of Interests. The authors report no conflict of interest.

Appendix

3A The induced diffusion approximation

In this appendix we reprise the KSV multiscale derivation of the induced diffusion approximation showing that the KSV assumption that $\boldsymbol{U}$ is incompressible is not necessary. All that is required is spatial homogeneity of the statistical properties of the sea-surface velocity $\boldsymbol{U}$.

We follow KSV and introduce the small parameter ϵ defined in (3.1) into the conservation equation of wave action (4.7) by writing $U_m \mapsto \epsilon U_m$. With slow space and time scales $\boldsymbol{X} = \epsilon^2 \boldsymbol{x}$ and $T = \epsilon^2 t$, the action equation (4.7) becomes

$$\partial_t A + c_n \partial_{x_n} A + \epsilon^2 \partial_T A + \epsilon^2 c_n \partial_{X_n} A + \epsilon U_n \partial_{x_n} A + \epsilon^3 U_n \partial_{X_n} A - \epsilon k_m U_{m,n} \partial_{k_n} A = 0 \,. \tag{3.36}$$

With the expansion $A = A_0(\boldsymbol{X}, \boldsymbol{k}, T) + \epsilon A_1(\boldsymbol{x}, \boldsymbol{X}, \boldsymbol{k}, t, T) + \cdots$ we satisfy the leading-order equation. Then at order ϵ^1:

$$\partial_t A_1 + c_n \partial_{x_n} A_1 = k_m U_{m,n} \, \partial_{k_n} A_0 \,, \tag{3.37}$$

with solution

$$A_1 = k_m \int_0^t U_{m,n}(\boldsymbol{x} - \tau \boldsymbol{c}) \, \mathrm{d}\tau \, \partial_{k_n} A_0 \,. \tag{3.38}$$

At order ϵ^2 the problem is

$$\partial_t A_2 + c_n \partial_{x_n} A_2 + \partial_T A_0 + c_n \partial_{X_n} A_0 = k_i U_{i,j}(\boldsymbol{x}) \partial_{k_j} A_1 - U_i(\boldsymbol{x}) \partial_{x_i} A_1 \,. \tag{3.39}$$

Pulling out ∂_{k_j} from the first term on the right of (3.39) and recombining we obtain

$$\partial_t A_2 + c_n \partial_{x_n} A_2 + \partial_T A_0 + c_n \partial_{X_n} A_0 = \partial_{k_j} k_i U_{i,j}(\boldsymbol{x}) A_1 - \partial_{x_i}(U_i(\boldsymbol{x}) A_1)\,. \tag{3.40}$$

None of these manipulations require $U_{i,i} = 0$. Assuming spatial homogeneity and taking the average over an ensemble of velocity fields, here denoted by an overbar, the last term on the right of (3.40) is the fast-x derivative of an average, which is zero because of spatial homogeneity. In the limit of $t \to \infty$, and using the expression for A_1 in (3.38), we find

$$\partial_T \bar{A} + c_n \partial_{X_n} \bar{A} = \partial_{k_j} \mathsf{D}_{jn} \partial_{k_n} \bar{A}\,, \tag{3.41}$$

where $\bar{A}$ is the ensemble average of A_0 and

$$\mathsf{D}_{jn}(\boldsymbol{k}) = k_i k_m \int_0^\infty \langle U_{i,j}(\boldsymbol{x}) U_{m,n}(\boldsymbol{x} - \tau \boldsymbol{c}) \rangle \, \mathrm{d}\tau\,. \tag{3.42}$$

We now write $U_i(\boldsymbol{x})$ and $U_m(\boldsymbol{x} - c\boldsymbol{\tau})$ in terms of inverse Fourier transforms, such as

$$U_i(\boldsymbol{x}) = \int \mathrm{e}^{\mathrm{i}\boldsymbol{q}\boldsymbol{x}} \tilde{U}_i(\boldsymbol{q}) \, \frac{\mathrm{d}\boldsymbol{q}}{(2\pi)^2}\,. \tag{3.43}$$

Substituting these Fourier representations into (3.42), and using the identity

$$\left\langle \tilde{U}_i(\boldsymbol{q}) \tilde{U}_m(\boldsymbol{q}') \right\rangle = (2\pi)^2 \delta\big(\boldsymbol{q} + \boldsymbol{q}'\big) \tilde{\mathsf{V}}_{im}(\boldsymbol{q})\,, \tag{3.44}$$

we obtain

$$\langle U_{i,j}(\boldsymbol{x}) U_{m,n}(\boldsymbol{x} - \tau \boldsymbol{c}) \rangle = \int \mathrm{e}^{\mathrm{i}\boldsymbol{q}\tau\boldsymbol{c}} \, q_j q_n \tilde{\mathsf{V}}_{im}(\boldsymbol{q}) \, \frac{\mathrm{d}\boldsymbol{q}}{(2\pi)^2}\,, \tag{3.45}$$

where $\tilde{\mathsf{V}}_{im}(\boldsymbol{q})$ is the Fourier transform of $\mathsf{V}_{im}(\boldsymbol{r})$, as in (3.8). Substituting (3.45) into (3.42),

switching the order of the integrals and using

$$\int_0^\infty \mathrm{e}^{\mathrm{i}\boldsymbol{q}\tau\boldsymbol{c}}\,\mathrm{d}\tau = \pi\delta(\boldsymbol{q}\boldsymbol{c}) = \pi k\delta(\boldsymbol{q}\boldsymbol{k})/c\,, \tag{3.46}$$

we obtain D_{jn} in (3.7). In (3.46) we have parted company with KSV by taking advantage of the isotropic dispersion relation of surface gravity waves — that is $\boldsymbol{c} = c\boldsymbol{k}/k$ — to simplify $\delta(\boldsymbol{q}\boldsymbol{c})$.

Acknowledgements

The authors thank the two anonymous reviewers for their suggestions in improving this manuscript. The authors are also thankful to Bruce D. Cornuelle, Sarah T. Gille, Matthew R. Mazloff, Pieter B. Smit and Jacques Vanneste for helpful discussion and suggestions and Guilherme Castelão for helping with the optimization of the ray-tracing solver. ABVB was funded by NASA Earth and Space Science Fellowship award number 80NSSC17K0326 and by NASA award NNX16AH67G. WRY is supported by the National Science Foundation Award OCE-1657041.

Chapter 3, in full, reprints material as it appears in Journal of Fluid Mechanics, 2020, DOI:10.1017/jfm. Ana B Villas Bôas and William R. Young. The dissertation author was the primary investigator and author of this paper.

Chapter 4

Wave-Current Interactions at Meso and Submesoscales: Insights from Idealized Numerical Simulations

Surface waves are part of the physical boundary that separates the ocean from the atmosphere, mediating exchanges of momentum, heat, energy, gases, and other tracers between these two media (Cavaleri et al., 2012; Villas Bôas et al., 2019). Waves are modulated by ocean currents via wave–current interactions, which lead to variations in their direction, frequency, and amplitude (Phillips, 1966; Peregrine, 1976). The effects of ocean currents on surface waves have been observed across upwelling jets off the California coast and meanders in the Loop Current region (Romero et al., 2017; Romero, 2019). These modulations resulted in high spatial inhomogeneity of the wave field, enhancing nonlinear effects such as wave breaking and producing variations of up to 30% in the significant wave height (H_s, the average of the highest one-third of the wave heights). Moreover, recent case studies based on realistic numerical simulations in the Gulf Stream and the Drake Passage suggest that surface currents dominate the variability of H_s at scales between 10 km and 100 km (Ardhuin et al., 2017). Although there is growing observational evidence based on satellite measurements to

support this hypothesis (e.g. Quilfen et al., 2018; Quilfen and Chapron, 2019), our knowledge of how meso and submesoscale currents affect the surface wave field is still limited by the lack of simultaneous measurements of waves and currents at these scales.

The surface kinetic energy (KE) of the ocean at mesoscales is known to be dominated by non-divergent, geostrophically balanced motions; however, in the submesoscale range, divergent motions associated with fronts, tides, and inertia-gravity waves account for a large portion of the KE (Bühler et al., 2014b; Rocha et al., 2016a; McWilliams, 2016). Several studies motivated by the upcoming Surface Water and Ocean Topography (SWOT) satellite altimetry mission have found strong seasonality in the KE in many regions of the ocean (e.g., Qiu et al., 2018, 2017; Rocha et al., 2016b). In the California Current System (CCS) region, for example, the KE is mostly dominated by balanced (rotational) motions in late winter/spring, while divergence is stronger in late summer/fall (Chereskin et al., 2019). Recent theoretical work by Villas Bôas and Young (2020) show from a ray-tracing framework that surface waves respond remarkably differently to divergent and rotational flows. Thus, a seasonality in the underlying kinematics governing surface currents should result in significant changes in the surface wave field.

Ardhuin et al. (2017) found strong gradients in wave heights associated with the flow intensity and structure. In that study, the authors used realistic currents, waves, and wind forcing to investigate relationships between currents and waves. More recently, Romero et al. (2020) investigated the effects of currents on waves using very high-resolution O(100 m) currents from a setup of the ocean model ROMS in southern California to force WW3. Although their results suggest wave refraction to be the main cause of H_s gradients, the underlying mechanisms leading to that are difficult to isolate due to the complexity of their model, which encompasses interactions between currents, winds, waves and other sources and sinks of wave action. In this context, idealized simulations provide a useful tool to diagnose the mechanisms leading to gradients in the wave field and to shed light on the extent to which surface wave gradients could be used to infer kinematic properties of the flow.

Building on Ardhuin et al. (2017) and the theoretical framework from Villas Bôas and Young (2020), here we analyze a large ensemble of numerical experiments produced using an idealized setup of the WAVE-height, WATer depth and Current Hindcasting (WAVEWATCH III) third generation wave model (hereinafter WW3) forced by synthetic currents to assess how the wave field responds to rotational and divergent flows. In addition, the response behavior diagnosed with the synthetic currents is used to interpret the results of simulations using realistic currents from a high-resolution ocean model in the CCS region. In section **??**, we present a theoretical background on current effects on waves. Section 4.2 describes the methods and the wave model setup. Results are presented and discussed in section **??**. Finally, a summary of the main results and conclusions of this paper is presented in section **??**.

4.1 Background

ch4background In this section we provide some theoretical background on the effects of currents on waves. We focus on linear deep-water surface gravity waves and, for the purpose of this paper, we consider horizontal currents that are depth-independent i.e., there is no vertical shear. Here, we are only concerned about the effects of currents on waves and not the effects of waves on currents. For a recent description of the two-way coupled problem see, for example, McWilliams (2018) and Suzuki (2019).

Waves propagating over a current are subject to a Doppler shift of their frequency, which can be expressed as

$$\omega(t, \boldsymbol{x}, \boldsymbol{k}) = \sigma + \boldsymbol{k}\boldsymbol{U}(t, \boldsymbol{x}) \,, \tag{4.1}$$

where ω is the absolute frequency (as observed from a fixed reference frame), σ is the intrinsic frequency (as observed from a reference frame moving with the current), $\boldsymbol{k} = (k_1, k_2)$ is the wavenumber vector, and $\boldsymbol{U}(t, \boldsymbol{x}) = (u, v)$ is the horizontal surface current. The intrinsic frequency is related to the wavenumber via the dispersion relationship. The cases studied

here use the dispersion relationship for deep-water linear surface waves:

$$\sigma = (gk)^{1/2}, \tag{4.2}$$

where g is the gravitational acceleration and $k = |\boldsymbol{k}|$. Here, the effects of surface currents on waves will be explored in the light of ray theory for linear waves, which assumes the geometrical optics approximation. For doing so, the underlying assumption is that currents are slowly varying with respect to the waves, i.e., the temporal scales of variations in the current field are longer and the spatial scales are larger than those of the waves. Formally, one can express these assumptions as (e.g., Peregrine, 1976):

$$k \gg \max\left|\frac{1}{U}\frac{\partial U}{\partial L_U}\right| \quad \text{and} \quad \omega \gg \max\left|\frac{1}{U}\frac{\partial U}{\partial T_U}\right|, \tag{4.3}$$

where U is the characteristic current speed, and L_U and T_U and are the characteristic spatial and temporal scales of the current. In addition, the group speed of the waves $c = (1/2)(g/k)^{1/2}$ is assumed to be much larger than the current speed U, such that:

$$\varepsilon \stackrel{\text{def}}{=} \frac{U}{c} \ll 1. \tag{4.4}$$

Using index notation, in which subscripts after the comma indicate partial derivatives, the evolution of the absolute frequency, wavenumber, and trajectory following a wave train are then given by the ray equations:

$$\dot{\omega} = k_n \partial_t U_n, \tag{4.5a}$$

$$\dot{k}_n = -\partial_{x_n}\omega = -U_{m,n}k_m\,, \tag{4.5b}$$

$$\dot{x}_n = \partial_{k_n}\omega = c_n + U_n\,, \tag{4.5c}$$

where $c_n = \partial_{k_n}\sigma(k)$ is the group velocity, and the overdot represents the total time derivative

following the wave train:

$$\partial_t + (U_n + c_n)\partial_{x_n}. \tag{4.6}$$

The sea state is composed of waves of multiple frequencies and directions, such that a convenient way of describing it is through the wave energy density spectrum $E(t, \boldsymbol{x}, \boldsymbol{k})$. However, under the influence of an inhomogeneous current, the wave energy is not conserved, due to the exchange of energy between the currents and the wave field via radiation stresses (Longuet-Higgins and Stewart, 1961, 1962). Instead, the wave action A, here approximated as $A(t, \boldsymbol{x}, \boldsymbol{k}) = E(t, \boldsymbol{x}, \boldsymbol{k})/\sigma$, is conserved (Bretherton and Garrett, 1968; Phillips, 1966). Then, the dynamical aspects of the evolution of the wave field can be described by the conservation of wave action:

$$\partial_t A + \dot{x}_n \partial_{x_n} A + \dot{k}_n \partial_{k_n} A = S\,, \tag{4.7}$$

where $\dot{x}_n$ and $\dot{k}_n$ given by 4.5c and 4.5b, and S represents sources and sinks of wave action such as wave breaking, nonlinear interactions, and wind forcing.

In the context of numerical wave modeling, the wavenumber vector is often decomposed into magnitude k and direction θ, such that $A(t, \boldsymbol{x}, \boldsymbol{k}) \equiv A(t, \boldsymbol{x}, k, \theta)$, and (4.7) can be written as

$$\partial_t A + (\boldsymbol{U} + \boldsymbol{c})\boldsymbol{\nabla} A + \dot{k}\partial_k A + \dot{\theta}\partial_\theta A = S\,, \tag{4.8}$$

where $\boldsymbol{\nabla}$ is the horizontal gradient operator. In (4.8), the first term on the left-hand side represents local changes of wave action; the second term is the advection of wave action in physical space (x, y) by the Doppler-shifted group velocity $(\boldsymbol{U} + \boldsymbol{c})$; the last two terms represent the advection of wave action in spectral space (k, θ), where the third term is associated with changes in wavenumber (or frequency), and the fourth term is associated with changes in wave direction (refraction).

4.2 Methods

4.2.1 Current Forcing

Synthetic Current Fields

According to Helmholtz's theorem of vector calculus, any sufficiently smooth two-dimensional velocity field can be decomposed into a component that is purely divergent ($\boldsymbol{U}^{\phi}$, described by a velocity potential ϕ) and a component that is purely rotational ($\boldsymbol{U}^{\psi}$, described by a streamfunction ψ), such that the sum of the two components reconstructs the original velocity completely:

$$\boldsymbol{U} = \boldsymbol{U}^{\phi} + \boldsymbol{U}^{\psi}, \tag{4.9}$$

where,

$$\boldsymbol{U}^{\phi} = (\phi_x, \phi_y)\,, \qquad \text{and} \qquad \boldsymbol{U}^{\psi} = (-\psi_y, \psi_x)\,. \tag{4.10}$$

We generate a set of stochastic horizontal velocity fields as follows. First, a two-dimensional scalar field with prescribed isotropic spectral slope and random phase is created. Then, this field is used as both a velocity potential and as a streamfunction to obtain $\boldsymbol{U}^{\phi}$ and $\boldsymbol{U}^{\psi}$ from (4.10). The resulting divergent and rotational components of the velocity have isotropic kinetic energy spectra $\tilde{E}^{\phi}(q)$ and $\tilde{E}^{\psi}(q)$ that follow a $q^{-\mathbb{S}}$ power law, where $q = |\boldsymbol{q}|$ is the horizontal isotropic wavenumber of the flow and $\mathbb{S}$ is the respective spectral slope. Additionally, the velocities are constructed such that all the variance of the flow is contained in wavelengths between 5 km and 300 km. To represent spectral slopes of surface kinetic energy that are typically observed in the ocean at meso and submesoscales (e.g., Rocha et al., 2016a,b; Qiu et al., 2018), we limit our parameter space to spectral slopes of $\mathbb{S} = (5/3,\ 2,\ 2.5\ , 3)$. Figure 4.1 shows an example of synthetic $\boldsymbol{U}^{\psi}$ (middle column) and $\boldsymbol{U}^{\phi}$ (right column) and the respective kinetic energy spectra for a shallow spectral slope ($q^{-5/3}$, top) and a steep spectral slope (q^{-3}, bottom).

The final velocity used in our simulations is obtained by combining the rotational and

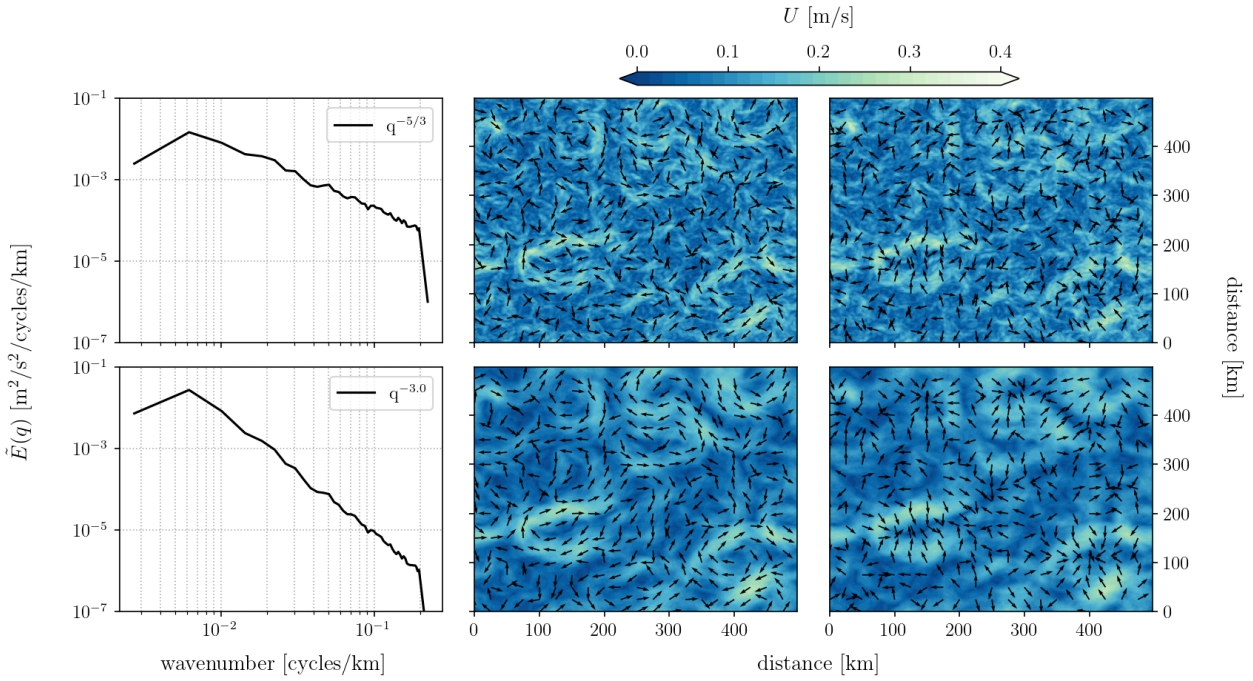

Figure 4.1: Example of stochastic velocity fields with a prescribed spectral slope and random phase. The top row shows the isotropic kinetic energy spectrum for a flow with a $q^{-5/3}$ spectral slope (left) and the corresponding velocity field for a purely rotational flow ($\boldsymbol{U}^{\psi}$, middle) and purely divergent flow ($\boldsymbol{U}^{\phi}$, right). The bottom row is the same, but for a spectral slope of q^{-3}.

divergent components of the flow and normalizing the mean kinetic energy (KE) such that:

$$U_n = \alpha^{1/2} U_n^{\phi} + (1-\alpha)^{1/2} U_n^{\psi}\,, \tag{4.11}$$

and, given the orthogonality of the cross terms,

$$KE = \frac{1}{2}\langle {U_n}^2 \rangle = \alpha \underbrace{\frac{1}{2}\langle (u^{\phi})^2 + (v^{\phi})^2 \rangle}_{KE^{\phi}} + (1-\alpha) \underbrace{\frac{1}{2}\langle (u^{\psi})^2 + (v^{\psi})^2 \rangle}_{KE^{\psi}} \tag{4.12}$$

$$= \alpha KE^{\phi} + (1-\alpha) KE^{\psi}\,, \tag{4.13}$$

where α is a number between zero and one that corresponds to the fraction of the total mean kinetic energy (KE) accounted for by the divergent component of the flow. So, if $\alpha = 1$ the flow is purely divergent, and if $\alpha = 0$ the flow is purely rotational. We ran experiments with

α ranging from 0 to 1 at increments of 0.2. For a particular realization of random phases, the combination of the four different values of $\mathbb{S}$ and six different values of α results in 24 possible velocity fields. For clarity, most of the discussion in the following sections focuses on cases using $\alpha = (0,\ 0.4,\ 0.8,\ 1)$ since we find that these values represent the behavior of the entire range. An example of one realization of a synthetic current field is shown in Figure 4.2.

Realistic Currents from the MITgcm llc4320

To investigate the response of surface waves to realistic mesoscale and submesoscale currents, we used snapshots of surface velocity from the latitude-longitude polar cap numerical simulation llc4320 (Rocha et al., 2016a) which has nominal resolution of 1/48° and was obtained using the Massachusetts Institute of Technology general circulation model (MITgcm). The llc4320 was forced by tides and by 6-hourly surface atmospheric fields. Here, we use surface velocities from the llc4320 in the CCS region (28°N-35°N and 120°W-129°W) from October 2011 to September, 2012 that were interpolated onto a 2.5 km regular Cartesian grid on a 600 km $\times$ 600 km domain. These velocity fields were then sub-sampled every 6 hours and used as an ensemble of snapshots (i.e., no temporal evolution) to force the wave model as described below.

4.2.2 Experimental setup

We use version 5.16 of the wave model WAVEWATCH III (WW3, WAVEWATCH III Development Group, 2016) to integrate the action balance equation. Here, we are only interested in the effects of currents on freely propagating swell-type waves, which are distant from their generation site. Additionally, the waves considered here have small steepness and are far from approaching the breaking limit. With that in mind, we neglect wind forcing, non-linear interactions, and wave breaking, which effectively means that the right-hand side of (4.8) is zero. Throughout this paper we discuss wave quantities that are averaged over

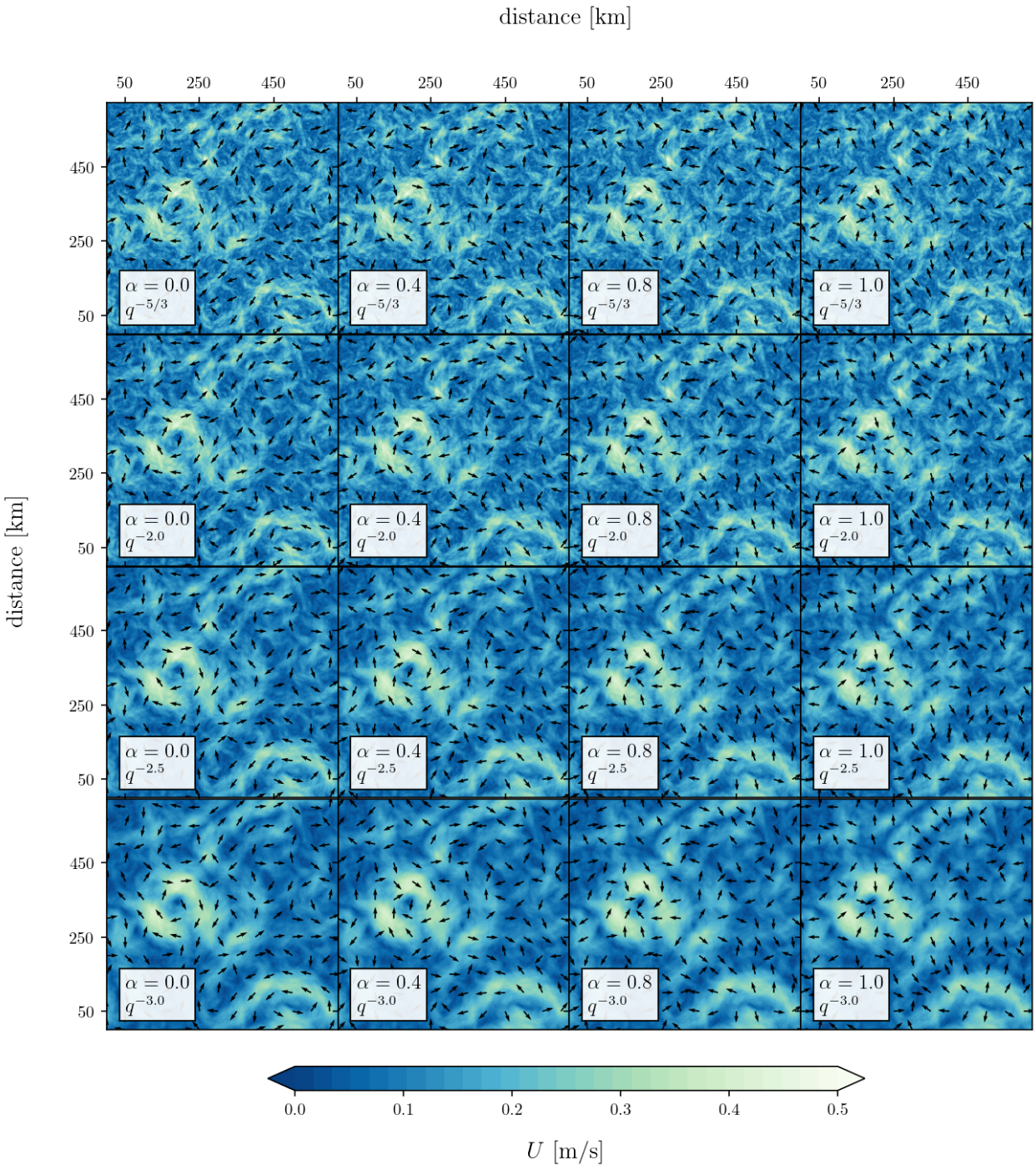

Figure 4.2: One realization of synthetic velocity fields created using the method described in Section 4.2.1. From left to right the velocities go from being purely rotational ($\alpha = 0$) to being purely divergent ($\alpha = 1$). From top to bottom the respective kinetic energy spectral slope goes from $q^{-5/3}$ to q^{-3}. All panels have the same mean kinetic energy and phase.

the wave energy spectrum, which are known as "bulk" quantities. In particular, we focus on the significant wave height (H_s), mean direction (θ_w), mean period ($T_{m0,-1}$), and directional spreading (σ_θ), which are formally defined in the Appendix. All simulations are initialized with a narrow-banded wave spectrum of short-crested waves which is Gaussian in frequency and has a cosine directional distribution. Waves enter the domain from the left boundary with initial mean direction $\theta_w = 270^\circ$ (propagating from left to right), directional spreading $\sigma_\theta = 12.4^\circ$, and $H_s = 1$ m. We run cases with initial mean period $T_{m0,-1} =$ (7 s, 10.3 s, 16.6 s) that are characteristic of swell. Although the quantitative results are affected by the initial value of the directional spreading, the overall discussion remains valid within a range of σ_θ characteristic of swell. Thus, in this manuscript, we chose a fixed value for the initial directional spreading and leave the detailed dependency of the results on σ_θ for future studies.

The experiments are run on a 600 km $\times$ 600 km Cartesian domain with 2.5 km spatial grid resolution, 32 frequencies, and 48 directions. We use a global integration time step of 200 s, spatial advection time step of 50 s, spectral advection time step of 12 s, and minimum source term time step of 5 s (see the appendix for more detail on the model setup). Increasing the spectral resolution or decreasing the time stepping does not change the results (not shown). The boundary condition at the left boundary is kept constant throughout the experiment and each experiment is run until steady state is reached, which takes on average the time for a wave of period $T_{m0,-1}$ to cross the domain (0.5-1.3 days). For the WW3 configuration used here, numerical errors are small enough such that in control cases without current forcing, all bulk quantities of the wave field in the entire domain are uniform, constant, and equal to the boundary condition, with standard deviation on the order of 10^{-6} for all variables (not shown). In other words, without currents, H_s would be equal to 1 m, θ_w would be equal to 270°, σ_θ would be equal to 12.4°, and $T_{m0,-1}$ would be equal to the chosen boundary condition mean period, everywhere. We refer the reader to the Appendix for a list of switches used to compile WW3.

To explore how different properties of the flow affect the wave field, we force WW3 in

Table 4.1: Parameter space used for the simulations with synthetic currents. The combination of these parameters result in 72 possibilities that are each run 50 times, yielding a total of 3600 model runs.

Parameter space						
Divergence fraction (α)	0.0	0.2	0.4	0.6	0.8	1.0
Spectral slope ($\mathbb{S}$)	-5/3	-2.0	-2.5	-3.0		
Wave mean period ($T_{m0,-1}$)	7.0 s	10.3 s	16.6 s			

the configuration described above using an ensemble of synthetic surface currents created as described in Section 4.2.1. Each realization of this ensemble consists of 24 possible cases (see Table 4.1) that are run for three initial different values of $T_{m0,-1}$, yielding a total of 72 possible cases per realization. We run 50 realizations, which corresponds to a total of 3600 experiments. In addition, the response of the wave field to realistic currents is assessed using surface currents from the llc4320 to force the same WW3 setup. Without loss of generality, we only ran simulations with an initial mean period of 10.3 s with the llc4320 currents.

4.3 Results

4.3.1 Spatial variability of bulk wave parameters

We begin by analyzing the spatial variability of bulk quantities of the wave field, namely mean direction, significant wave height, mean period, and directional spreading. For the sake of clarity, here we discuss snapshots from WW3 forced by one realization of synthetic currents with $KE = 0.01$ m^2 s^{-2} and for waves with initial mean period of 10.3 s, although the same discussion applies for the entire ensemble. Each figure is organized as follows:

- Along a fixed row, all panels were forced with currents that have the same kinetic energy spectrum $\tilde{E}(q)$ and different divergence fractions α, which increases from $\alpha = 0$ (left, purely rotational) to $\alpha = 1$ (right, purely divergent).

- Along a fixed column, all panels were forced with currents that have the same divergence fraction and different kinetic energy spectral slope, which varies from a shallow slope (top, $q^{-5/3}$) to a steep slope (bottom, q^{-3}).
- The results are interpreted as deviations from a simulation with no current forcing, in which all bulk quantities are uniform and equal across all panels (i.e, all panels would be entirely filled with the same color).

Mean Direction

Figure 4.3 shows snapshots of mean direction θ_w. Close to the left boundary, θ_w is nearly uniform and equal to the boundary condition at the left boundary ($\theta_w = 270°$). As the waves propagate through the domain, the currents may modify the mean direction at a given location by both refraction and advection of wave action (where the latter effect is of order ϵ). Refraction is larger for cases where the currents are mostly rotational (first two columns) than cases where currents are mostly divergent (last two columns). This result is consistent with the predictions from ray theory: in the limit of weak currents one can approximate the curvature of individual rays (how much the rays refract) by the ratio between the vorticity (ζ) of the flow and the group velocity of the waves (Kenyon, 1971b; Landau and Lifshitz, 1987b; Dysthe, 2001b). Thus, in the last column where the flow is purely divergent ($\zeta = 0$), θ_w does not deviate much from the initial condition. Although we only show snapshots from one realization, the discussion above applies to the entire ensemble. For waves that have $T_{m0,-1} = 10.3$ s, the standard deviation of the θ_w across all realizations decreases from $\approx 2°$ when $\alpha = 0$ to $\approx 0.7°$ when $\alpha = 1$, for all spectral slopes.

Significant wave height

Strong refraction leads to strong convergences and divergences of wave action, which result in spatial gradients of significant wave height (Figure 4.4). As a consequence, gradients of H_s are stronger in the first two columns (where the flow has more vorticity) than in the last

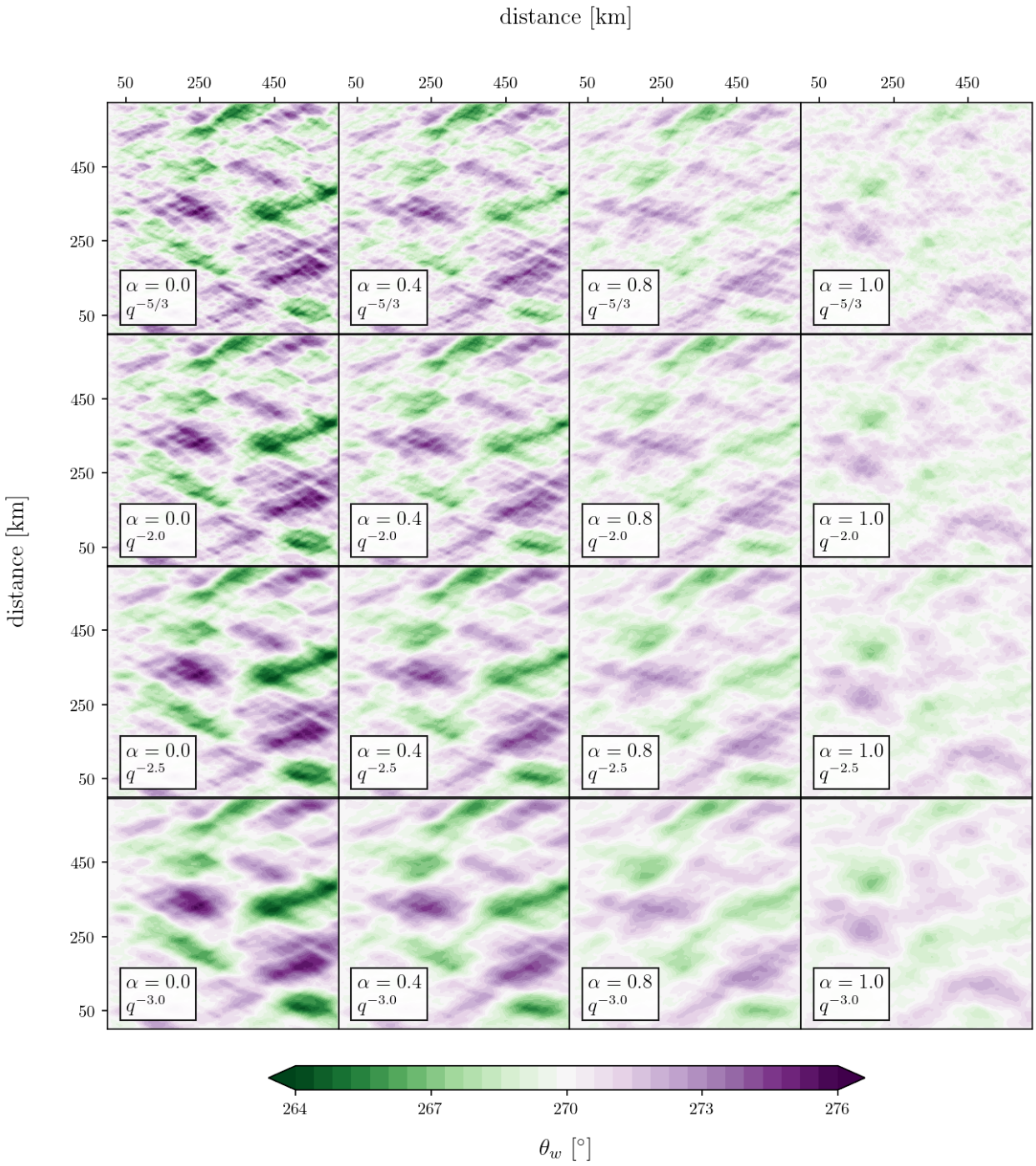

Figure 4.3: Mean direction (θ_w) for one realization of the idealized simulations spanning the entire parameter space, which consists of four spectral slopes ($q^{-5/3}, q^{-2}, q^{-2.5}, q^{-3}$) and four divergence fractions $\alpha = (0, 0.4, 0.8, 1)$, where $\alpha = 0$ corresponds to a purely rotational flow and $\alpha = 1$ to a purely divergent flow. For a case without currents, θ_w would be equal to 270° in the entire domain.

two columns (where the flow has more divergence). For these purely rotational currents that have $KE = 0.01$ m^2 s^{-2} and waves with $T_{m0,-1}$ on the order of 10 s, we observe a change of up to 20% in H_s at scales of tens of kilometers. Additionally, visual inspection of Figure 4.4 show that current fields with shallow spectral slope (top two rows) result in variability of H_s at shorter spatial scales in comparison to steep spectral slopes (bottom two rows) suggesting a scale dependency between the current forcing and the wave response. A striking feature of Figure 4.4 is the abrupt change in the spatial variability of H_s from $\alpha = 0.8$ to $\alpha = 1$. In the first three columns, increasing the divergence fraction (going from left to right) results in weaker gradients of H_s but with a similar spatial pattern in each column. However, the picture changes completely when the flow is purely divergent (last column). To better characterize this transition, we have run two additional sets of simulations with $\alpha = 0.9$ and $\alpha = 0.95$. Figure 4.5 shows the spatial correlation of H_s between the case with $\alpha = 0$ and all other values of α. Regardless of the spectral slope, the correlation drops from about 0.5 for $\alpha = 0.95$ to zero for $\alpha = 1$, which means that even if only 5% of the kinetic energy of the flow is in the rotational component, the spatial variability of H_s is still remarkably similar to the purely rotational case.

Mean period

Why is the spatial variability of H_s for the purely divergent case in Figure 4.4 so different from the other cases? For the purely divergent case ($\alpha = 1$) the vorticity is zero, and refraction no longer dominates the action balance equation. Conservation of the absolute frequency $\omega = \sigma + \boldsymbol{kU}$ leads to a change of order ϵ in the intrinsic frequency, which in turn changes the wave energy via conservation of wave action. Then, in terms of bulk parameters, an increase in $T_{m0,-1}$ would correspond to a decrease in H_s for action to be conserved. Figure 4.6 shows the mean period for the respective cases discussed in Figures 4.3 and 4.4. Comparing Figures 4.4 and 4.6, we can see that the spatial pattern of H_s in the purely divergent case (Figure 4.4, last column) nearly matches the spatial pattern of the mean period (Figure 4.6, last column).

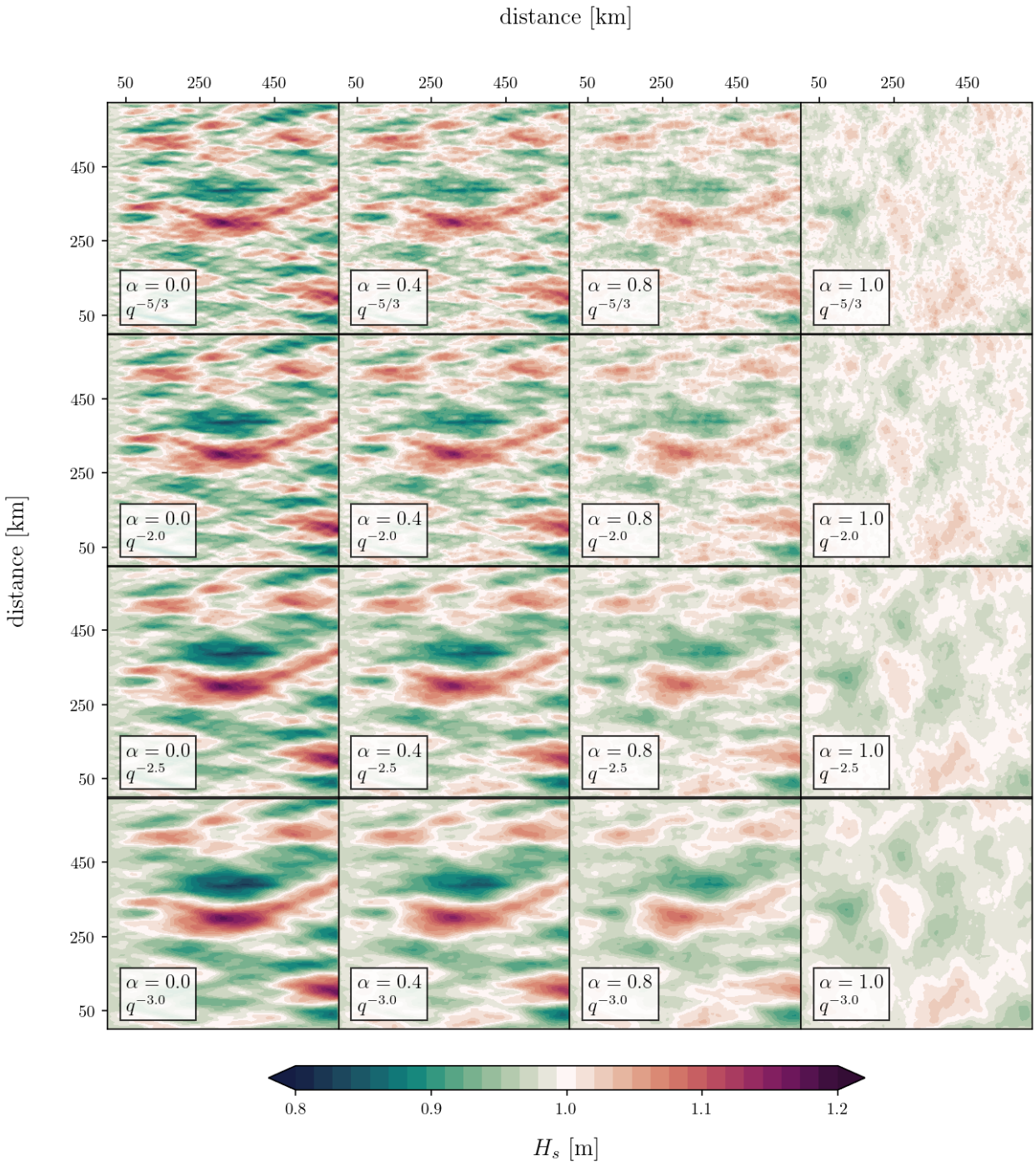

Figure 4.4: Same as Figure 4.3 but for the significant wave height (H_s). For a case without currents, H_s would be equal to 1 m in the entire domain for all panels.

More specifically, blue regions in the last column of Figure 4.6 (decrease in $T_{m0,-1}$) correspond to red regions in Figure 4.4 (increase in H_s). Computing the spatial correlation between H_s

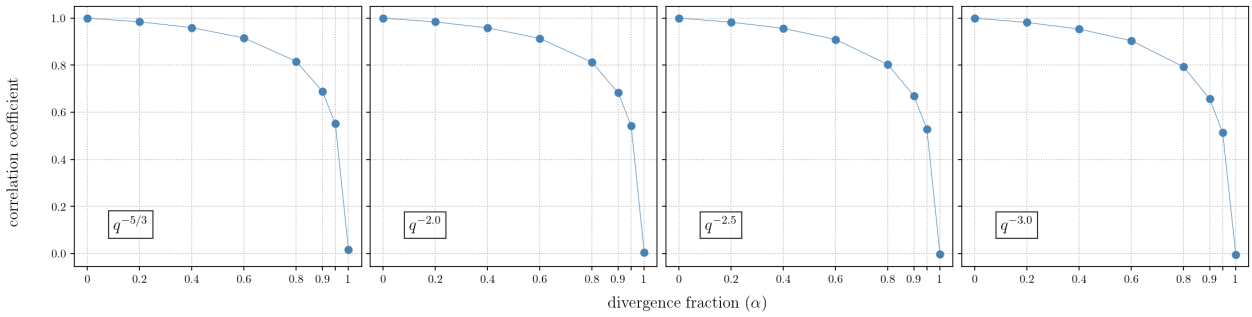

Figure 4.5: Correlation coefficient as a function of α between the significant wave height for the case $\alpha = 0$ and all other cases. Each panel corresponds to a different spectral slope. The correlation coefficients for each value of α were averaged across 20 realizations. The standard error of the mean is too small to be noticeable on the plot.

and $T_{m0,-1}$ for $\alpha = 1.0$ and averaging across all realizations results in correlation coefficients of -0.72, -0.73, -0.77, and -0.81 for $\mathbb{S} = 5/3$, 2, 2.5, and 3, respectively. Additionally, a back-of-the-envelope calculation (see page 74 of Phillips (1966)) using a current speed variation of the order of 0.5 m s^{-1} (as in Figure 4.2) and group velocity of 8 m s^{-1} (corresponding to $T_{m0,-1} = 10.3$ s) leads to a change of 3% in $T_{m0,-1}$ and a corresponding change of about 6% in H_s, which is in agreement with the values observed in the last column of Figures 4.4 and 4.6.

Directional spreading

Figure 4.7 shows snapshots of the directional spreading (σ_θ). Waves enter the domain from the left boundary with an initial directional spreading of 12.4°. As the waves propagate through the domain they are refracted by the currents which results in higher directional spreading, increasing from left ($x = 0$) to right ($x = 600$) on each panel. As shown in Figure 4.3, more vorticity leads to stronger refraction; thus σ_θ is higher for the purely rotational flow (first column, $\alpha = 0$), and it decreases as α increases. Figure 4.7 also reveals that shallower spectral slopes (top two rows) produce higher directional spreading than steep spectral slopes (bottom two rows). Perhaps the most interesting feature of Figure 4.7 is the fact that there is virtually no change in the directional spreading for purely divergent flows (last column,

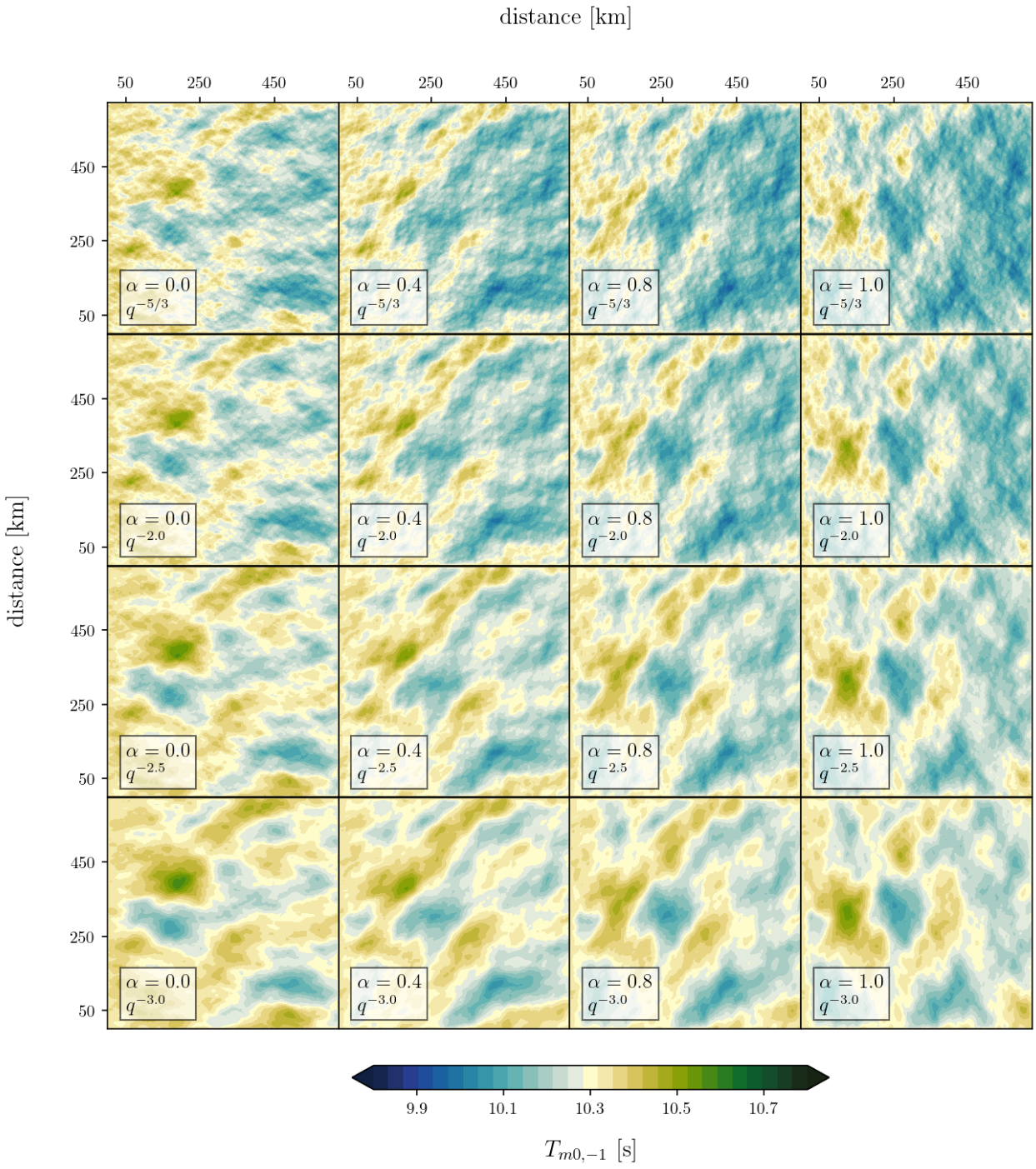

Figure 4.6: Same as Figure 4.3 but for the mean period ($T_{m0,-1}$). In the absence of currents, $T_{m0,-1}$ would be equal to 10.3 s in the entire domain for all panels.

$\alpha = 1$). Using a ray tracing approach, (Villas Bôas and Young, 2020, henceforth VBY20) have recently shown that the divergent component of the flow has no contribution to the

directional diffusion of wave action. Our results corroborate the VBY20 results in a spectral wave modeling framework. VBY20 arrived at an analytical expression for the variance of the wave direction that depends on the kinetic energy spectrum of the rotational component of the flow only and also found larger directional variance for shallow spectral slopes. Although there is no direct relationship between the direction of monochromatic wave rays and the mean direction computed from a wave spectrum, the directional spreading (as defined in 4.21) provides an energy-weighted proxy for the variance of wave direction discussed by VBY20.

4.3.2 Significant wave height response to vorticity and divergence

Synthetic currents

So far we have seen that spatial gradients of H_s are stronger for cases where most of the kinetic energy of the flow is in the rotational component (Fig. 4.4) and that this coincides with the cases where refraction is also stronger (Fig. 4.3). Building on the results from VBY20 that found no directional diffusion of wave action by the divergent component of the flow and what we have shown in section 4.3.1, we hypothesize that the spatial variability of H_s is determined by the spatial variability of the **rotational** component of the flow. To test this hypothesis we run an additional set of experiments in which we double the kinetic energy of the purely rotational flow by adding an equally energetic potential component. One realization of such an experiment (for $\mathbb{S} = 2.5$) is shown in Figure 4.8. In case (A) the flow is purely rotational with $KE = 0.01$ m^2 s^{-2}. In case (B) $KE = 0.02$ m^2 s^{-2}, where the rotational component was kept the same and the additional energy was obtained by adding a purely divergent flow to (A). One would expect that stronger currents would have a larger impact on the wave field; however, the respective H_s responses (C and D) are fairly similar (rms difference of 0.01 m), providing evidence that the spatial variability of H_s at these scales is not affected by the potential component of the flow.

To further verify our hypothesis, we ran 50 realizations of experiments with the same

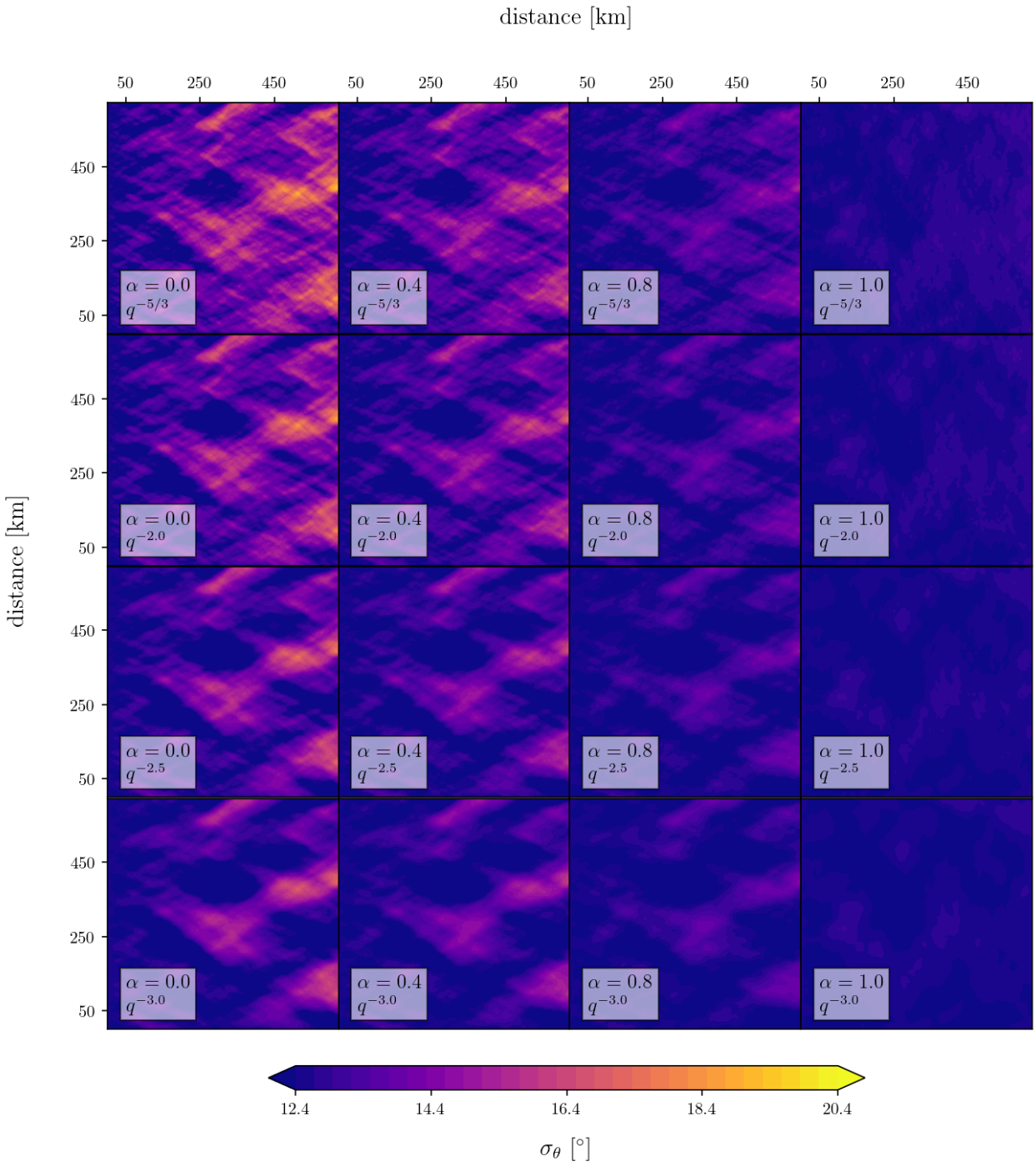

Figure 4.7: Same as Figure 4.3 but for the directional spreading (σ_θ). In the absence of currents, σ_θ would be equal to 12.4° in the entire domain for all panels.

setup as the example shown in Figure 4.8 and computed the average wavenumber spectra of surface currents and significant wave heights for all kinetic energy spectral slopes considered

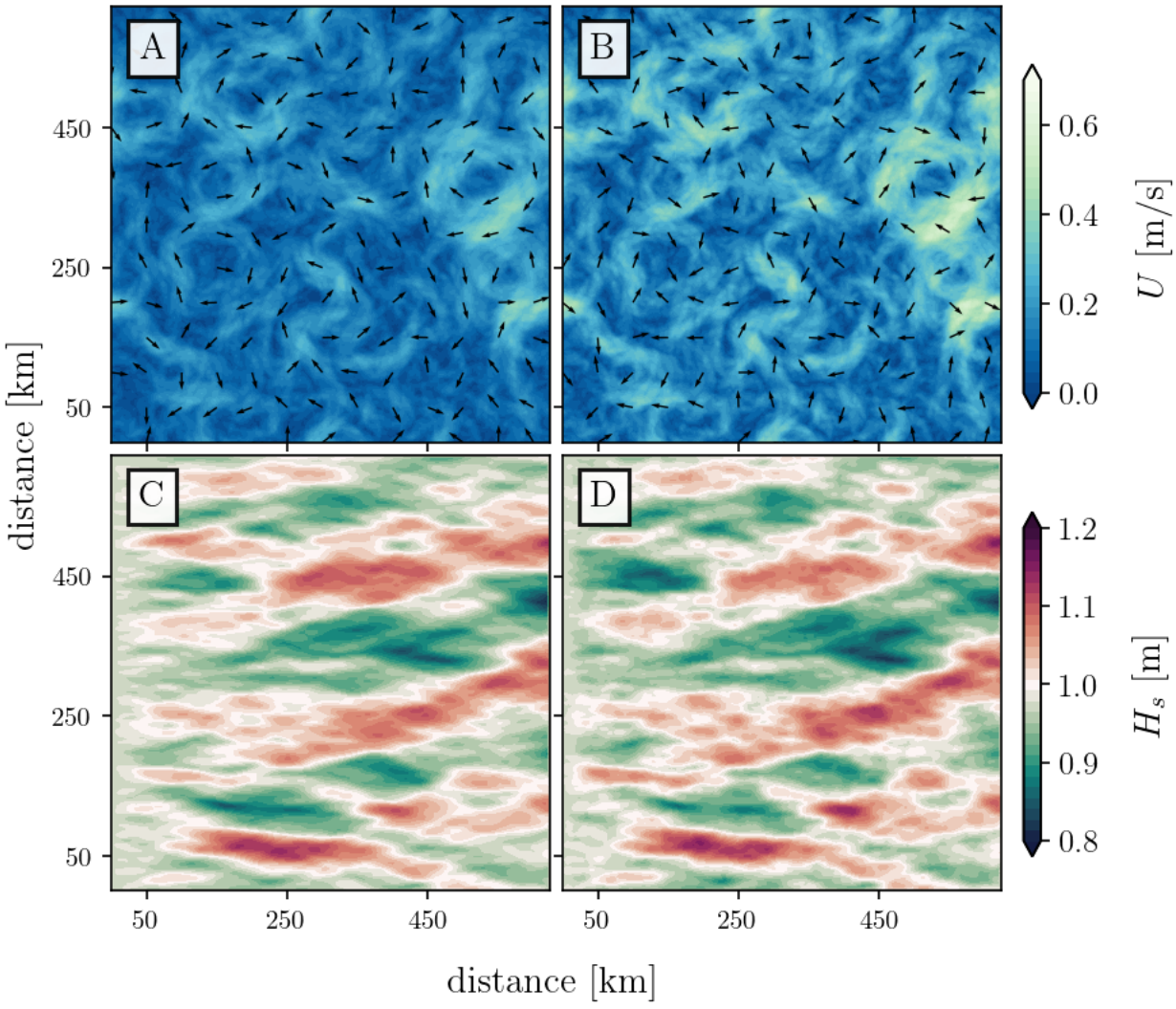

Figure 4.8: Surface current forcing (A, B) and respective significant wave heights H_s (C, D). In panel A the flow is purely rotational ($\alpha = 0$) and has kinetic energy $KE = 0.01$ m^2/s^2 which produces the H_s shown in C. The flow in panel B was obtained by adding a purely divergent component to A, resulting in a current twice as energetic ($KE = 0.02$ m^2/s^2) with $\alpha = 0.5$ and corresponding H_s shown in D. In both cases the flow has a kinetic energy spectral slope $\mathbb{S} = 2.5$.

in this study. Although the flow is isotropic, it is clear from the snapshots of H_s (Fig. 4.8) that the surface wave response is not, since the experimental setup produces waves propagating in a preferential direction (from left to right). Thus, instead of using the isotropic spectrum, we analyze the one-dimensional wavenumber spectrum as a function of the q_2 wavenumber,

obtained by integrating the 2D spectra in the q_1 wavenumber direction

$$\tilde{E}(q_2) = \int \tilde{E}(\boldsymbol{q}) dq_1, \tag{4.14}$$

where $\tilde{E}(q_2)$ is the one-dimensional spectrum and $\boldsymbol{q} = (q_1, q_2)$ is the horizontal wavenumber vector. Additionally, to avoid the transition region close to the left boundary, where the statistics are not yet stationary, we neglect the first 200 km of the domain when computing the wavenumber spectra.

Figure 4.9 confirms our hypothesis that, to leading order, the spatial variability of H_s is not affected by the divergent component of the flow. Although we forced the wave model with currents that are twice as energetic (dashed black), the resulting wavenumber spectra of H_s (dashed green) are indistinguishable from the purely rotational case (solid green) and this is true for all spectral slopes. Another remarkable feature to note in Figure 4.9 is that at scales between 15 and 200 km (gray shaded box) the spectral slope of H_s nearly follows the KE spectral slope, meaning that shallow H_s spectral slopes are associated with shallow KE slopes (e.g., $q^{-5/3}$), while steep H_s spectral slopes are associated with steep KE slopes (e.g., q^{-3}).

Realistic current forcing

A question that naturally arises from the results discussed up to this point of this manuscript is if the same behavior would be observed for realistic currents. A detailed analysis of the seasonality of kinetic energy at submesoscales in the CCS was recently carried out by Chereskin et al. (2019) using both observational data and the output from the llc4320 simulation. The authors show that in this region, KE is dominated by balanced motions (rotational) in late winter/spring, whereas internal waves and other divergent motions dominate the KE in summer/fall. From our experiments with idealized currents, we expect the spatial variability of H_s to respond to the rotational component of the flow. Thus, a seasonality in

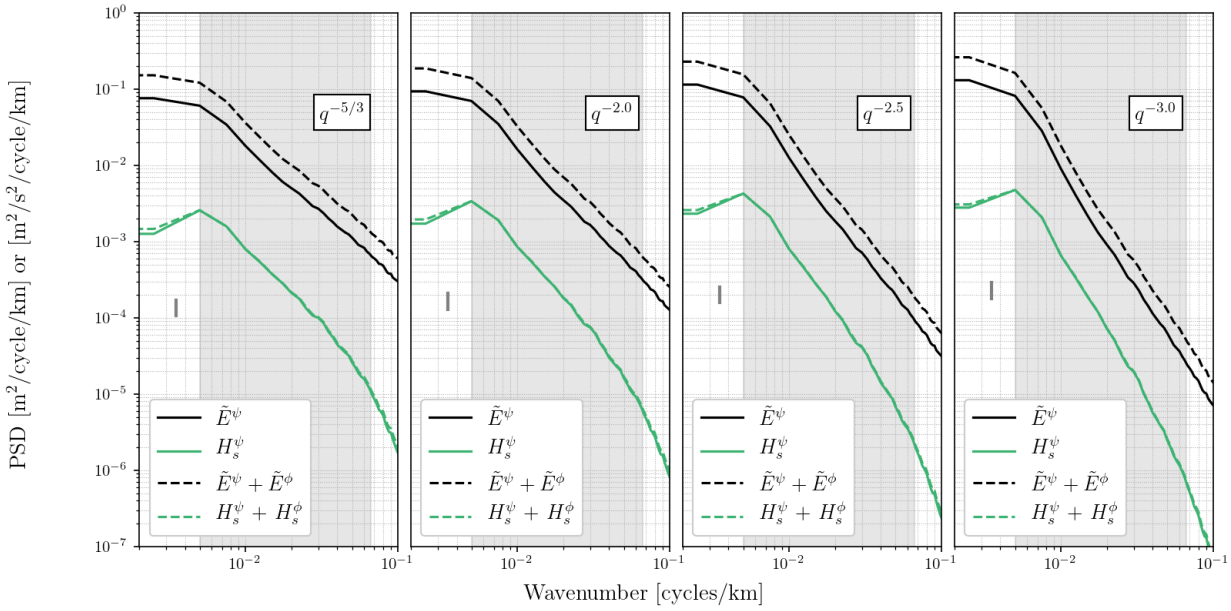

Figure 4.9: Wavenumber spectra of kinetic energy for a purely rotational flow with $KE = 0.01$ m^2/s^2 (E^{ψ}, solid black) and combined rotational and potential flow with $KE = 0.02$ m^2/s^2 ($E^{\psi} + E^{\phi}$, dashed black). Each panel shows different spectral slopes as indicated in the upper box. The respective wavenumber spectra for the significant wave height are shown in green, solid for the purely rotational case ($H_s{}^{\psi}$) and dashed for the combined rotational and potential ($H_s{}^{\psi} + H_s{}^{\phi}$). These 1D spectra were obtained by integrating the 2D spectra in the q_1 wavenumber direction, thus representing the variance density as a function of the q_2 wavenumber. The spectra were averaged across 50 realizations, and the error bar is shown as a light gray line. For clarity, the H_s spectra were scaled by a factor of 10^{-1}. The gray shaded box indicates the wavelength range between 200 km and 15 km.

the rotational KE in the CCS region, should lead to a seasonality in the H_s wavenumber spectrum, whereas changes in the divergent component of the KE should not significantly change the H_s spectrum.

To test this hypothesis, an equivalent setup was used to run WW3 forced with realistic currents from the MITgcm llc4320 in the CCS region, as explained in Section 4.2.1. Figure 4.10 shows snapshots of surface relative vorticity (top) from the llc4320 in the winter (left) and summer (right) and the H_s (bottom) obtained from WW3 forced with the respective llc4320 currents. In the winter, strong vorticity results in strong gradients in H_s that are comparable with the values obtained for small α in Figure 4.4 (up to 20% change in H_s). In contrast, H_s gradients in the summer are much weaker as a consequence of a weak vorticity

field. This example illustrates how the seasonality of the submesoscale in the CCS may affect surface waves leading to strong seasonality in the variations of gradients of H_s.

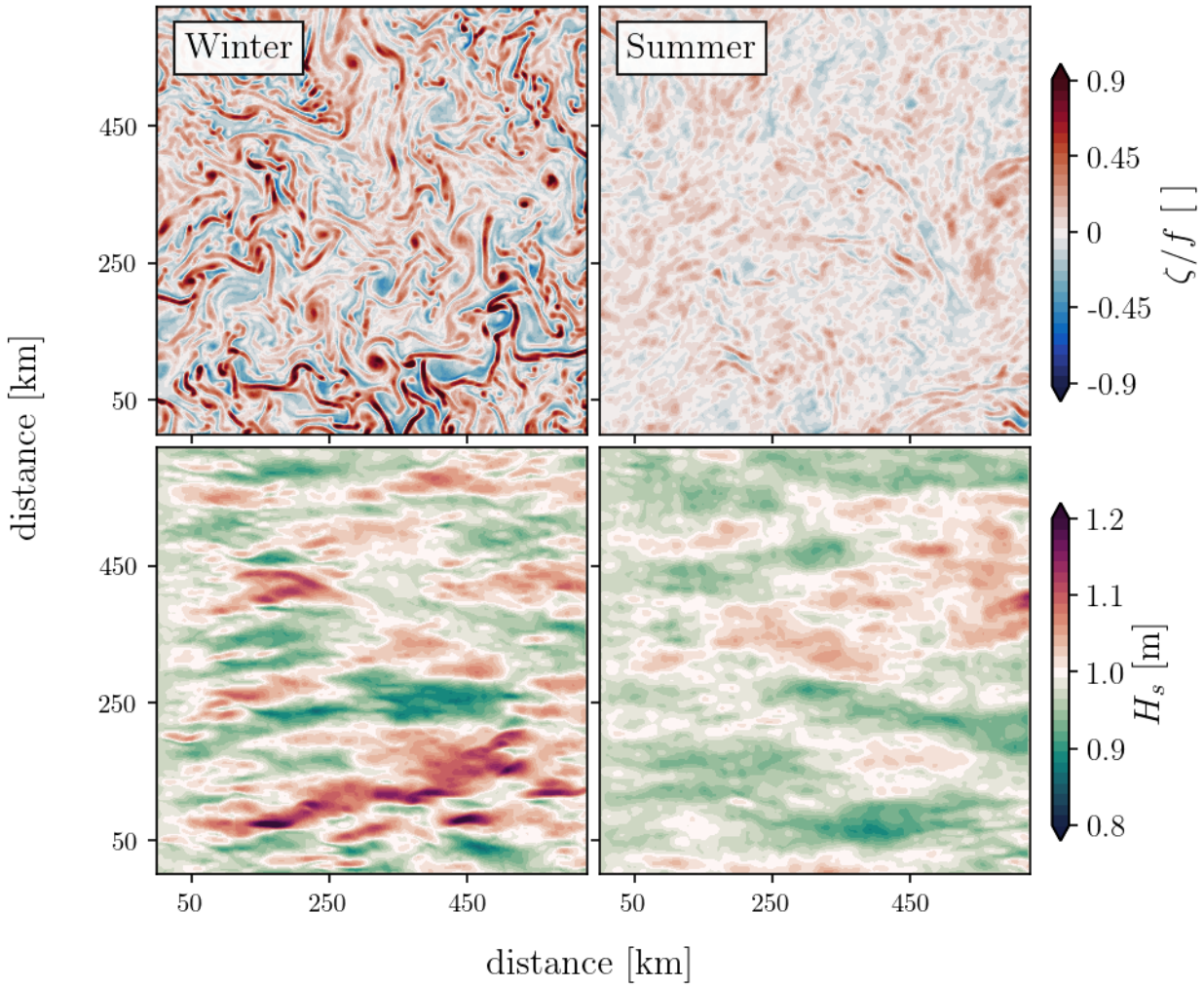

Figure 4.10: Snapshots of surface relative vorticity (top) from the llc4320 in the winter (left) and summer (right) and the significant wave height H_s (bottom) obtained from WW3 forced by the respective llc4320 currents. The vorticity is normalized by the local Coriolis parameter. Note that the color scale for H_s is the same used in the previous plots.

For the following analysis, we applied a Helmholtz decomposition to separate the rotational and divergent components of the llc4320 currents (e.g., Bühler et al., 2014b; Rocha et al., 2016a). We start by considering January and July as examples. The top left panel of Figure 4.11 shows KE spectra of the rotational ($\tilde{E}^{\psi}$) component of the flow in January (solid blue) and July (solid red). In agreement with the results from Chereskin et al. (2019),

we observe higher values of $\tilde{E}^{\psi}$ in January at all wavenumbers. In contrast, the KE spectra of the divergent component $\tilde{E}^{\phi}$ (Fig 4.11, top right) do not change much between these two months. Now, if we focus on the significant wave height spectra (dashed), we see that the H_s spectrum is also more energetic in January (blue), particularly at scales between 200 km and 15 km (shaded box). Since $\tilde{E}^{\phi}$ is nearly constant between January and July, we conclude that the observed change in the H_s spectrum is caused by the KE in the rotational component of the flow.

We can further analyze this problem by looking at the opposite case: we choose two months where there is a significant difference in the divergent component of the KE, but the rotational component remains somewhat constant. The bottom two panels of Figure 4.11 illustrate this scenario. Between October (purple) and March (orange), $\tilde{E}^{\psi}$ is relatively constant at scales between 200 km and 15 km (Fig. 4.11 bottom left panel); however, $\tilde{E}^{\phi}$ is much larger in October than March (Fig. 4.11 bottom right panel). Despite $\tilde{E}^{\phi}$ being larger in October, the H_s spectra do not change significantly between October and March reinforcing the idea that divergent component of the flow does not affect the spatial variability of H_s.

Considering that for the waves analyzed in this paper (narrow-banded swell), the dominant balance in the conservation of wave action in (4.8) is between advection (second term on the left-hand side) and refraction (last term on the left-hand side), we expect a relationship between spatial gradients of significant wave height and the vertical vorticity of the flow. Applying these scaling arguments to (4.8) allows us to arrive at the following relation (see supplemental material for more details)

$$c\frac{|\nabla H_s|_{rms}}{\langle H_s \rangle} \propto \mathbb{S}\ \zeta_{rms}\,, \tag{4.15}$$

where c is the group speed, $|\nabla H_s|_{rms}$ is the root-mean-square (rms) significant wave height gradient, $\langle H_s \rangle$ is the mean significant wave height, $\mathbb{S}$ is the spectral slope of the flow, and ζ_{rms} is the rms vertical vorticity of the flow.

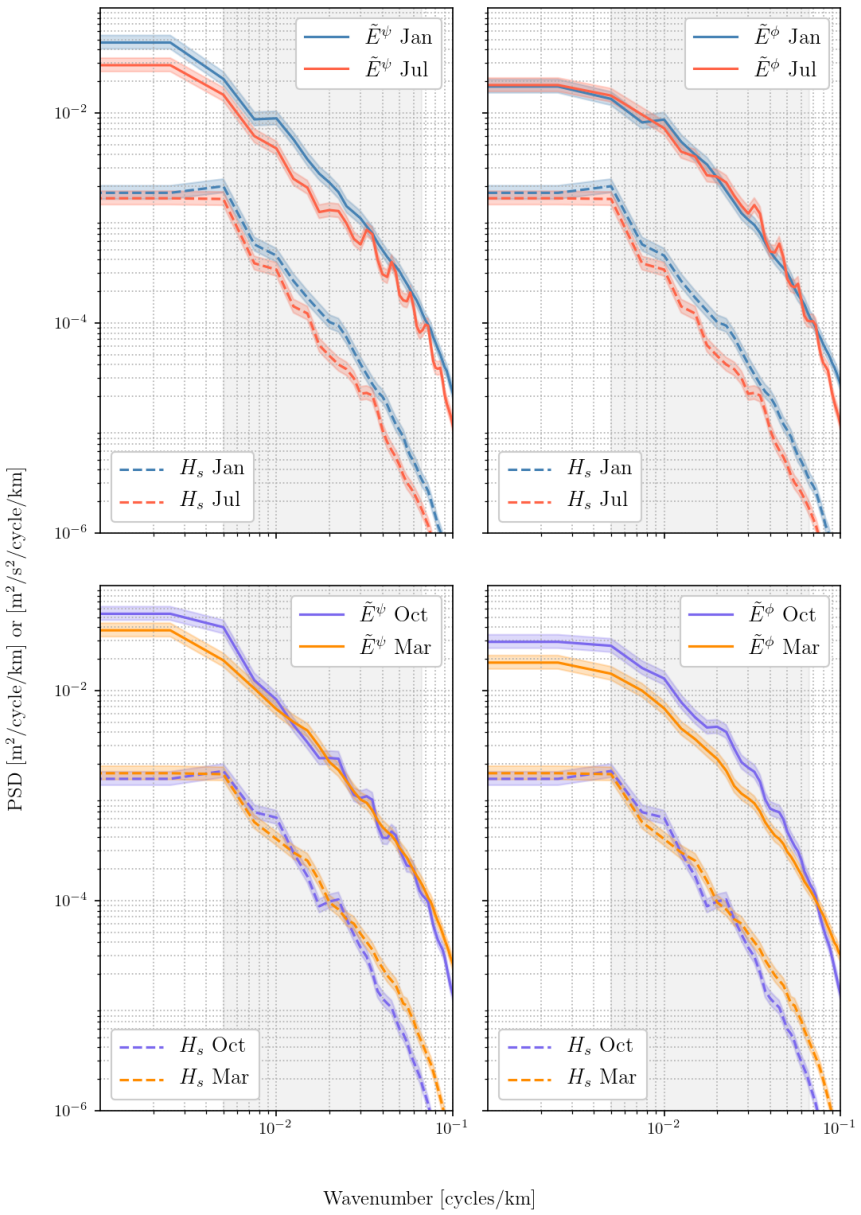

Figure 4.11: Wavenumber spectra of kinetic energy KE from the MITgcm llc4320 (solid), and the respective spectra of significant wave height H_s (dashed). The spectra are shown as monthly averages for January (blue), July (red), October (purple), and March (orange). Panels on the left show the KE spectra for the rotational component of the flow ($\tilde{E}^{\psi}$) and on the right for the divergent component ($\tilde{E}^{\phi}$). To facilitate the comparison, the same H_s spectra is plotted both on the left and right panels. All H_s spectra were scaled by a factor of 10^{-1}. The color shades represent the 95% confidence limit. The gray shaded box indicates the wavelength range between 200 km and 15 km.

Figure 4.12 illustrates the scaling (4.15): results for experiments using both synthetic (dots) and realistic (crosses) currents all collapse to the same line (see supplemental material

Figure S1 for sequential illustrations of the collapse). In Figure 4.12, light blue dots were computed from the ensemble described in Table 4.1 that have mean kinetic energy $KE = 0.01$ m^2 s^{-2}. Dark blue dots correspond to a total of 480 realizations of experiments with the same parameter space as in Table 4.1, but with $KE = 0.005$ m^2 s^{-2} and only for for waves with initial $T_{m0,-1} = 10.3$ s. Note that all cases with $\alpha = 1.0$, for which the vorticity is zero, were excluded from this analysis. Black crosses correspond to experiments forced by the llc4320 currents, for which the spectral slope, divergence fraction, and mean kinetic energy are not prescribed. The experiments using the llc4320 currents are also only for waves with initial $T_{m0,-1} = 10.3$ s and correspond to a total of 1464 realizations. The right-hand side of (4.15) is scaled by the kinetic energy spectral slope $\mathbb{S}$. The concept of a spectral slope for the llc4320 currents is subjective, and here it was estimated by doing a linear fit (in log space) to each spectrum between wavelengths of 10 km and 100 km.

The relationship in (4.15) synthesizes the idea that spatial gradients of H_s are caused by vorticity, and it provides a direct connection between bulk wave quantities (left-hand side) and kinematic properties of the flow (right-hand side) that applies to a wide range of currents and wave conditions. For all three cases shown in Figure 4.12, the correlation coefficient is greater than 0.9.

We have shown that surface waves contain information on statistical properties of the flow, such as the kinetic energy spectrum and the rms vorticity. Now, do surface wave gradients contain phase information of current gradients? If we go back to the limit of a monochromatic wave with propagation described by the ray equations, the evolution of the wave direction can be written as

$$\theta_t + (\boldsymbol{U} + \boldsymbol{c})\boldsymbol{\nabla}\theta = -\frac{1}{k}\hat{\boldsymbol{n}}\boldsymbol{\nabla}\left(\boldsymbol{k}\boldsymbol{U}\right) , \tag{4.16}$$

where $\hat{\boldsymbol{n}}$ is a unit vector in the direction perpendicular to the wavenumber $\boldsymbol{k}$. We remind the reader that we are considering the steady-state solution with $\varepsilon = U/c \ll 1$, so defining $\nabla_{\parallel} \overset{\text{def}}{=} \hat{\boldsymbol{k}} \cdot \boldsymbol{\nabla}$ and $\nabla_{\perp} \overset{\text{def}}{=} \hat{\boldsymbol{n}} \cdot \boldsymbol{\nabla}$ as the gradient in the direction parallel and perpendicular to

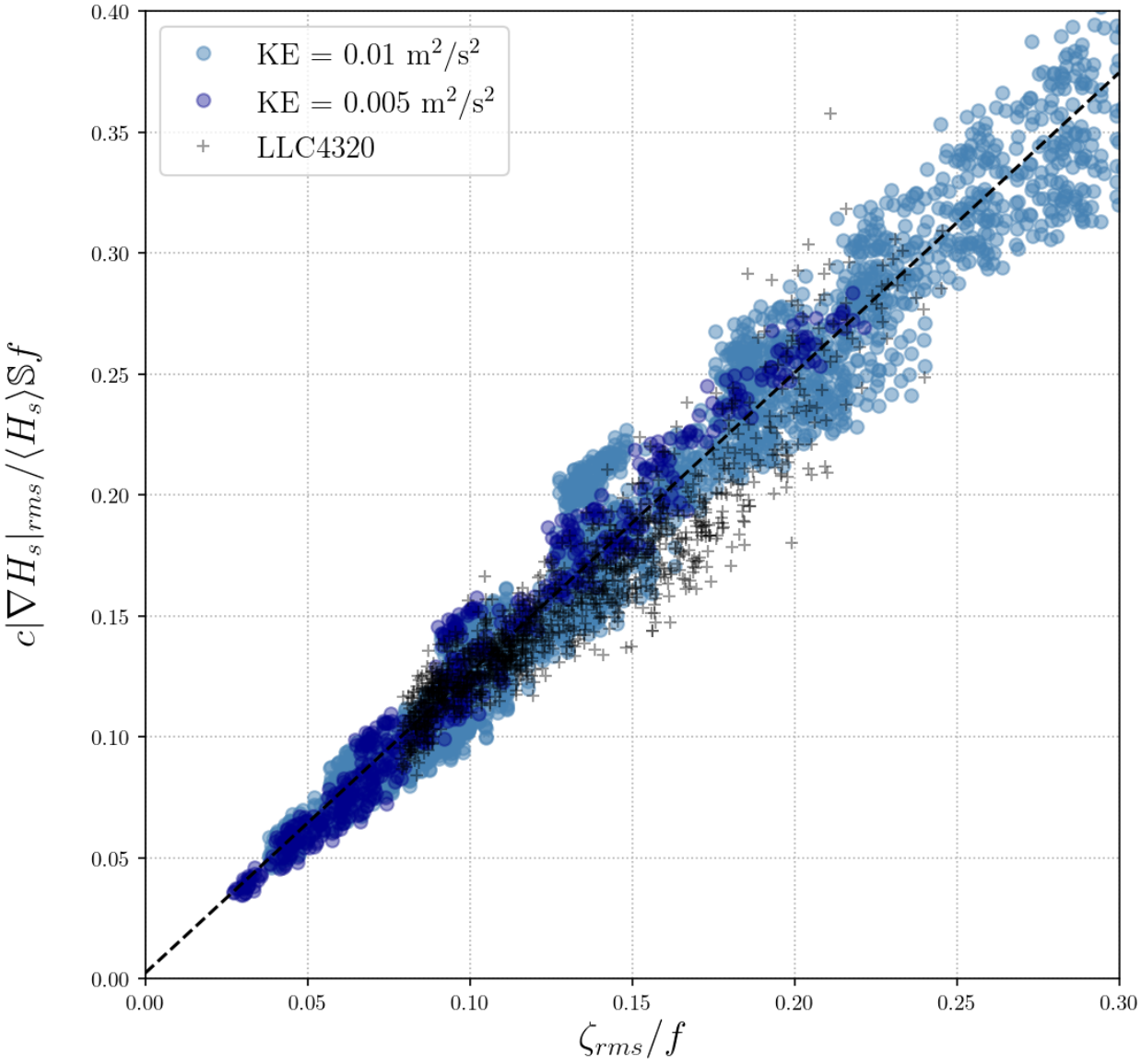

Figure 4.12: Scatter plot of non-dimensional root-mean-square (rms) significant wave height gradient as a function of normalized rms vorticity. Light blue dots are from the ensemble described in Table 4.1, that have mean kinetic energy $KE = 0.01$ m^2 s^{-2}. Dark blue dots correspond to a total of 480 realizations of experiments with the same parameter space as in Table 4.1, but with $KE = 0.005$ m^2 s^{-2} and only for for waves with initial $T_{m0,-1} = 10.3$ s. Black crosses correspond experiments forced by the llc4320 currents, for which the spectral slope, divergence fraction, and mean kinetic energy are not prescribe. The experiments using the llc4320 currents are also only for waves with initial $T_{m0,-1} = 10.3$ s and correspond to a total of 1464 realizations. For this plot, both sides of (4.15) were normalized by the mean Coriolis parameter in the CCS region ($f = 7.8 \times 10^{-5}$) for all realizations.

the wave number direction, respectively, we can write (4.16) to $O(\varepsilon)$ as:

$$c\ \nabla_{\parallel}\theta = -\nabla_{\perp}U^{k}\,, \tag{4.17}$$

where U^k is the component of $\boldsymbol{U}$ in the direction of the wavenumber $\boldsymbol{k}$ (along-wave). Equation (4.17) says that, for monochromatic waves, if we know the wave direction and group velocity everywhere, we can retrieve the gradient of the along-wave component of the current in the direction perpendicular to the wave propagation.

Figure 4.S1(A) shows a snapshot of surface speed from the llc4320 where we observe a sharp diagonal front on the right side of the domain. Now, we apply (4.17) to a narrow-banded wave spectrum using the group velocity at the mean period ($\mathrm{c} = \mathrm{g}T_{m0,-1}/4\pi$) and the mean wave direction ($\theta = \theta_w$). Panel (B) of Figure 4.S1 shows the gradient of the along-wave component of the current in the direction perpendicular to the mean direction and is our "truth", meaning that panel (B) was computed straight from the llc4320 currents. Note that the front described in panel (A) appears in panel (B) as a diagonal line in shades of blue. Panel (C) shows the same gradient as in (B), but now computed using the left-hand side of (4.17), which depends only on wave quantities. In other words, without any knowledge of the current field, a "beam" of short-crested, narrow-banded waves is able to provide insight on the spatial structure of current gradients. For the case shown in Figure 4.S1, the spatial correlation coefficient between panels B and C is on the order of 0.6. Similar analysis was performed for all llc2320 current snapshots. Because refraction is a non-local effect, we expect the skill of (4.17) to be higher close to the left boundary and decrease as the waves propagate through the domain. Additionally, we also expect the skill to vary seasonally, depending on the relative contribution of the rotational and divergent part to the surface kinetic energy. This inhomogeneity in the skill of (4.17) was quantified through the correlation coefficient shown in the supplemental material Figure S2.

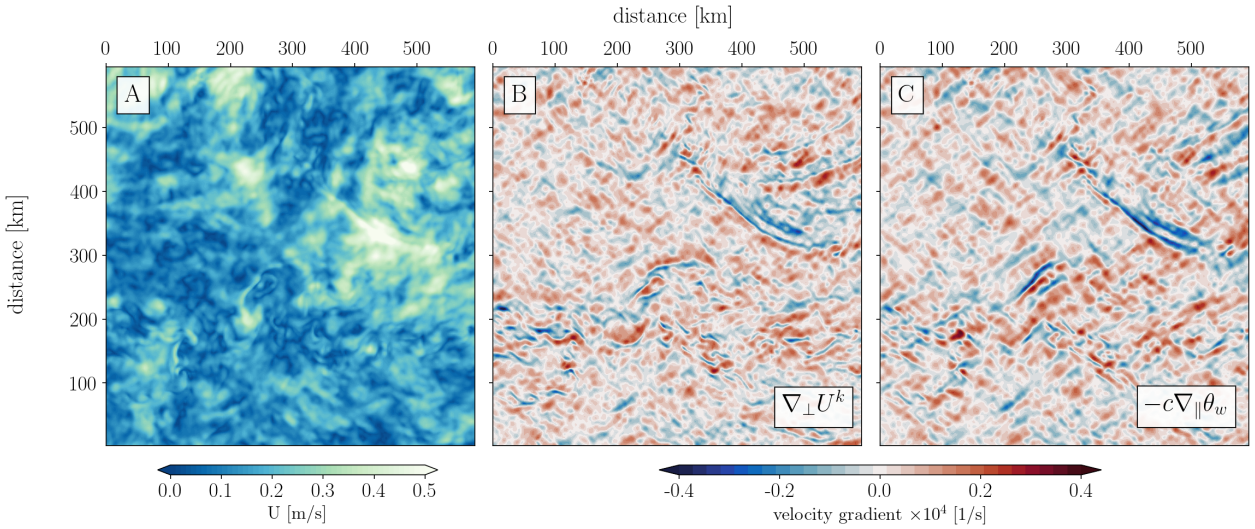

Figure 4.13: (A) Snapshot of surface speed from the llc4320; (B) gradient of the the along-wave component of the current shown in (A) in the direction perpendicular to the wave propagation (see eq. 4.17); (C) group velocity at the mean period multiplied by the gradient of the mean wave direction in the direction parallel to the wave propagation. Note that the sharp diagonal front on the right side of panel (A) appears as a dark blue diagonal line both in panels (B) and (C).

4.4 Summary and Conclusions

An ensemble of synthetic currents were used to force WAVEWATCH III and assess the relative importance of current divergence and vorticity in modifying several properties of the wave field. Using these idealized numerical simulations we were able to show that the spatial variability of the significant wave height is driven by the rotational component of the flow, which is the only component that has vorticity. For the type of waves considered in this paper, which have relatively long period and are not subject to wind-forcing, we found refraction to be the main mechanism leading to spatial gradients of wave heights. These findings corroborate the results from Ardhuin et al. (2017), who have done experiments turning the refraction term on and off in the wave model as opposed to controlling the vorticity in the currents, as well as the observational results from Quilfen and Chapron (2019). Further, we have also shown that purely divergent flows do not contribute to increasing the directional spreading of the wave field, which extends the results from Villas Bôas and Young (2020) to

a narrow-banded wave spectrum.

Gradients of wave quantities contain information about statistical and kinematic properties of the flow. In particular, we have shown that the wavenumber spectrum of the significant wave height is highly sensitive to the nature of the underlying current. Our numerical results suggest that at scales from 15–200 km the spectral slope of H_s follows the spectral slope of the rotational component of the surface kinetic energy and, most remarkably, that variance of H_s is not affected by the kinetic energy contained in the divergent component of the flow.

The upcoming SWOT mission will measure the sea surface height (SSH) with the unprecedented spatial resolution of tens of kilometers. While conventional satellite altimetry has for decades provided us with a quasi-global picture of the ocean's geostrophic circulation, deriving velocities from SSH will pose a challenge for SWOT since at the SWOT scales, divergent (non-geostrophic) motions associates with tides, internal waves, and fronts may contribute to a significant portion of the SSH signal (Morrow et al., 2019). In response to that, community efforts have focused on strategies to separate balanced from unbalanced motions. One of the main takeaways from this paper is that surface waves respond differently to rotational (balanced) and divergent (unbalanced) flows, which may offer the possibility of using the wave information contained in the SWOT signal to help distinguish between these two dynamical regimes.

In addition to the synthetic current forcing, a set of idealized simulations with realistic currents from the MITgcm llc4320 model was run. Our results using the llc4320 demonstrate that waves are modulated by ocean currents over the scales of eddies and fronts even with the comparatively weak currents of the California Current System ($U < 0.5$ m s^{-1} and $\zeta = O(f)$). As a consequence, we observed that in the CCS region seasonal differences in the dominant regime and spatial scales of the background flow led to corresponding differences in H_S. Note that in a realistic scenario, the wave field itself would also experience a seasonal variability that is not associated with the currents. Here, we have focused on only the wave response to the seasonality of the currents.

Finally, the highly structured wave response to coherent features present in the llc4320 currents offers the possibility of using wave parameters to detect and characterize strong gradients in the velocity field. The case illustrated here relies on a "beam" of narrow banded swell and requires knowledge of the spatial variability of the wave frequency and direction. Understanding how surface waves respond to currents in a more realistic scenario and the extent to which wave information could be used to constrain ocean currents calls for joint observations of winds, currents, and waves. Efforts such as NASA's Sub-Mesoscale Ocean Dynamics Experiment (S-MODE, Farrar et al. (2020)) and Doppler oceanography satellite mission concepts such as the Winds and Currents Mission (WACM Rodríguez et al., 2019) and the Sea surface KInematics Multiscale monitoring (SKIM Ardhuin et al., 2019) will be of paramount importance to our understanding of how meso and submesoscale currents affect waves.

Appendix

4A WAVEWATCH III setup and bulk parameters

In this manuscript we used WAVEWATCH III version 5.16 compiled with the following switches:

F90 NOGRB NOPA LRB4 SCRIP SCRIPNC NC4 TRKNC DIST MPI PR3 UQ FLX0 LN1 ST4 STAB0 NL1 BT0 DB0 TR0 BS0 IC0 IS0 REF0 IG0 XX0 WNT2 WNX1 RWND CRT1 CRX1 O0 O1 O2 O2a O2b O2c O3 O4 O5 O6 O7.

The spectral grid used had 48 directions (7.5° resolution) and 32 frequencies with the lowest frequency equal to 0.04118 Hz and an increment factor of 1.1.) The spatial grid had 2.5 km resolution in both x and y and we used a global integration time step of 200 s, spatial advection time step of 50 s, spectral advection time step of 12 s, and minimum source term time step of 5 s.

The wave field was described using bulk parameters, which are computed within WW3

from integrals of the wave energy spectrum. Below is the formal definition of these parameters. For more details on the bulk parameters calculation and the numerical schemes used by WW3 we refer the reader to the WW3 user manual (WAVEWATCH III Development Group, 2016).

Significant Wave Height (H_s)

$$H_s = 4\sqrt{E}\,, \tag{4.18}$$

where

$$E = \int_0^{2\pi} \int_0^{\infty} E(\sigma, \theta) d\sigma d\theta\,. \tag{4.19}$$

Mean Period ($T_{m0,-1}$)

The mean period $T_{m0,-1}$ is the energy-weighted average of the wave period defined as:

$$T_{m0,-1} = \frac{1}{E} \int_0^{2\pi} \int_0^{\infty} \sigma^{-1} E(\sigma, \theta) d\sigma d\theta\,. \tag{4.20}$$

Directional Spreading (σ_θ)

$$\sigma_\theta = \left[2 \left\{ 1 - \left(\frac{a^2 + b^2}{E^2} \right)^{1/2} \right\} \right]^{1/2}\,, \tag{4.21}$$

where

$$a = \int_0^{2\pi} \int_0^{\infty} \cos\theta E(\sigma, \theta) d\sigma d\theta\,, \tag{4.22}$$

and

$$b = \int_0^{2\pi} \int_0^{\infty} \sin\theta E(\sigma, \theta) d\sigma d\theta\,. \tag{4.23}$$

Mean Direction (θ_w)

$$\theta_w = \text{atan}\left(\frac{b}{a}\right) , \tag{4.24}$$

Supplemental Material

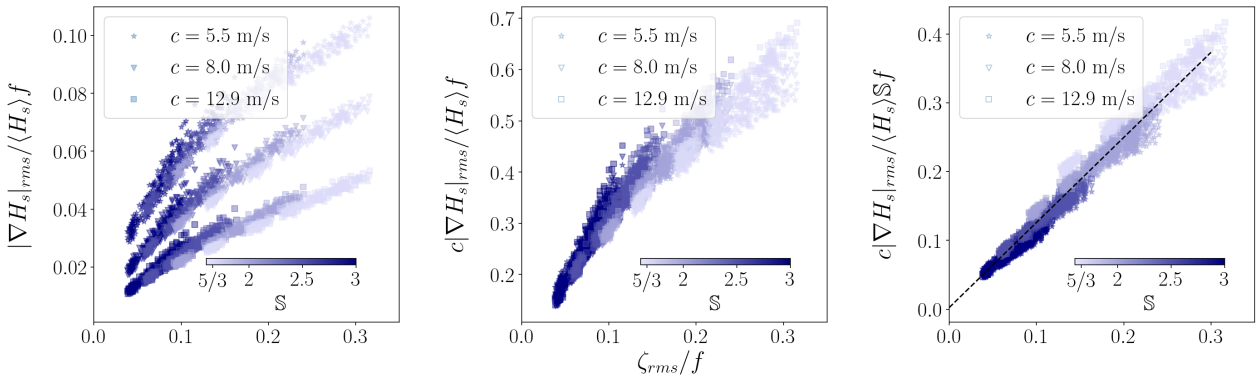

Figure 4.S1: Collapsing of the data under the scaling given by equation (15) in the main manuscript. For this figure, we only show results from experiments run with the synthetic currents and with $KE = 0.01\text{m/s}^2$. The left panel shows the relationship in (15) without scaling by the group speed c and spectral slope $\mathbb{S}$. The middle panel shows the relationship in (15) scaled by the group speed, but not by the spectral slope. The right panel shows the full relationship.

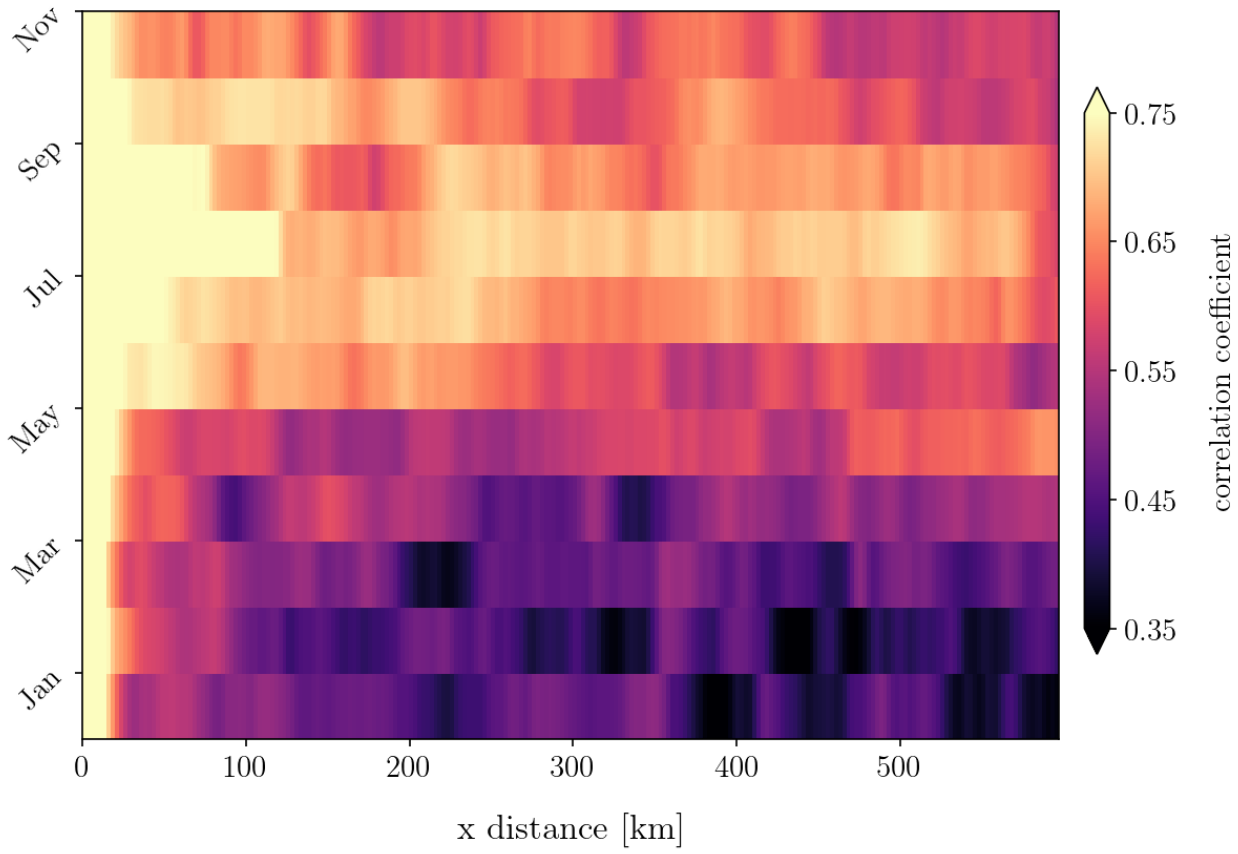

Figure 4.S2: Correlation coefficient between the left and right hand side of equation (17) in the main manuscript calculated as a function of month and distance from the origin ($x = 0$), for the model runs forced by the llc4320 currents. In each bin the correlation was computed across over 28000 points. Note that the correlation coeffitient is higher near the origin and during summer, when the vorticity in the llc4320 in the California Current region is smaller.

Acknowledgments

We thank the two anonymous reviewers for their comments and suggestions. ABVB was funded by NASA Earth and Space Science Fellowship award number 80NSSC17K0326. ABVB, STG, MRM, and, BDC were funded by NASA awards NNX16AH67G and 80NSSC20K1136). ABVB and FA acknowledge the Kavli Institute for Theoretical Physics for partially supporting this research through the National Science Foundation Grant No. NSF PHY17-48958. FA was partially funded by the Office of Naval Research grant N00014-17-1-2402. ABVB first discussed the idea of running this set of experiments with Ken Melville, who was on her PhD committee before he passed away. Ken was a giant in the field of surface waves and she feels extremely grateful for having had the chance to work with him. This paper is dedicated to him.

Chapter 4, in full, reprints material as it appears in Journal Physical Oceanography, 2020, DOI:10.1175/JPO-D-20-0151.1. Ana B. Villas Bôas, Bruce D. Cornuelle, Matthew R. Mazloff, Sarah T. Gille, and Fabrice Ardhuin. The dissertation author was the primary investigator and author of this paper.

Data and Source Code Availability

All model output analyzed in this paper is available from https://doi.org/10.6075/J0X928V6. The source code used to produce the figures can be accessed on https://doi.org/10.5281/zenodo.4045183

Bibliography

Adams, P. N., D. L. Inman, and N. E. Graham, 2008: Southern California deep-water wave climate: characterization and application to coastal processes. *Journal of Coastal Research*, 1022–1035.

Alves, J. H. G., M. L. Banner, and I. R. Young, 2003: Revisiting the Pierson–Moskowitz asymptotic limits for fully developed wind waves. *Journal of physical oceanography*, **33 (7)**, 1301–1323.

Ardhuin, F., B. Chapron, and F. Collard, 2009: Observation of swell dissipation across oceans. *Geophysical Research Letters*, **36 (6)**.

Ardhuin, F., S. Gille, D. Menemenlis, C. Rocha, N. Rascle, B. Chapron, J. Gula, and J. Molemaker, 2017: Small-scale open ocean currents have large effects on wind wave heights. *J. Geophys. Res: Oceans*, **122 (6)**, 4500–4517.

Ardhuin, F., and Coauthors, 2010: Semiempirical dissipation source functions for ocean waves. part i: Definition, calibration, and validation. *Journal of Physical Oceanography*, **40 (9)**, 1917–1941.

Ardhuin, F., and Coauthors, 2012: Numerical wave modeling in conditions with strong currents: Dissipation, refraction, and relative wind. *J. Phys. Oceanogr.*, **42 (12)**, 2101–2120.

Ardhuin, F., and Coauthors, 2019: Skim, a candidate satellite mission exploring global ocean currents and waves. *Frontiers in Marine Science*, **6**.

Bidlot, J.-R., D. J. Holmes, P. A. Wittmann, R. Lalbeharry, and H. S. Chen, 2002: Intercomparison of the performance of operational ocean wave forecasting systems with buoy data. *Weather and Forecasting*, **17 (2)**, 287–310.

Bouffard, J., S. Vignudelli, P. Cipollini, and Y. Menard, 2008: Exploiting the potential of an improved multimission altimetric data set over the coastal ocean. *Geophysical Research Letters*, **35 (10)**.

Bretherton, F. P., and C. J. Garrett, 1968: Wavetrains in inhomogeneous moving media. *Proceedings of the Royal Society of London A: Mathematical, Physical and Engineering Sciences*, **302 (1471)**, 529–554.

Bromirski, P. D., D. R. Cayan, and R. E. Flick, 2005: Wave spectral energy variability in the northeast pacific. *Journal of Geophysical Research: Oceans*, **110 (C3)**.

Bromirski, P. D., D. R. Cayan, J. Helly, and P. Wittmann, 2013: Wave power variability and trends across the North Pacific. *Journal of Geophysical Research: Oceans*, **118 (12)**, 6329–6348.

Brown, G. S., 1977: The average impulse response of a rough surface and its applications. *Antennas and Propagation, IEEE Transactions on*, **25 (1)**, 67–74.

Bühler, O., J. Callies, and R. Ferrari, 2014a: Wave–vortex decomposition of one-dimensional ship-track data. *J. Fluid Mech.*, **756**, 1007–1026.

Bühler, O., J. Callies, and R. Ferrari, 2014b: Wave–vortex decomposition of one-dimensional ship-track data. *Journal of Fluid Mechanics*, **756**, 1007–1026.

Cavaleri, L., B. Fox-Kemper, and M. Hemer, 2012: Wind waves in the coupled climate system. *Bulletin of the American Meteorological Society*, **93 (11)**, 1651–1661.

Chawla, A., D. M. Spindler, and H. L. Tolman, 2013: Validation of a thirty year wave hindcast using the climate forecast system reanalysis winds. *Ocean Modelling*, **70**, 189–206.

Chereskin, T. K., C. B. Rocha, S. T. Gille, D. Menemenlis, and M. Passaro, 2019: Characterizing the transition from balanced to unbalanced motions in the southern california current. *Journal of Geophysical Research: Oceans*, **124 (3)**, 2088–2109.

Collins, C., N. Garfield, T. Rago, F. Rischmiller, and E. Carter, 2000: Mean structure of the inshore countercurrent and california undercurrent off point sur, california. *Deep Sea Research Part II: Topical Studies in Oceanography*, **47 (5)**, 765–782.

Cox, A. T., and V. R. Swail, 2001: A global wave hindcast over the period 1958-1997-validation and climate assessment. *Journal of Geophysical Research*, **106 (C2)**, 2313–2329.

D'Asaro, E., and Coauthors, 2018: Ocean convergence and the dispersion of flotsam. *Proc. Nat. Acad. Sci.*, **115 (6)**, 1162–1167.

Di Lorenzo, E., 2003: Seasonal dynamics of the surface circulation in the southern california current system. *Deep Sea Research Part II: Topical Studies in Oceanography*, **50 (14)**, 2371–2388.

Donelan, M., 1998: Air-water exchange processes. *Physical Processes in Lakes and Oceans*, 19–36.

Dysthe, K., 2001a: Refraction of gravity waves by weak current gradients. *J. Fluid Mech.*, **442**, 157–159.

Dysthe, K. B., 2001b: Refraction of gravity waves by weak current gradients. *Journal of Fluid Mechanics*, **442**, 157–159.

Farrar, J. T., E. D'Asaro, E. Rodriguez, A. Shcherbina, and Coauthors, 2020: S-mode: The submesoscale ocean dynamics experiment. *2020 IEEE International Geoscience and Remote Sensing Symposium, Waikoloa, Hawaii, USA*, 1–4.

Ferrari, R., and C. Wunsch, 2008: Ocean circulation kinetic energy: Reservoirs, sources, and sinks. *Annual Review of Fluid Mechanics*, **41 (1)**, 253.

Fu, L.-L., and R. Glazman, 1991: The effect of the degree of wave development on the sea state bias in radar altimetry measurement. *Journal of Geophysical Research: Oceans*, **96 (C1)**, 829–834.

Gallet, B., and W. Young, 2014: Refraction of swell by surface currents. *J. Mar. Res.*, **72 (2)**, 105–126.

Glazman, R. E., and S. H. Pilorz, 1990: Effects of sea maturity on satellite altimeter measurements. *Journal of Geophysical Research: Oceans*, **95 (C3)**, 2857–2870.

Halliwell, G. R., and J. S. Allen, 1987: The large-scale coastal wind field along the west coast of North America, 1981–1982. *Journal of Geophysical Research: Oceans*, **92 (C2)**, 1861–1884.

Hanley, K. E., S. E. Belcher, and P. P. Sullivan, 2010: A global climatology of wind–wave interaction. *Journal of Physical Oceanography*, **40 (6)**, 1263–1282.

Harms, S., and C. D. Winant, 1998: Characteristic patterns of the circulation in the santa barbara channel. *Journal of Geophysical Research: Oceans*, **103 (C2)**, 3041–3065.

Heller, E., L. Kaplan, and A. Dahlen, 2008: Refraction of a Gaussian seaway. *J. Geophys. Res.: Oceans*, **113 (C9)**.

Henderson, S., R. Guza, S. Elgar, and T. Herbers, 2006: Refraction of surface gravity waves by shear waves. *J. Phys. Oceanogr.*, **36 (4)**, 629–635.

Irvine, D., and D. Tilley, 1988: Ocean wave directional spectra and wave-current interaction in the agulhas from the shuttle imaging radar-b synthetic aperture radar. *Journal of Geophysical Research: Oceans*, **93 (C12)**, 15 389–15 401.

Kafiabad, H., M. Savva, and J. Vanneste, 2019: Diffusion of inertia-gravity waves by geostrophic turbulence. *J. Fluid Mech.*, **869**, R7.

Kenyon, K., 1971a: Wave refraction in ocean currents. *Deep-Sea Res. and Oceanographic Abstracts*, **18 (10)**, 1023–1034.

Kenyon, K. E., 1971b: Wave refraction in ocean currents. *Deep Sea Research and Oceanographic Abstracts*, **18 (10)**, 1023 – 1034, doi:https://doi.org/10.1016/0011-7471(71)90006-4, URL http://www.sciencedirect.com/science/article/pii/0011747171900064.

Kirby, J., and T.-M. Chen, 1989: Surface waves on vertically sheared flows: approximate dispersion relations. *J. Geophys. Res: Oceans*, **94 (C1)**, 1013–1027.

Koračin, D., and C. E. Dorman, 2001: Marine atmospheric boundary layer divergence and clouds along California in June 1996. *Monthly Weather Review*, **129 (8)**, 2040–2056.

Koračin, D., C. E. Dorman, and E. P. Dever, 2004: Coastal perturbations of marine-layer winds, wind stress, and wind stress curl along California and Baja California in June 1999. *Journal of Physical Oceanography*, **34 (5)**, 1152–1173.

Landau, L., and E. Lifshitz, 1987a: Fluid Mechanics. Pergamon.

Landau, L. D., and E. M. Lifshitz, 1987b: *Fluid Mechanics, Second Edition: Volume 6 (Course of Theoretical Physics)*. 2nd ed., Elsevier, 266 pp.

Long, R. B., 1980: The statistical evaluation of directional spectrum estimates derived from pitch/roll buoy data. *Journal of Physical Oceanography*, **10 (6)**, 944–952.

Longuet-Higgins, M. S., 1963: The effect of non-linearities on statistical distributions in the theory of sea waves. *Journal of fluid mechanics*, **17 (03)**, 459–480.

Longuet-Higgins, M. S., D. Cartwright, and N. Smith, 1963: Observations of the directional spectrum of sea waves using the motions of a floating buoy.

Longuet-Higgins, M. S., and R. Stewart, 1961: The changes in amplitude of short gravity waves on steady non-uniform currents. *Journal of Fluid Mechanics*, **10 (04)**, 529–549.

Longuet-Higgins, M. S., and R. Stewart, 1962: Radiation stress and mass transport in gravity waves, with application to 'surf beats'. *Journal of Fluid Mechanics*, **13 (4)**, 481–504.

Lygre, A., and H. E. Krogstad, 1986: Maximum entropy estimation of the directional distribution in ocean wave spectra. *Journal of Physical Oceanography*, **16 (12)**, 2052–2060.

Masson, D., 1996: A case study of wave-current interaction in a strong tidal current. *Journal of Physical Oceanography*, **26 (3)**, 359–372.

McComas, C., and F. Bretherton, 1977: Resonant interaction of oceanic internal waves. *J. Geophys. Res.*, **82 (9)**, 1397–1412.

McWilliams, J. C., 2016: Submesoscale currents in the ocean. *Proceedings of the Royal Society A: Mathematical, Physical and Engineering Sciences*, **472 (2189)**, 20160 117.

McWilliams, J. C., 2018: Surface wave effects on submesoscale fronts and filaments. *Journal of Fluid Mechanics*, **843**, 479–517.

Mei, C., 1989: *The Applied Dynamics of Ocean Surface Waves*, Vol. 1. World Scientific.

Melville, W., R. Stewart, W. Keller, J. A. Kong, D. Arnold, A. Jessup, M. Loewen, and A. Slinn, 1991: Measurements of electromagnetic bias in radar altimetry. *Journal of Geophysical Research: Oceans*, **96 (C3)**, 4915–4924.

Morrow, R., and Coauthors, 2019: Global observations of fine-scale ocean surface topography with the surface water and ocean topography (SWOT) mission. *Frontiers in Marine Science*, **6**, 232.

Munk, W. H., and M. A. Traylor, 1947: Refraction of ocean waves: a process linking underwater topography to beach erosion. *The Journal of Geology*, **55 (1)**, 1–26.

O'Reilly, W., T. Herbers, R. Seymour, and R. Guza, 1996: A comparison of directional buoy and fixed platform measurements of pacific swell. *Journal of Atmospheric and Oceanic Technology*, **13 (1)**, 231–238.

Peral, E., E. Rodríguez, and D. Esteban-Fernández, 2015: Impact of surface waves on SWOT's projected ocean accuracy. *Remote Sensing*, **7 (11)**, 14 509–14 529.

Peregrine, D., 1976: Interaction of water waves and currents. *Advances in Applied Mechanics.*, Vol. 16, Elsevier, 9–117.

Phillips, O., 1966: *The Dynamics of the Upper Ocean*. Cambridge University Press.

Phillips, O. M., 1980: *The dynamic of upper ocean*. 2nd ed., Cambridge press.

Pierson, W. J., 1955: Wind generated gravity waves. *Advances in geophysics*, **2**, 93–178.

Pierson, W. J., and L. Moskowitz, 1964: A proposed spectral form for fully developed wind seas based on the similarity theory of SA Kitaigorodskii. *Journal of geophysical research*, **69 (24)**, 5181–5190.

Portilla-Yandún, J., A. Salazar, and L. Cavaleri, 2016: Climate patterns derived from ocean wave spectra. *Geophysical Research Letters*, **43 (22)**.

Qiu, B., S. Chen, P. Klein, J. Wang, H. Torres, L.-L. Fu, and D. Menemenlis, 2018: Seasonality in transition scale from balanced to unbalanced motions in the world ocean. *J. Phys. Oceanogr.*, **48 (3)**, 591–605.

Qiu, B., T. Nakano, S. Chen, and P. Klein, 2017: Submesoscale transition from geostrophic flows to internal waves in the northwestern pacific upper ocean. *Nature communications*, **8 (1)**, 1–10.

Queffeulou, P., 2004: Long-term validation of wave height measurements from altimeters. *Marine Geodesy*, **27 (3-4)**, 495–510.

Quilfen, Y., and B. Chapron, 2019: Ocean surface wave-current signatures from satellite altimeter measurements. *Geophys. Res. Lett.*, **46 (1)**, 253–261.

Quilfen, Y., M. Yurovskaya, B. Chapron, and F. Ardhuin, 2018: Storm waves focusing and steepening in the Agulhas current: Satellite observations and modeling. *Remote Sensing of Environment*, **216**, 561–571.

Rascle, N., and F. Ardhuin, 2013: A global wave parameter database for geophysical applications. Part 2: Model validation with improved source term parameterization. *Ocean Modelling*, **70**, 174–188.

Rocha, C., T. Chereskin, S. Gille, and D. Menemenlis, 2016a: Mesoscale to submesoscale wavenumber spectra in Drake Passage. *J. Phys. Oceanogr.*, **46 (2)**, 601–620.

Rocha, C. B., S. T. Gille, T. K. Chereskin, and D. Menemenlis, 2016b: Seasonality of submesoscale dynamics in the Kuroshio extension. *Geophysical Research Letters*, **43 (21)**, 11–304.

Rodionov, S., J. Overland, and N. Bond, 2005: The Aleutian low and winter climatic conditions in the Bering Sea. Part I: Classification. *Journal of Climate*, **18 (1)**, 160–177.

Rodríguez, E., M. Bourassa, D. Chelton, J. T. Farrar, D. Long, D. Perkovic-Martin, and R. Samelson, 2019: The winds and currents mission concept. *Frontiers in Marine Science*.

Romero, L., 2019: Distribution of surface wave breaking fronts. *Geophysical Research Letters*, **46 (17-18)**, 10 463–10 474.

Romero, L., D. Hypolite, and J. C. McWilliams, 2020: Submesoscale current effects on surface waves. *Ocean Modelling*, 101662.

Romero, L., L. Lenain, and W. K. Melville, 2017: Observations of surface wave–current interaction. *Journal of Physical Oceanography*, **47 (3)**, 615–632.

Schroeder, I. D., B. A. Black, W. J. Sydeman, S. J. Bograd, E. L. Hazen, J. A. Santora, and B. K. Wells, 2013: The North Pacific High and wintertime pre-conditioning of California current productivity. *Geophysical Research Letters*, **40 (3)**, 541–546.

Schwendeman, M., and J. Thomson, 2015: Observations of whitecap coverage and the relation to wind stress, wave slope, and turbulent dissipation. *Journal of Geophysical Research: Oceans*, **120 (12)**, 8346–8363.

Seymour, R., 1996: Wave climate variability in southern california. *Journal of Waterway, Port, Coastal, and Ocean Engineering*, **122 (4)**, 182–186.

Seymour, R. J., R. R. Strange III, D. R. Cayan, and R. A. Nathan, 1985: Influence of el niños on california's wave climate. *Coastal Engineering 1984*, 577–592.

Smit, P. B., and T. T. Janssen, 2019: Swell propagation through submesoscale turbulence. *Journal of Physical Oceanography*, **49 (10)**, 2615–2630.

Snodgrass, F., G. W. Groves, K. Hasselmann, G. Miller, W. Munk, and W. Powers, 1966: Propagation of ocean swell across the pacific. *Philosophical Transactions of the Royal Society of London A: Mathematical, Physical and Engineering Sciences*, **259 (1103)**, 431–497.

Stopa, J. E., and K. F. Cheung, 2014: Intercomparison of wind and wave data from the ECMWF Reanalysis Interim and the NCEP Climate Forecast System Reanalysis. *Ocean Modelling*, **75**, 65–83.

Sullivan, P. P., J. C. McWilliams, and W. K. Melville, 2004: The oceanic boundary layer driven by wave breaking with stochastic variability. Part 1. direct numerical simulations. *Journal of Fluid Mechanics*, **507**, 143–174.

Suzuki, N., 2019: On the physical mechanisms of the two-way coupling between a surface wave field and a circulation consisting of a roll and streak. *Journal of Fluid Mechanics*, **881**, 906–950.

Sverdrup, H. U., and W. H. Munk, 1947: Wind, sea, and swell: theory of relations for forecasting. *US Hydrographic Office, Washington, D.C*, **601**.

Taylor, S. V., D. R. Cayan, N. E. Graham, and K. P. Georgakakos, 2008: Northerly surface winds over the eastern North Pacific Ocean in spring and summer. *Journal of Geophysical Research: Atmospheres*, **113 (D2)**.

Torres, H. S., P. Klein, D. Menemenlis, B. Qiu, Z. Su, J. Wang, S. Chen, and L.-L. Fu, 2018: Partitioning ocean motions into balanced motions and internal gravity waves: A modeling study in anticipation of future space missions. *Journal of Geophysical Research: Oceans*, **123 (11)**, 8084–8105.

Villas Bôas, A. B., and Coauthors, 2019: Integrated observations of global surface winds, currents, and waves: Requirements and challenges for the next decade. *Frontiers in Marine Science*, **6**, 425, doi:10.3389/fmars.2019.00425, URL https://www.frontiersin.org/article/10.3389/fmars.2019.00425.

Villas Bôas, A. B., and W. R. Young, 2020: Directional diffusion of surface gravity wave action by ocean macroturbulence. *Journal of Fluid Mechanics*, **890**, R3, doi:10.1017/jfm.2020.116.

Wang, D. W., A. K. Liu, C. Y. Peng, and E. A. Meindl, 1994: Wave-current interaction near the gulf stream during the surface wave dynamics experiment. *Journal of Geophysical Research: Oceans*, **99 (C3)**, 5065–5079.

Wang, J., L.-L. Fu, B. Qiu, T. Farrar, and D. Menemenlis, 2016: An observing system simulation experiment (OSSE) on the design of an in-situ observing system for the CalVal of SWOT SSH measurement.

Wang, X. L., and V. R. Swail, 2001: Changes of extreme wave heights in northern hemisphere oceans and related atmospheric circulation regimes. *Journal of Climate*, **14 (10)**, 2204–2221.

WAVEWATCH III Development Group, 2009: User manual and system documentation of wavewatch iii version 3.14, technical note. *Camp Springs MD: US Department of Com-*

merce, National Oceanographic and Atmospheric Administration, National Weather Service, National Centers for Environmental Predictions.

WAVEWATCH III Development Group, 2016: User manual and system documentation of wavewatch iii tm version 5.16. *Technical note*, **329**, 326.

White, B., and B. Fornberg, 1998: On the chance of freak waves at sea. *J. Fluid Mech.*, **355**, 113–138.

Winant, C., C. Dorman, C. Friehe, and R. Beardsley, 1988: The marine layer off northern California: An example of supercritical channel flow. *Journal of the Atmospheric Sciences*, **45 (23)**, 3588–3605.

Young, I., S. Zieger, and A. V. Babanin, 2011: Global trends in wind speed and wave height. *Science*, **332 (6028)**, 451–455.

Zemba, J., and C. A. Friehe, 1987: The marine atmospheric boundary layer jet in the coastal ocean dynamics experiment. *Journal of Geophysical Research: Oceans*, **92 (C2)**, 1489–1496.

Zieger, S., J. Vinoth, and I. Young, 2009: Joint calibration of multiplatform altimeter measurements of wind speed and wave height over the past 20 years. *Journal of Atmospheric and Oceanic Technology*, **26 (12)**, 2549–2564.